Electron Spin Transport in Quantum Dots and Point Contacts

University of Groningen
Zernike Institute for Advanced Materials

Zernike Institute PhD thesis series 2008-22
ISSN: 1570-1530
ISBN: 978-90-367-3530-8 (printed version)
ISBN: 978-90-367-3529-2 (electronic version)

The work described in this thesis was performed in the research group Physics of Nanodevices of the Zernike Institute of Advanced Materials at the University of Groningen, the Netherlands. This work is part of the research program of the 'Stichting voor Fundamenteel Onderzoek der Materie (FOM)', which is financially supported by the 'Nederlandse Organisatie voor Wetenschappelijk Onderzoek (NWO)'.

Printed by: Drukkerij van Denderen, Groningen

Rijksuniversiteit Groningen

Electron Spin Transport in Quantum Dots and Point Contacts

Proefschrift

ter verkrijging van het doctoraat in de
Wiskunde en Natuurwetenschappen
aan de Rijksuniversiteit Groningen
op gezag van de
Rector Magnificus, dr. F. Zwarts,
in het openbaar te verdedigen op
vrijdag 12 september 2008
om 13:15 uur

door

Erik Johan Koop

geboren op 27 mei 1980
te Stadskanaal

Promotor:	Prof. dr. ir. B. J. van Wees
Copromotor:	Dr. ir. C. H. van der Wal
Beoordelingscommissie:	Prof. dr. J. A. Folk
	Prof. dr. Y. Meir
	Prof. dr. D. M. Zumbühl

Contents

Chapter 1

Introduction

1.1 Electrons: charge and spin

In classical mechanics, the spin angular momentum is associated with the rotation of a body around its own center of mass. For example, the spin of the Earth is associated with its daily rotation about the polar axis, not to be confused with the orbital angular momentum of the Earth which is associated with its annual motion around the Sun.

The concept spin for elementary particles was first proposed in 1925 by Uhlenbeck and Goudsmit [1, 2]. However, the first experimental observations that were in fact due to spin were made long before that, when in 1857 the Anisotropic MagnetoResistance (AMR) was discovered [3]. The classic experiment by Stern and Gerlach in 1922 showed there was more to the electron than only its charge and was the first direct observation of the quantization of angular momentum [4].

In some ways an electron can be considered as a spinning sphere of charge. In classical terms that means that it possesses a magnetic dipole moment and that it can be described as a vector that is (for a free electron) antiparallel to the direction of its spin. Consequently, a magnetic field can exert a torque such that the spin vector undergoes precession. However, spin is a purely quantum mechanical property. Quantum mechanics states that whenever the spin of an electron is measured along a certain axis, there are only two possible outcomes, either spin-up or spin-down. The field of spintronics (or spin-based electronics) was founded on this quantum mechanical form of binary logic. Currently, several research efforts investigate whether spin can play a role in the electron transport properties of materials and electronic devices.

1.2 Motivation

This thesis presents research that aims at improving the understanding and control of the dynamics of electrons and electron spin in electronic nanodevices. Our work contributes mainly to fundamental research on these topics. The behavior of electrons and spins is studied in nanodevices that are fabricated with ultra-clean non-magnetic semiconductors, and by state-of-the-art nanofabrication processes. Further, the experiments are performed at very low temperatures (less than one degree above absolute zero), such that thermal fluctuations do not impede an analysis of how fundamental interactions in materials influence electron and spin states in nanodevices. Even though this work is fundamental in character, this research is related to application-driven research in the field of spintronics. In the remainder of this section, I will first introduce the two experimental systems that were used in this research (the quantum point contact and the quantum dot), and discuss for each system the scientific questions that underlie the work. After this, I will shortly summarize why these studies are of importance for developing practical spintronic devices.

Research on Quantum Point Contacts

The first part of this thesis presents experiments on Quantum Point Contacts (QPCs). A QPC is a narrow constriction between two large electron reservoirs and is essentially a short one-dimensional transport channel in which the electron transport is ballistic. It is one of the most fundamental electronic systems and a key model system for showing how modern nanotechnology can give electronic devices in which there is very high control over the electronic states and transport. In particular, these devices show quantized conductance [5, 6], an effect that has now been observed and understood for 20 years already. Furthermore, the electron emission from QPCs can be spin-polarized when a strong in-plane magnetic field is applied [7]. The conductance of this device also shows several features that reveal signatures of electron many-body effects, which include the so-called 0.7 anomaly, enhancement of the electron g-factor, and the Kondo effect.

In particular the 0.7 anomaly has been observed in nearly all QPC studies in these last 20 years, but it is still not fully understood. At the same time, this phenomenon is very interesting. Several models have been proposed that relate the 0.7 anomaly to a spontaneous spin splitting in zero magnetic field [8, 9]. The Kondo effect is a many-body interaction effect between a single magnetic impurity and a sea of conduction electrons [10]. An earlier study on QPCs [11]

investigated a feature in the QPC conductance that shows remarkable similarity to a characteristic of the Kondo effect seen in few-electron quantum dots [12], where a localized state with a magnetic impurity is deliberately formed. The Kondo signatures in a QPC suggest that by only making a narrow constriction in a clean non-magnetic semiconductor, a localized state can spontaneously form, while a QPC is in fact an open quantum system.

Thus, the QPC provides a very simple model system, that is suited for investigating how many-body effects and electron spin can affect electron and spin transport in nanodevices. Notably, the QPC is a key element in several proposal for spintronics and quantum information devices, and for this the understanding of these many-body effects is important. The work on QPCs that is presented in this thesis aims to improve the understanding of these many-body effects by looking at the influence of a change in QPC geometry, and hence Coulomb effects, on the signatures of these many-body phenomena. Further, we studied the possible correlation between the 0.7 anomaly and signatures of the Kondo effect. We also used this work to determine how the spin-polarized emission of electrons from QPCs in strong magnetic fields can be optimized.

Spin relaxation in large Quantum Dots

The second part of this thesis presents experiments on electron spin relaxation in large open quantum dots. Spin accumulation and relaxation of the spin ensemble is in these systems influenced by ballistic scattering of electrons in the device structure. Such a system is best described as an electron ensemble that is ballistically scattering inside a chaotic cavity., thus providing a regime in between bulk samples (that have been mainly studied with optical techniques [13]) and ultra small dots [14]. For large open dots, however, spin relaxation occurs in a fundamentally different manner and its full understanding is still a challenge to the spintronics community [15]. It is expected that spin-orbit effects have a dominant role, and that the scattering rate at the edge of the dot is important.

Spin-orbit interaction results from the motion of an electron in an electric field [16]. The electric field is felt as a magnetic field in the electron's rest frame and interacts with the spin of the electron, leading to precession of the spin state. This effect is a source of relaxation but also a possible means for controlled spin manipulation. This is in contrast with spin relaxation in few-electron dots, where electrons are highly localized due to quantum confinement, and the spin relaxation due to momentum scattering inside the dot and spin-orbit effects is thereby nearly irrelevant [17].

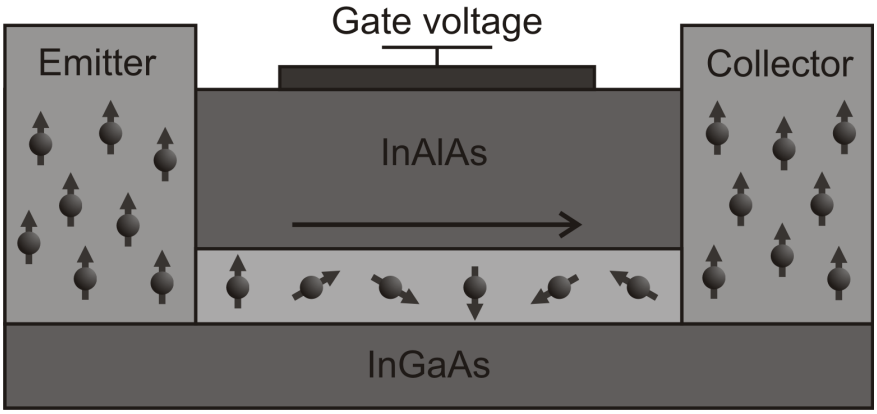

Figure 1.1: Schematic drawing of the Datta-Das spin transistor. A ferromagnetic electrode emits spin-aligned electrons into a narrow semiconducting channel. During transport in the channel towards the ferromagnetic collector the electrons precess around the spin-orbit fields that can be controlled by the gate electrode. The resistance of the device is determined by the alignment of the spins with the direction of magnetization of the ferromagnetic collector electrode when they arrive at the collector. The resistance, and thus also the emitter-collector current can be modulated by the gate voltage.

The work in this thesis aims at observing spin signals from large quantum dots and to understand the relaxation mechanism in these systems. At the same time, such results are indeed relevant for developing spintronic devices that work with large spin ensembles in device structures (as for example the Datta-Das transistor) instead of few-electron dots. We succeeded in measuring electronically the spin relaxation time, which is a measure for how long the spin polarization of the ensemble of electrons can be maintained. We also performed a numerical study of the interaction of the oriented spin ensemble with its environment via the spin-orbit interaction. In particular, we wanted to understand how the spin polarization evolves in various device geometries.

Relation with the field of spintronics

Besides being an interesting topic for fundamental research on its own, the spin degree of freedom may offer new device functionalities that cannot be achieved with charge transport alone, and that could lead to a new generation of computational devices [18, 19].

The field of metallic spintronics originates from the discovery of the Giant

MagnetoResistance (GMR) in 1988 [20, 21] and subsequent development of the spin valve [22]. Since then, the GMR effect has already found many practical applications, mainly in the read heads used for high density data storage on computer hard disks. The discovery of this effect has therefore been rewarded with the 2007 Nobel prize in physics. The interest in semiconductor spintronics was greatly stimulated by a proposal in 1990 by Datta and Das for a field-effect spin transistor [23]. We will present it here as an archetype example of a device that shows spintronic functionality. In this device, shown schematically in Fig. 1.1, spins are injected into a two-dimensional semiconductor transport channel by a ferromagnetic emitter electrode and detected by a ferromagnetic collector electrode. The emitter injects electrons with their spin oriented along the direction of its magnetization. The electrons are precessing during transport from emitter to collector as a result of spin-orbit coupling. The resistance of this device is high when on average electrons arrive at the collector with their spin anti-parallel to the magnetization of the collector and low when their spin is parallel to this magnetization. The gate electrode influences the strength of the spin-orbit interaction and therefore modulates the resistance of the device.

This example shows that the ability to generate, transport, and detect electron spin in a controlled manner is important for the field of spintronics and is also a very useful tool for investigating basic properties of spin in electronic systems. The electrical injection, transport and detection of spin has been demonstrated for metals in a non-local measurement geometry [24, 25]. Non-local experiments sensitive to precession of the spins around an externally applied magnetic field were also performed [26, 27]. Early efforts towards realization of spin injection in semiconductors using a ferromagnetic metal, as proposed for the Datta-Das spin transistor, were complicated by an effect known as the conductivity mismatch [28]. A solution to this fundamental limitation in polarization of the injected current was the use of tunnel barriers [29, 30], but only very recently experimental results were presented for the all-electrical injection, detection [31], and precession [32] of spin polarization in an n-doped GaAs channel using ferromagnetic contacts. The work that is presented in this thesis is therefore clearly relevant for open questions regarding spin injection and manipulation, and contributes to the understanding of fundamental properties of electron and spin transport in semiconductor nanostructures.

1.3 Outline of this thesis

In this thesis we thus present experimental and numerical results on quantum point contacts and quantum dots. *Chapter 3* then forms the first part devoted measurements on individual quantum point contacts. *Chapters 4*, *5*, and *6* form the second part, presenting experiments and a numerical study, related to spin accumulation and relaxation in a quantum dot. In addition we present in *Chapter 7* an experimental study of the fabrication of ohmic contacts to a GaAs heterostructure. We start in *Chapter 2* with an explanation of the basic theory of quantum dots and point contacts. Further, this chapter describes how we fabricate our devices and we present the measurement techniques and set-up used in this work.

In *Chapter 3* we present an experimental study of the dependence of many-body effects, like the 0.7 anomaly, the enhancement of the electron g-factor, and the Kondo effect, on the geometry of a QPC. We determine these properties for a set of 12 QPCs with identical material parameters, where we used different values for the length L and width W for the electrode spacing that defines the device. We find a clear relation between the enhanced g-factor and the subband spacing in our QPCs, and can relate this to the device geometry with electrostatic modeling of the QPC potential. The many-body electron physics that causes the apparent energy splitting of the 0.7 anomaly does not show a clear dependence on QPC geometry, but we do find a clear correlation with a field-independent exchange effect that contributes to spin splittings in high magnetic fields. Signatures of the Kondo effect also show no regular dependence on QPC geometry, but are possibly correlated with the splitting of the 0.7 anomaly.

In *Chapter 4* we present experimental results on a four-terminal quantum dot system in a GaAs heterostructure. We use a non-local measurement geometry for studying spin accumulation and relaxation. We find that this can be used to extract in a single measurement the relaxation time for electron spins inside the dot ($\tau_{sf} \approx 300$ ps), contributions to the relaxation from coupling to the reservoirs, and the degree of spin polarization of the contacts ($P \approx 0.8$). In this Chapter we also study the two-terminal conductance of a quantum dot, where one of the contacts is used as a spin filter. We find that this method is harder to implement since it requires a very flat spin-resolved conductance plateau for a QPC. We could therefore not get a clear conclusion for the spin relaxation time or polarization of the contacts using this method.

In *Chapter 5* we present a numerical study of electron spin relaxation due

to spin-orbit interaction in confined systems where we study the effects of confinement and large external magnetic fields. We used an approach where the relaxation was simulated with semiclassical electron trajectories, and studied 2D and confined systems with realistic device parameters. We find that confinement in a micronscale dot can result in enhanced relaxation with respect to a free two-dimensional electron ensemble, contrary to the established result that strong confinement or frequent momentum scattering reduces relaxation.

Chapter 6 presents additional experimental results on quantum dots, where we investigate quantum fluctuations in the non-local resistance of an open quantum dot which is connected to four reservoirs via quantum point contacts. The amplitude of the resistance fluctuations is strongly reduced when the coupling between the voltage probe reservoirs and the dot is enhanced. Along with experimental results, we present a theoretical analysis based on the Landauer-Büttiker formalism.

Ohmic contacts to a two-dimensional electron gas (2DEG) in GaAs/AlGaAs heterostructures are often realized by annealing of AuGe/Ni/Au that is deposited on its surface. In the last chapter of this thesis, *Chapter 7*, we study how the quality of this type of ohmic contact depends on the annealing time and temperature, where we focussed on the question how the optimum parameters change for a different depth of the 2DEG. Combined with transmission electron microscopy and energy dispersive X-ray spectroscopy studies of the annealed contacts, our results allow for identifying the annealing mechanism and describing a model that can predict optimal annealing parameters for a certain heterostructure.

References

[1] G. Uhlenbeck, and S. Goudsmit, Naturwissenschaften **47**, 264 (1925).

[2] G. Uhlenbeck, and S. Goudsmit, Nature **117**, 264 (1926).

[3] W. Thomson, Proc. R. Soc. **8**, 546 (1857).

[4] W. Gerlach and O. Stern, Zeit. Phys. **9**, 349 (1922).

[5] B. J. van Wees *et al.*, Phys. Rev. Lett. **60**, 848 (1988).

[6] D. A. Wharam *et al.*, J. Phys. C **21**, L209 (1988).

[7] R. M. Potok *et al.*, Phys. Rev. Lett. **89**, 266602 (2002).

[8] R. Fitzgerald, Phys. Today **55**, 21 (May 2002).

[9] K. Ensslin, Nature Phys. **2**, 587 (2006).

[10] L. P. Kouwenhoven and L. Glazman, Physics World **14**, 33 (2001).

[11] S. M. Cronenwett *et al.*, Phys. Rev. Lett. **88**, 226805 (2002).

[12] D. Goldhaber-Gordon *et al.*, Nature **391**, 156 (1998); S. M. Cronenwett, T. H. Oosterkamp, and L. P. Kouwenhoven, Science **281**, 540 (1998); W. G. van der Wiel *et al.*, Science **289**, 2105 (2000).

[13] D. D. Awschalom, N. Samarath, and D. Loss (eds.), *Semiconductor Spintronics and Quantum Computation* (Springer, Heidelberg, 2002).

[14] For a review see R. Hanson *et al.*, Rev. Mod. Phys. **79**, 1217 (2007).

[15] See for example C. W. J. Beenakker, Phys. Rev. B **73**, R201304 (2006).

[16] For a review see R. H. Silsbee, J. Phys.: Cond. Mat. **16**, R179 (2004).

[17] A. V. Khaetskii and Y. V. Nazarov, Phys. Rev. B **61**, 12639 (2000); A. V. Khaetskii and Y. V. Nazarov, Phys. Rev. B **64**, 125316 (2001).

[18] D. D. Awschalom and M. E. Flatté, Nature Phys. **3**, 153 (2007).

[19] I. Žutić, J. Fabian, and S. Das Sarma, Rev. Mod. Phys. **76**, 323 (2004).

[20] M. Baibich *et al.*, Phys. Rev. Lett. **61**, 2472 (1988).

[21] J. Barnas *et al.*, Phys. Rev. B **39**, 4828 (1989).

[22] B. Dieny *et al.*, Phys. Rev. B **43**, 1297 (1991).

[23] S. Datta and B. Das, Appl. Phys. Lett. **56**, 665 (1990).

[24] M. Johnson and R. H. Silsbee, Phys. Rev. Lett. **55**, 1790 (1985).

[25] F. J. Jedema, A. T. Filip, and B. J. van Wees, Nature **410**, 345 (2001).

[26] F. J. Jedema *et al.*, Nature **416**, 713 (2002).

[27] M. Zaffalon and B. J. van Wees, Phys. Rev. Lett. **91**, 186601 (2003).

[28] G. Schmidt *et al.*, Phys. Rev. B **62**, R4790 (2000).

[29] E. I. Rashba, Phys. Rev. B **62**, R16267 (2000).

[30] H. J. Zhu *et al.*, Phys. Rev. Lett. **87**, 016601 (2001).

[31] X. Lou *et al.*, Phys. Rev. Lett. **96**, 176603 (2006).

[32] X. Lou *et al.*, Nature Phys. **3**, 197 (2007).

Chapter 2

Theory, device fabrication and measurement techniques

2.1 Quantum Point Contacts

One of the most fundamental systems in mesoscopic physics is the Quantum Point Contact (QPC). Generally speaking a QPC is a short channel that carries ballistic one-dimensional electron transport between two reservoirs. Its conductance as a function of channel width is quantized [1, 2] and shows plateaus at integer multiples of $2e^2/h$, where e is the electron charge and h Planck's constant.

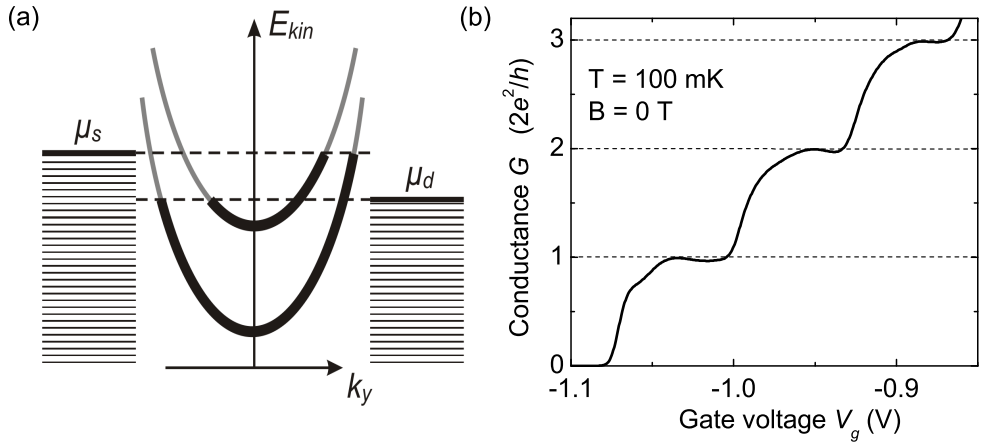

Figure 2.1: **(a)** Energy of one-dimensional subbands as a function of longitudinal wave function k_y. Electrons in the source and drain leads are filled up to their chemical potentials, μ_s and μ_d. **(b)** The conductance G of a QPC, quantized in steps of $2e^2/h$ as a function of gate voltage V_g in zero magnetic field.

This type of device can be formed by two depletion gates on the surface of a GaAs/AlGaAs heterostructure with a 2-Dimensional Electron Gas (2DEG) below the surface. This is the so-called split gate QPC. When a negative voltage is applied to these gates with respect to the 2DEG, the 2DEG directly beneath the gates is electrostatically depleted. These constrictions can also be created by etching two trenches with a narrow gap in between. Then the 2DEG is locally destroyed. All devices presented in this thesis are formed by depletion gates.

The potential felt by the electrons near a QPC can be approximated as a saddle-point potential [3]. The confinement for the two transverse directions leads to the quantization of energy levels. There is a parabolic confinement in x-direction $1/2m^*\omega_0^2x^2$, like the harmonic oscillator potential, where x is the direction in plane perpendicular to the current direction. In z-direction the confinement of the 2DEG also leads to quantization of energy levels in that direction. The energy dispersion is then

$$E_n(k_y) = \frac{h^2k_y^2}{2m^*} + E_{n,x} + E_z, \tag{2.1}$$

where $E_{n,x}$ is given by

$$E_{n,x} = (n - \frac{1}{2})\hbar\omega_0 + eV_0, \tag{2.2}$$

where V_0 is the bottom of the constriction, $\hbar\omega_0$ is the level separation, k_y is the wave vector in y-direction, and n labels the subbands in x-direction. We assume that the confinement in z direction is much stronger, such that only the lowest subband in the 2DEG is occupied.

These energies describe 1-D subbands because electrons are free to move in the y-direction (described by the free-electron kinetic energy dispersion) but quantized in the x-direction. Figure 2.1 shows these 1-D subband dispersions versus the longitudinal wave vector k_y. Electrons in the source and drain leads fill up states in the Fermi sea to the respective chemical potentials, μ_s and μ_d. The current is then determined by the number of subbands that lie below or in between these potentials.

In the next section we will derive the quantized conductance and properties of these type of devices in electric and magnetic fields. Here we will also introduce the 0.7 anomaly and other signatures of many-body effects, but we will mainly focus on non-interacting electrons. Many-body interaction effects in QPCs and their effect on the conductance properties will be discussed in more detail in Chapter 3.

2.2 Quantized conductance

A current will flow through the 1D conductor when a voltage V_{sd} is applied across the source and the drain reservoirs. The chemical potentials of these reservoirs are then related as $eV_{sd} = \mu_s - \mu_d$ and the current that will flow is

$$I = \sum_{n=1}^{N_c} \int_0^\infty 2eN_n(E)\upsilon_n(E)[f(E,\mu_s) - f(E,\mu_d)]T_n(E)dE, \tag{2.3}$$

where $N_c = integer[\frac{E_F - eV_0}{\hbar\omega_0} + \frac{1}{2}]$ is the total number of modes propagating through the QPC, $N_n(E) = \frac{1}{2\pi}[dE_n(k_y)/dk_y]^{-1}$ is the 1D density of states, $f(E,\mu_{s,d})$ are Fermi-Dirac distributions, $T_n(E)$ is the transmission probability through the QPC and $\upsilon_n(E) = \frac{1}{\hbar}[dE_n(k_y/dk_y]$ is the group velocity. Since the product of the density of states and the group velocity in a 1D system is constant, the current is now given by

$$I = \sum_{n=1}^{N_c} \int_0^\infty \frac{2e}{h}[f(E,\mu_s) - f(E,\mu_d)]T_n(E)dE. \tag{2.4}$$

As the transport is in the linear regime (small V_{sd}), the difference in the Fermi-Dirac distributions is given in first order approximation as

$$f(E,\mu_s) - f(E,\mu_d) \approx -eV_{sd}\frac{\partial f(E,\mu)}{\partial E}. \tag{2.5}$$

Considering for simplicity the case of zero temperature, equation 2.4 is reduced to

$$I = \sum_{n=1}^{N_c} \frac{2e^2 V_{sd}}{h} T_n(E_F), \tag{2.6}$$

and the conductance is given by

$$G = \sum_{n=1}^{N_c} \frac{2e^2}{h} T_n(E_F). \tag{2.7}$$

If we assume unity transmission probability for each mode, $T_n = 1$, then Eq. 2.7 for the conductance reduces to

$$G = \frac{2e^2}{h} N_c. \tag{2.8}$$

Each subband contributes $2e^2/h$ to the conductance (in the absence of a magnetic field). The quantized conductance plateaus are shown in Fig. 2.1b.

Possible causes for deviations from good quantization are tunneling, scattering and reflections of electron waves in the QPC. Reflections from, or tunneling through the top of the potential barrier is visible in the experimental data as smooth transitions from one conductance plateau to another, even at zero temperature. Reflections and scattering from irregularities in the saddle point potential may lead to unwanted resonances in the conductance plateaus.

2.2.1 The 0.7 anomaly

The shoulder in the conductance around $0.7(2e^2/h)$ in Fig. 2.1b is the so-called 0.7 anomaly. Even though this feature was present in the first measurement of quantized conductance [1] it is still not fully understood. Nevertheless its appearance is a clear sign of the importance of many-body effects in QPCs. In Chapter 3 of this thesis we study how the appearance of the 0.7 anomaly depends on the geometry of the point contact.

One of the most striking features of the 0.7 anomaly is its temperature dependence. Figure 2.2 shows experimental results of the conductance of a QPC at different temperatures. In several detailed experimental studies [4, 5, 6, 7] it was shown that the 0.7 anomaly becomes more pronounced at elevated temperatures. When the temperature is increased, the conductance plateaus at integer multiples of $2e^2/h$ become thermally smeared. The conductance at the shoulder on the left of the $2e^2/h$ plateau, however, reduces with increasing temperature, strengthening the appearance of the 0.7 anomaly. At $T = 4.2$ K the 0.7 anomaly is the only remaining feature in the conductance.

The 0.7 feature appears and has been investigated in many other device structures, like QPCs defined in two-dimensional hole systems [8] as well as in local-oxidation-defined QPCs [9]. Several models have been proposed that relate the 0.7 anomaly to a spontaneous spin splitting in zero magnetic field [10, 11], since the 0.7 plateau evolves continuously into the spin-resolved plateau at $0.5(2e^2/h)$ when an in-plane magnetic field is applied.

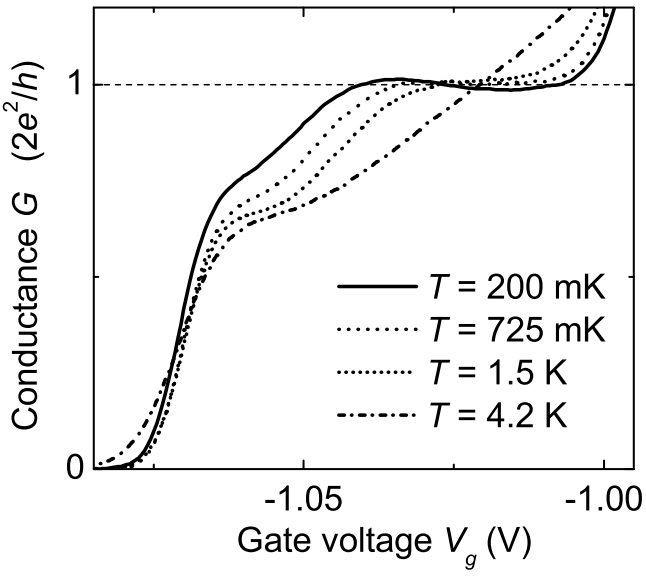

Figure 2.2: Conductance G of a QPC as a function of gate voltage V_g, shown for four different temperatures. With increasing temperature the shoulder on the conductance around $0.7(2e^2/h)$ becomes more pronounced.

2.2.2 External magnetic fields and non-linear transport

In a non-interacting electron picture, the application of a large magnetic field splits the spin degenerate 1-D subbands by the Zeeman energy, $\Delta E_z = g^*\mu_B B$, where g^* is the effective g-factor. The spin-resolved subbands each carry a conductance of e^2/h as is shown in Fig. 2.3. The magnetic field considered here is applied parallel with the plane of the 2DEG.

Figure 2.4a shows the differential conductance $G = \mathrm{d}I/\mathrm{d}V$ as a function of dc source-drain bias voltage, V_{sd}, at many different gate voltages, V_g. Each line is a measurement at a different V_g value. The plateaus in conductance appear as regions where many lines accumulate. In a large magnetic field of 9 T the spin-resolved plateaus are visible at multiples of e^2/h (Fig. 2.4b). At high bias the so-called half-plateaus appear in the differential conductance, when the number of transport modes available for left-going and right-going electrons differs by one, i.e. when the bottom of a subband dispersion (as shown in Fig. 2.1a) lies in between the chemical potentials of the reservoirs, μ_s and μ_d.

In these experiments we observe two features that are associated with many-body interactions but not fully understood. In Fig. 2.4a, the conductance peak around $V_{sd} \sim 0$ for $G < 2e^2/h$ is the zero-bias anomaly (ZBA). This peak is only

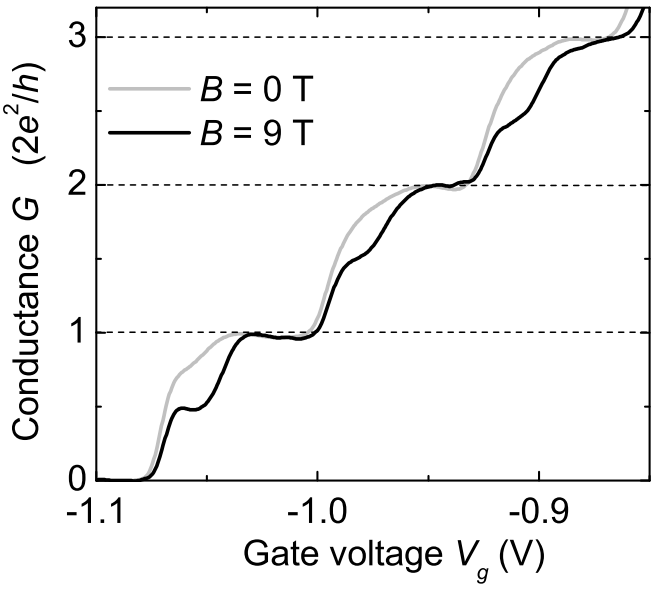

Figure 2.3: Conductance G of a QPC as a function of gate voltage V_g, shown for zero and high magnetic field. Additional plateaus appear at odd multiples of e^2/h in high magnetic field due to the Zeeman splitting of spin-degenerate subbands.

present at low magnetic fields and low temperatures. In the same figure, the plateaus at $0.8(2e^2/h)$ at high bias ($V_{sd} \sim \pm 1$ mV in the $B = 0$ data are also not expected in a non-interacting picture.

Figures 2.4c,d present the transconductance $\mathrm{d}G/\mathrm{d}V_g$ as a function of V_{sd} for 0 T and 9 T respectively. Transitions between plateaus appear in white whereas the black regions correspond to plateaus. The central diamond shapes in the plot in zero field (labeled in units of $2e^2/h$) and the high-bias half-plateaus can be understood from a non-interacting picture. A clear explanation of this plot with corresponding energy diagrams can be found in chapter 6 of Ref. [12]. The additional lines that appear near the bottom edge of the first integer plateau are again related to the 0.7 anomaly and cannot be explained in this non-interacting model. The data in high magnetic field shows the spin-resolved plateaus. These appear as small diamonds in between the larger diamonds that are labeled in units of $2e^2/h$.

This type of experiment is in particular useful to extract information about the energy splittings between the 1-D subbands (see also Ref. [12]) and to find a lever arm for converting gate voltage V_g scale into energy scale as described in Chapter 3 of this thesis.

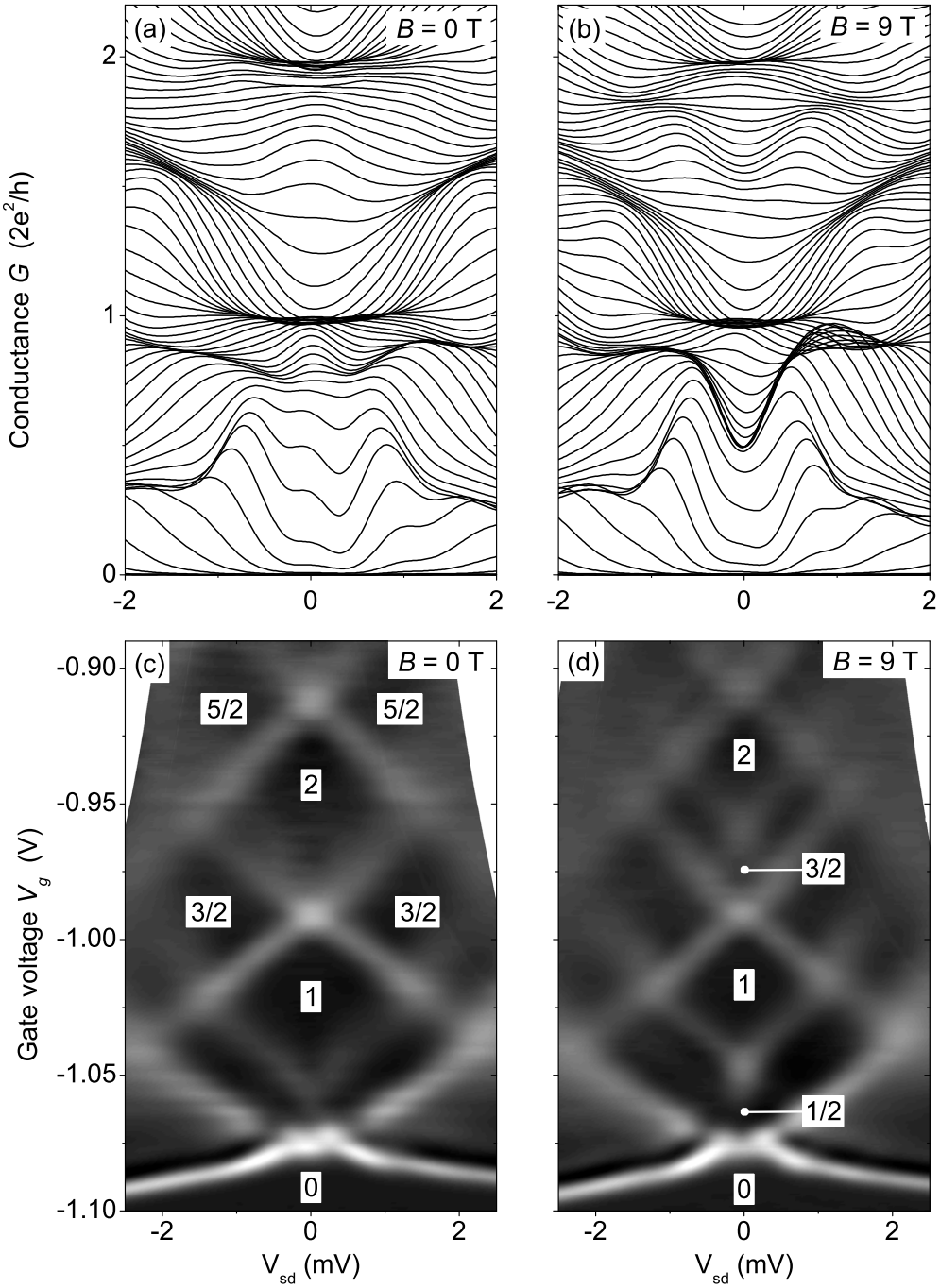

Figure 2.4: **(a)**, **(b)** Differential conductance G as a function of DC source-drain voltage V_{sd} for many different values of gate voltage V_g, shown for zero **(a)** and high magnetic field **(b)**. Plateaus appear as regions where many lines converge. **(c)**, **(d)** Derivative of the conductance with respect to gate voltage $\mathrm{d}G/\mathrm{d}V_g$ as a function of V_{sd} for many different values of gate voltage V_g, shown for zero **(c)** and high magnetic fields **(d)**. White lines indicate transitions between plateaus (black regions). The conductance plateaus are labelled in units of $2e^2/h$.

2.3 Quantum Dots

A Quantum Dot (QD) is a device where electrons are confined in all three directions and can contain any number from a single electron to thousands of electrons [13]. For the QDs in this thesis the confinement is realized using electrostatic depletion gates. Quantum Point Contacts (QPCs) are used as tunable contacts to the dot, connecting the dot to large 2DEG reservoirs. These enable electrical transport measurements on the dot.

The coupling to these reservoirs can be in the tunneling regime, where $G_{QPC} \ll 2e^2/h$, such that the dot is very weakly coupled to the reservoirs. On the other hand, the QPCs can also be tuned to carry one or more modes of conductance, $G \sim 2e^2/h$, such that electrons can enter and exit the dot without tunneling. Measurements in these regimes are often referred to as closed dot or open dot experiments respectively.

The number of electrons in the dot can simply be changed by changing the area within the lithographically defined depletion gates. The dots we are studying are so-called large QDs and contain up to thousands of electrons. These dots are however still sufficiently small to be in the ballistic regime, where edge scattering (scattering on the walls of the QD) is much more frequent than impurity scattering.

In practice, transport in large open QDs always shows mesoscopic fluctuations of the conductance, a characteristic that results from the interference of multiple transport paths through the sample [14, 15]. Any change in the QD system which affects the accumulation of the trajectory phase, such as a small change to the the shape with a gate voltage, or by changing the accumulated (Aharonov-Bohm) phase with a perpendicular magnetic field, will alter the interference pattern, resulting in random but repeatable conductance fluctuations as a a function of the external parameter. If you want to study average properties of our system, this requires that for each measurement we need to average over sufficient statistically independent samples.

Another important effect in this type of device is Weak Localization (WL). This is an interference effect of electron trajectories scattering back to their point of origin. When Time Reversal Symmetry (TRS) is not broken and coherence is not lost, the phase accumulated along these trajectories is exactly the same as the phase of the time reversed trajectories. This creates constructive interference, leading to an increased probability for the electron to remain at the origin, hence decreasing the conductance. If TRS is broken due to for instance a strong Spin-

Orbit (SO) field, the constructive interference can be suppressed or turned into destructive interference leading to a peak in conductance. This effect is called Weak Anti-Localization (WAL). These effects can and have been used to study the coherence time in open QDs [16, 17] and SO interaction in open QDs [18] and large area 2DEG systems [19]. In our type of experiment we are typically in the regime where TRS is broken, since in practice we always suppress WL when we apply a large in-plane magnetic field, due to a small perpendicular component of that magnetic field.

For measurement on large open QDs Coulomb Blockade (CB) effects are less important because the charging energy for electrons E_c decreases with increasing dot area A and can be much smaller than temperature. Further the level broadening Γ due to electrons entering and leaving the dot through the point contacts is larger than the spin degenerate mean level spacing Δ_m even for only a few modes in each point contact.

2.4 Device fabrication

2.4.1 GaAs/AlGaAs heterostructures

Fabrication of lateral structures like QPCs and quantum dots starts with a semiconductor heterostructure as shown in Fig. 2.5a. The stacked layers of GaAs and AlGaAs layers are grown by Molecular Beam Epitaxy (MBE). Dopants can be implanted during the growth process.

A 2-Dimensional Electron Gas (2DEG) forms by doping the n-AlGaAs layer with Si. The doping introduces free electrons that accumulate at the interface between the GaAs and the AlGaAs since there is a dip in the conduction band (see Fig. 2.5c). Due to the confinement in the z-direction, the energy levels in this triangular potential are quantized. The 2DEG is separated from the n-AlGaAs donor layer by an undoped AlGaAs buffer layer. This separation greatly reduces the scattering with the Si donors resulting in extremely high mobilities of the electrons in the 2DEG. Usually, the heterostructure is engineered such that only the first subband is occupied.

Figure 2.5b shows the effect of electrostatic gates on the electron gas below. This gating effect is typically realized by applying negative voltages to metal gates on top of the heterostructure.

We use heterostructures grown in the group of D. Reuter and A.D. Wieck at the Ruhr-Universität in Bochum, Germany. The sequence of the grown layers is

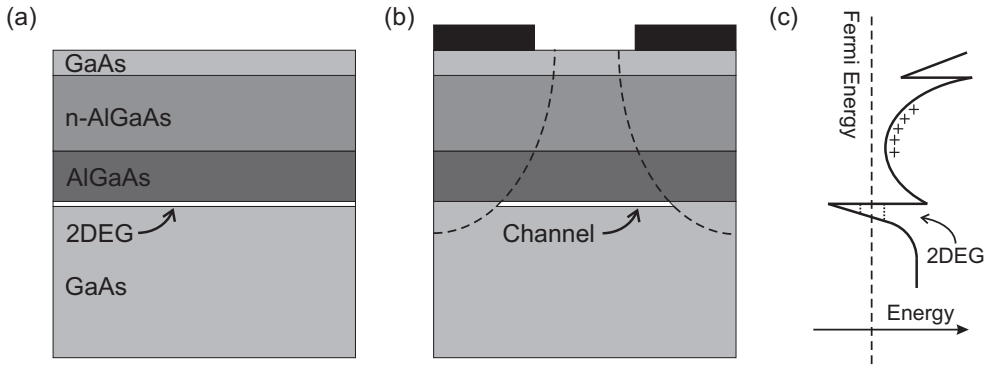

Figure 2.5: **(a)** Semiconductor heterostructure containing a 2DEG. **(b)** Electrons can be confined by applying negative voltages to gates on top of the wafer surface. The underlying 2DEG can then be fully depleted. **(c)** Energy band diagram for the conduction band of the heterostructure.

indicated in Fig. 2.5a. For most of the results presented in this thesis we used a heterostructure where the 2DEG is at 114 nm below the surface from modulation doping with Si. The buffer layer had a thickness of 36.8 nm and Si doping was about $n_{Si} \approx 1 \cdot 10^{24}$ m^{-3}. At 4.2 K, the mobility of the 2DEG was $\mu = 159$ m^2/Vs, and the electron density $n_s = (1.5 \pm 0.1) \cdot 10^{15}$ m^{-2}. In Chapters 6 and 7 we also present results where we have used another heterostructure from this group and a wafer purchased from Sumitomo Electric Industries, Inc. The specifications for all wafers can be found in Appendix A.

2.4.2 Electron beam lithography

The most important tool for fabrication of the devices presented in this thesis is Electron Beam Lithography (EBL). In essence it is the irradiation of a layer of an electron-sensitive polymer with a focused electron beam. The e-beam breaks the polymer chains in the resist and the exposed resist can then be selectively removed with a suitable solvent. The main advantages of EBL are high resolution and great flexibility. This general principle of EBL is depicted in Fig. 2.6.

The first EBL machines were developed in the late 1960s. Shortly thereafter it was found that polymethyl methacrylate (PMMA) made an excellent e-beam resist [20]. The resist layer that has to be used in the EBL process depends mainly on the thickness of the structure that is fabricated. In general, resists with a lower molecular weight are more sensitive to exposure and dissolve faster in a developer. Therefore the contrast of a resist becomes higher as the molecular weight of the

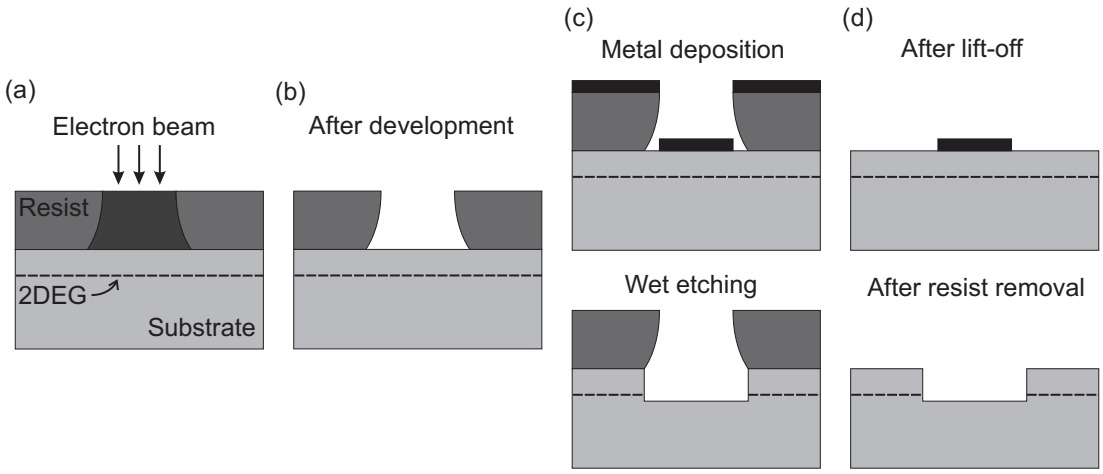

Figure 2.6: Electron beam lithography process to either define metal structures or to etch the surface of the heterostructure wafer. **(a)** Writing a pattern in the resist with an electron beam. **(b)** After development the exposed resist has been removed. **(c)** Evaporating metal (top figure) or wet etching (bottom figure). **(d)** After lift-off all resist, and all metal on top of that resist has been removed.

PMMA increases. To facilitate the spin coating of thin PMMA layers, the PMMA is diluted in solution.

Two different types of resist were used, 950k PMMA dissolved in chlorobenzene (2%) and 50k PMMA dissolved in ethyl-L-lactate (7%). The most common procedure is a bi-layer PMMA where the PMMA with the highest molecular weight is on top. Both layers are spin coated at 4000 rpm and then baked for 15 minutes at 170 °C. After exposure and development this results in the formation of an undercut of the bottom resist layer, which is important for a good lift-off. However for high-resolution patterns with a thickness less than $\sim$ 50 nm we use a single layer 950k PMMA resist. During ELB exposure, backscattered electrons from the substrate create an undercut even for a single layer of resist.

In our lab we use Raith E-line system for exposure. Typically we use an acceleration voltage of 10 keV, however for the high-resolution patterns we use 30 keV. The exposed polymer can be easily dissolved in a 1:3 solution of methyl-isobutyl-ketone (MIBK) and isopropanol (IPA). The developing process is stopped by rinsing in pure IPA. The unexposed resist remains unaffected. After further processing (like metal deposition or wet etching of the surface) all remaining resist and any material on top of that resist is removed using acetone. After this process, called lift-off, we rinse in IPA and spin-dry the sample.

2.4.3 Fabrication steps

The fabrication of devices used in this thesis required up to 5 fabrication steps. Each of these steps involves the writing of a specifically designed pattern using EBL as described in the previous section. Here we present shortly each of the steps, in Appendix B we describe the fabrication process in more detail.

Markers

The first fabrication step is the deposition of markers as shown in Fig. 2.7a. The marker pattern consists of 4 crosses in each corner of the device, where each line has a length of 50 μm and a width of 5 μm. A small square is added in a specific corner of the cross for easy recognition. These markers will be used for alignment in subsequent fabrication steps. We deposit Au with a thickness of 45 nm using a Ti sticking layer.

Mesa

The next step is the definition of a mesa by wet etching (Fig. 2.7b). Etching the heterostructure wafer is necessary to electrically isolate conducting regions of the device. This isolation is in principle achieved when all the Si donors in the n-AlGaAs layer are removed, since they provide the electrons to form the 2DEG. In practice we always etched below the 2DEG and also removed the AlGaAs spacer layer.

The etchant is $H_2SO_4 : H_2O_2 : H_2O$, a mixture of sulphuric acid, hydrogen peroxide and DI water, with a composition 1:1:50. This results in an etching rate of approximately 2 nm/s. The etching process is stopped by rinsing the sample in DI water. Finally we spin-dry the sample.

Ohmic contacts

Electrical contacts to the 2DEG are realized by thermal annealing of surface electrodes in the shape of bonding pads. These electrodes have an area of 150 by 150 μm^2 and are located at specific places near the edge of the mesa (Fig. 2.7c). We make sure that the edge of the ohmic contact intersects the mesa edge at several places, such that there can be no edge currents around an ohmic contact.

We deposit 150 nm of Au and Ge in a eutectic mixture of 88:12 wt% followed by a layer of Ni with a thickness of 30 nm and a layer of Au with a thickness of 20 nm. The melting temperature of the eutectic AuGe mixture is 363 °C. For

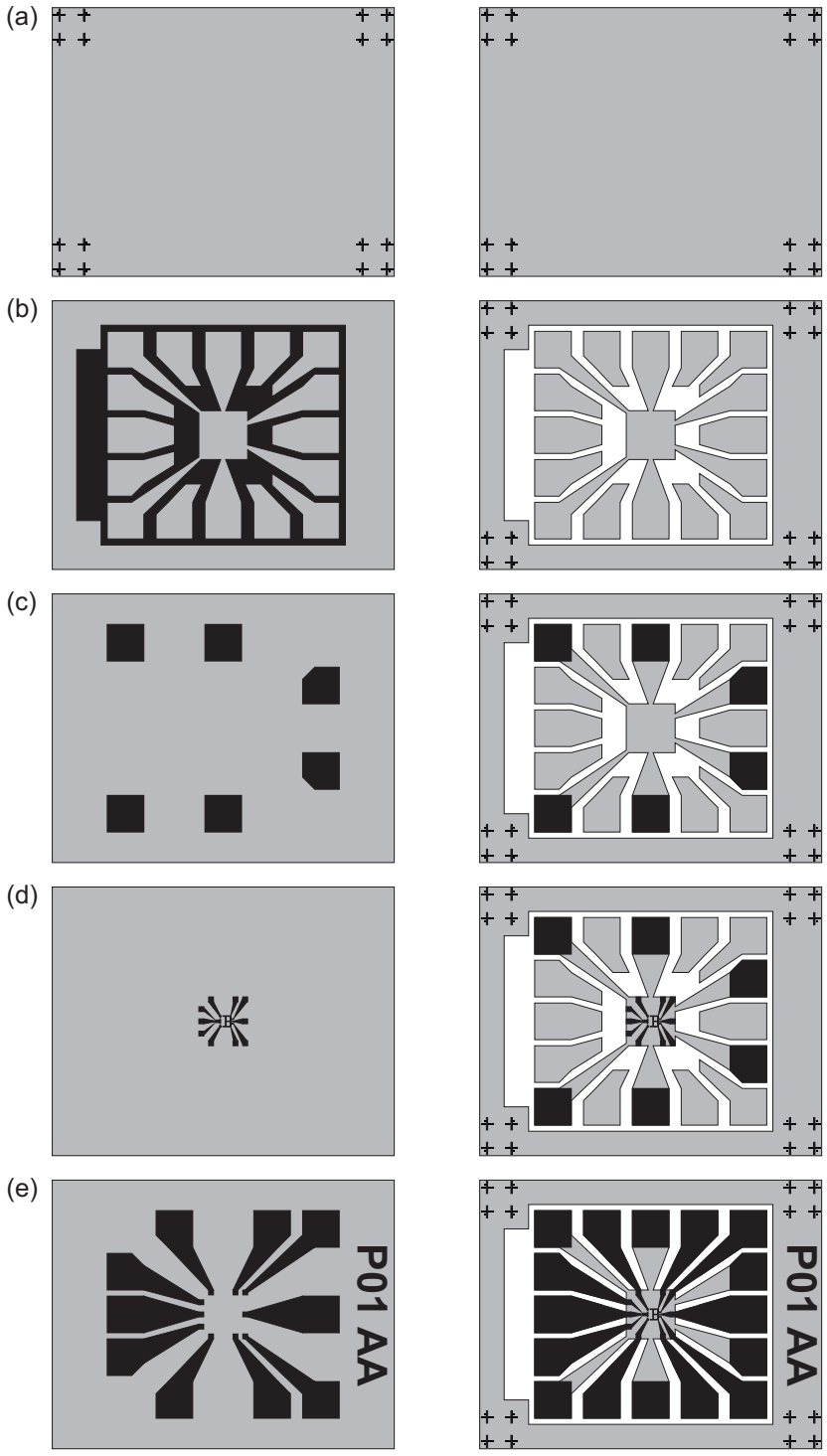

Figure 2.7: Electron beam lithography patterns for the fabrication of Quantum Point Contact and Quantum Dot devices. Each individual step is shown in the left image while the right image shows the sequential result for **(a)** alignment markers, **(b)** mesa etching, **(c)** ohmic contacts, **(d)** small gates (not to scale), and **(e)** large gates.

the annealing we use a quartz tube oven at 450 °C with an N_2 flow to prevent oxidation. Further, for devices that were accidentally annealed without an N_2 flow we have found that a conducting layer forms on the surface of the wafer.

During the annealing the electrodes melt and diffuse into the heterostructure wafer. The metal-rich phases penetrate into the wafer but do not actually reach the 2DEG. The Ge atoms form a highly doped region in between the diffused metal and the 2DEG, resulting in linear IV characteristics for the contact. At 4.2 K the contact resistance is typically well below 1 kΩ. The results of an in depth study on the fabrication of ohmic contacts can be found in chapter 7 of this thesis.

Fine gates

This step is the most critical step in the sample fabrication, since in this step the gates defining the quantum point contacts and quantum dots are made. The structures are defined in the center of the mesa as shown in Fig. 2.7d.

The pattern is written with a larger acceleration voltage for the electrons of 30 keV (compared to 10 keV for the other steps) to reduce proximity effects. We deposit 15 nm of Au with a Ti sticking layer. In this step the lift-off has to be done more carefully, typically the sample is left in heated acetone for several hours.

Large gates

The fabrication of the large gates is necessary to connect the fine gates to large bonding pads on the outside of the mesa (Fig. 2.7). We deposit a thick layer (typically 150 nm) of Au with a Ti sticking layer to overcome the height step of the mesa.

After the processing is finished, the sample is glued onto a chip carrier with varnish and bonding wires are attached to the bonding pads.

2.5 Measurement techniques

2.5.1 Dilution refrigerator

Our measurements are done at temperatures well below 1 K, in order to resolve very small energy differences. We use a ^{3}He/^{4}He dilution refrigerator purchased from Leiden Cryogenics, which has a base temperature less than 10 mK and

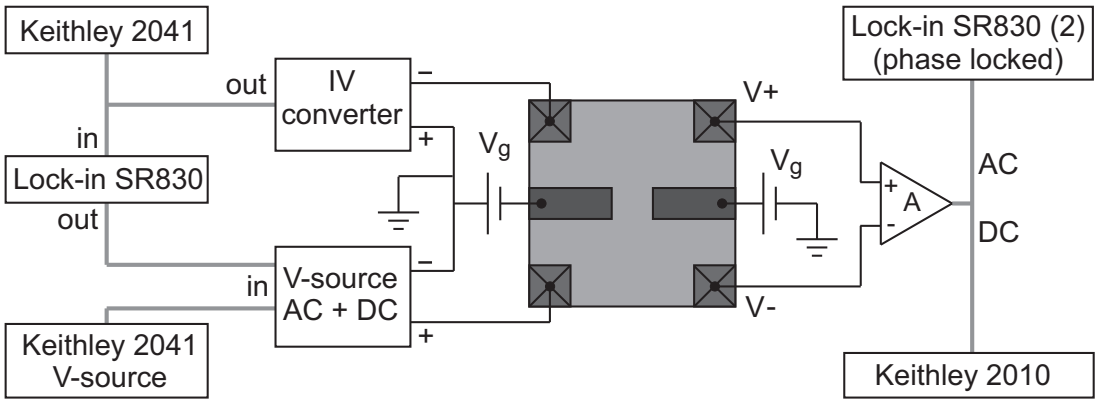

Figure 2.8: Circuit drawing of a 4-terminal voltage-bias measurement. Thin black wires carry very small signals at the sample level, connected to a clean ground and electrically isolated from the thick grey wires. These wires carry signals at the 1 V level that are connected to our measurement equipment.

a cooling power of about 1 mW at 100 mK. The sample is mounted onto a sample holder, thermally anchored to a cold finger, and inside a series of 3 copper cans that act as radiation shields. The sample holder is placed in the bore of a superconducting magnet that can apply a magnetic field up to 9 T.

2.5.2 Measurement electronics

Many properties of our devices can be studied by measuring the resistance $R = V/I$ or conductance $G = I/V$ of the device. In practice we mostly measured the differential resistance or differential conductance using a lock-in technique. There are two common measurement geometries to determine the resistance of a sample. One where a fixed current is passed through the device and the voltage drop is measured, or vice versa. This is called a current biased or voltage biased measurement respectively.

A voltage biased measurement is typically used when $R_{device} > e^2/h$, because all resistances in series with the sample add up to determine the current $I = V_{sd}/R_{total}$, where $R_{total} = R_{device} + R_{ohmics} + R_{wiring} + R_{IVconv}$. The input impedance of the IV converter $R_{IVconv} = 2$ kΩ for the most typical choice of the feedback resistance (10 MΩ). The sample resistance is ideally much larger than the other resistances in the set-up. Because in our measurements this requirement is not always met we use an additional set of voltage probes to determine the voltage drop across the device ΔV. Then the resistance of the device can be

determined as $R_{device} = \Delta V/I$.

An important condition for our measurements (in the linear regime) is that the voltage drop across the device V_{sd} is smaller than temperature $eV_{sd} < kT$. This can be achieved using a voltage biased measurement or by actively checking with a current biased measurement.

Here we will describe the 4-terminal voltage biased measurement as drawn in Fig. 2.8. The AC modulation voltage of an SR830 lock-in amplifier is used, if so desired together with a DC voltage from a Keithley 2041, to control the output of the voltage source. The inputs are passed through isolation amplifiers to isolate the sample electrically from the measurement electronics. An IV converter, or transimpedance amplifier, measures a voltage proportional to the current through the device. The non-inverting input (+) of the amplifier is grounded. Then its inverting input (-), although not connected to ground, will assume a similar potential, becoming a virtual ground. The AC component of the IV converter output is, after passing through an isolation amplifier, measured by the SR830 lock-in, the DC component is measured by the Keithley 2041. We typically use lock-in frequencies of 11 Hz for quantum dot measurements and 380 Hz for point contact measurements, and $V_{sd} = 10$ μV. Lower frequencies are required for the quantum dot experiments because there can be a large resistance in the voltage probe path.

The voltage difference measured by the two voltage probes on the right side of Fig. 2.8 is amplified by a factor 10 to 10^4 and measured by a second SR830 lock-in (phase locked to the first) and a Keithley 2010 multimeter. Voltages to the gates are applied via 8 Digital-to-Analogue Converters (DACs). These DACs are floating voltage sources where we connect the ground to the minus wire of the bias voltage source.

We use LabView to control the measurements. All signals are sent to the computer via a GBIP interface. This computer also controls the DAC outputs via an optical fiber.

2.5.3 Measurement wires and filtering

In between measurement electronics and the device, several filtering stages are required to ensure that the effective electron temperature is close to the lattice temperature. In practice the effective electron temperature is always higher due to interference and noise.

Four sets of 12 twisted pair manganin wires (making a total of 96 wires) with

a diameter of 0.13 mm run all the way from room temperature down to base temperature. To minimize the heat load on the mixing chamber, these wires are thermally anchored near the top of the IVC at 4.2 K, at the 1K pot ($\sim$ 1.5 K), at the still ($\sim$ 500 mK), at the 80 mK plate, and finally at the mixing chamber.

At room temperature all wires are connected to a pi-filter, or capacitor-input filter. This filter acts as a low-pass filter and consists of a 1.5 nF capacitor to ground, an inductive element in series and another 1.5 nF capacitor to ground. At the mixing chamber all wires go through copper powder filters [21]. These are copper tubes in which 4 measurement wires are wound, each with a length of $\sim$ 3 m. The tubes are then filled with copper powder to create a large contact area with the wires. The resistance of these wires, in combination with their stray capacitance, RC-filters high-frequency noise.

References

[1] B. J. van Wees *et al.*, Phys. Rev. Lett. **60**, 848 (1988).

[2] D. A. Wharam *et al.*, J. Phys. C **21**, L209 (1988).

[3] M. Büttiker, Phys. Rev. B **41**, 7906 (1990).

[4] K. J. Thomas *et al.*, Phys. Rev. Lett. **77**, 135 (1996).

[5] K. J. Thomas *et al.*, Phys. Rev. B **58**, 4846 (1998).

[6] A. Kristensen *et al.*, Phys. Rev. B **62**, 10950 (2000).

[7] S. M. Cronenwett *et al.*, Phys. Rev. Lett. **88**, 226805 (2002).

[8] R. Danneau *et al.*, Appl. Phys. Lett. **88**, 012107 (2006).

[9] L. P. Rokhinson, L. N. Pfeiffer, and K. W. West, Phys. Rev. Lett. **96**, 156602 (2006).

[10] R. Fitzgerald, Phys. Today **55**, 21 (May 2002).

[11] K. Ensslin, Nature Phys. **2**, 587 (2006).

[12] S. M. Cronenwett, Ph. D. Thesis, Stanford University (2001).

[13] L. Kouwenhoven and C.M. Marcus, Physics World **11**, 35 (1998).

[14] R. Washburn, R.A. Webb, Rep. Prog. Phys. **55**, 1311 (1992).

[15] C. M. Marcus *et al.*, Phys. Rev. Lett. **69**, 506 (1997).

[16] A.G. Huibers *et al.*, Phys. Rev. Lett. **81**, 200 (1998).

[17] A.G. Huibers *et al.*, Phys. Rev. Lett. **83**, 5090 (1999).

[18] D. M. Zumbühl *et al.*, Phys. Rev. Lett. **89**, 276803 (2002).

[19] J. B. Miller *et al.*, Phys. Rev. Lett. **90**, 76807 (2003).

[20] M. Hatzakis, J. Electrochem. Soc. **116**, 1033 (1969).

[21] J. M. Martinis, H. M. Devoret, and J. Clarke, Phys. Rev. B **35**, 4682 (1987).

Chapter 3

Many-body effects in quantum point contacts

Abstract

The conductance of a quantum point contact (QPC) shows several features that result from many-body electron interactions. The spin degeneracy in zero magnetic field appears to be spontaneously lifted due to the so-called 0.7 anomaly. Further, the g-factor for electrons in the QPC is enhanced, and a zero-bias peak in the conductance points to similarities with transport through a Kondo impurity. We report here how these many-body effects depend on QPC geometry. We find a clear relation between the enhanced g-factor and the subband spacing in our QPCs, and can relate this to the device geometry with electrostatic modeling of the QPC potential. We also measured the zero-field energy splitting related to the 0.7 anomaly, and studied how it evolves into a splitting that is the sum of the Zeeman effect and a field-independent exchange contribution when applying a magnetic field. While this exchange contribution shows sample-to-sample fluctuations and no clear dependence on QPC geometry, it is for all QPCs correlated with the zero-field splitting of the 0.7 anomaly. This provides evidence that the splitting of the 0.7 anomaly is dominated by this field-independent exchange splitting. Signatures of the Kondo effect also show no regular dependence on QPC geometry, but are possibly correlated with the splitting of the 0.7 anomaly.

This chapter is based on Refs. 6 and 7 on p. 131.

3.1 Introduction

A quantum point contact (QPC) is a short channel that carries ballistic one-dimensional electron transport between two reservoirs. Its conductance as a function of channel width is quantized [1, 2] and shows plateaus at integer multiples of $2e^2/h$, where e is the electron charge and h Planck's constant. This quantization of the conductance can be understood with a non-interacting electron picture. However, there are several features in the conductance that result from many-body interaction effects between electrons. The effective electron g-factor is enhanced and almost all semiconductor QPCs show an additional plateau at $\sim 0.7(2e^2/h)$, the so-called 0.7 anomaly. Further, electron transport through QPCs tuned to conditions where the 0.7 anomaly appears has similarities with transport through a Kondo impurity. These many-body effects are not yet fully understood, and in particular understanding the 0.7 anomaly has been the topic of on-going research for more than a decade now [3, 4]. A consistent picture of these effects is of interest for spintronics and quantum information proposals where QPCs are a key element, and QPCs are now also a key model system for studies of many-body physics in nanodevices.

Several models have been proposed that relate the 0.7 anomaly to a spontaneous spin splitting in zero magnetic field [5, 6, 7, 8, 9, 10, 11], since the 0.7 plateau evolves continuously into the spin-resolved plateau at 0.5 ($2e^2$/h) when an in-plane magnetic field is applied. A recent theory paper [12] presented spin-density functional calculations of realistic QPC geometries that show that a localized state can exist near pinch-off in a QPC, providing a theoretical background for the Kondo-like physics that was found experimentally [13]. Other studies have proposed electron-phonon scattering [14], Wigner crystal formation [15], or a dynamical Coulomb blockade effect [16] as the microscopic origin of the 0.7 anomaly. Graham *et al.* reported evidence that many-body effects also play a role in magnetic fields at crossings between Zeeman levels of different subbands [17], and at crossings of spin-split subbands with reservoir levels [18].

We report here how these many-body effects in QPCs depend on the QPC geometry. We study the energy spacing between the one-dimensional subbands and spin-splittings within one-dimensional subbands, both in zero field and high magnetic fields. While this type of data from individual devices has been reported before [6, 19], we report here data from a set of 12 QPCs with identical material parameters. Our measurements show a clear correlation between the subband spacing $\hbar\omega_{12}$ and the enhancement of the effective g-factor $|g^*|$. Both also depend

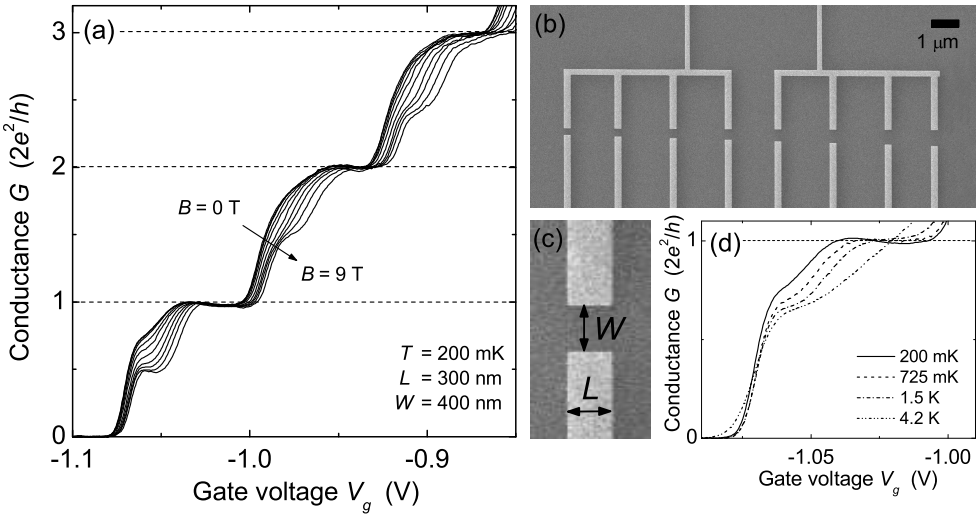

Figure 3.1: **(a)** The differential conductance G as a function of gate voltage V_g at 200 mK, for a QPC with $L = 300$ nm and $W = 400$ nm. The in-plane magnetic field is increased from $B = 0$ T to $B = 9$ T. The first three spin-degenerate plateaus at integer multiples of $2e^2/h$ for $B = 0$ T split into six spin-resolved plateaus integer multiples of e^2/h for $B = 9$ T. **(b)** Micrograph of a device containing 8 QPCs. From left to right the width W is increased, where W is defined as the spacing between the gate electrodes as shown in **(c)**. L is the length of the channel. Table 3.1 contains all values for L and W of the measured devices. **(d)** Differential conductance G as a function of gate voltage V_g at zero field for different temperatures. The 0.7 anomaly becomes more pronounced with increasing temperature.

in a regular manner on the geometry of the QPC, and we can understand this behavior using electrostatic modeling of the QPC potential.

The appearance of the 0.7 anomaly and signatures of the Kondo effect do not show a regular dependence on QPC geometry. Intriguingly, however, we find that in high magnetic fields there is a field-independent exchange contribution to the spin-splitting for the lowest one-dimensional subband in addition to the regular Zeeman splitting, and this exchange contribution is clearly correlated with the apparent zero-field splitting of the 0.7 anomaly. This new observation provides evidence that the apparent splitting of the 0.7 anomaly is dominated by this field-independent exchange splitting. The Kondo effect appears as a zero-bias peak in the differential conductance G, and the width of this peak is set by the Kondo temperature T_K, which represents the strength of the Kondo effect. Our measurements of T_K suggest a correlation between T_K and the 0.7 anomaly.

This chapter is organized as follows. Section 3.2 presents information about sample fabrication and measurement techniques. In section 3.3 we present measurements of the conductance of our set of QPCs, and we extract the energy splittings between subbands and spin splittings. In section 3.4 we focus on analyzing the signatures of many-body effects in our QPC data, before ending with concluding remarks in the last section.

3.2 Experimental realization

Our devices were fabricated using a GaAs/$Al_{0.32}Ga_{0.68}As$ heterostructure with a 2DEG at 114 nm below the surface from modulation doping with Si. The buffer layer had a thickness of 36.8 nm, and Si doping was about $n_{Si} \approx 1 \cdot 10^{24}$ m^{-3}. At 4.2 K, the mobility of the 2DEG was $\mu = 159$ m^2/Vs, and the electron density $n_s = (1.5 \pm 0.1) \cdot 10^{15}$ m^{-2}. A QPC is formed by applying a negative gate voltage V_g to a pair of electrodes on the wafer surface. The 2DEG below the electrodes is then fully depleted, and tuning of V_g allows for controlling the width of a short one-dimensional transport channel. Our QPCs had different values for the length L and width W for the electrode spacing that defines the device (see Table 3.1, and Figs. 3.1b,c). Note that W should not be confused with the actual width of the transport channel that is controlled with V_g. The depletion gates were defined with standard electron-beam lithography and lift-off techniques, using deposition of 15 nm of Au with a Ti sticking layer. The reservoirs were connected to macroscopic leads via Ohmic contacts, which were realized by annealing a thin Au/Ge/Ni layer that was deposited on the surface.

All QPCs were fabricated in close proximity of each other on a single central part of the wafer to ensure the same heterostructure properties for all QPCs. The set of 8 QPCs for which we varied L (Device 1 in Table 3.1) had all QPCs within a range of about 10 μm. The set of 8 QPCs for which we varied W (Device 2 in Table 3.1 and Fig. 3.1b) had an identical layout, and was positioned at 2 mm from Device 1. Thus, all semiconductor processing steps (resist spinning, e-beam lithography, metal deposition, etc.) could be kept nominally identical for all 16 QPCs. Electron-microscope inspection of the measured devices (after the measurements) confirmed that the dimensions of all gate electrodes were within 10 nm of the designed values (see table 3.1). In our data this appears as a very regular dependence of QPC properties (see for example the discussion of the pinch-off voltage V_{po} and subband spacing $\hbar\omega_{12}$ in the next session) on L and W for QPCs within the sets of Device 1 and 2. At the same time, two devices from

Device 1								
L (nm)	100	150	200	250	300	350	400	450
W (nm)	350	350	350	350	350	350	350	350
Device 2								
L (nm)	300	300	300	300	300	300	300	300
W (nm)	200	250	300	350	400	450	500	550

Table 3.1: Dimensions of the measured QPCs. The QPC length L and width W are defined as in Fig. 3.1c.

two different sets with nominally identical values of L and W (labeled (1) and (2) in Figs. 3.3 and 3.4) show slightly different QPC properties (in particular for the subband spacing $\hbar\omega_{12}$). This is not fully understood.

Measurements were performed in a dilution refrigerator with the sample at temperatures from ~ 5 mK to 4.2 K. For all our data the temperature dependence saturated when cooling below ~ 200 mK. We therefore assume for the data in this chapter that this is the lowest effective electron temperature that could be achieved. For measuring the differential conductance G we used standard lock-in techniques at 380 Hz, with an ac voltage bias $V_{ac} = 10\ \mu$V. Only the V_- contact was connected to the grounded shielding of our setup, and all gate voltages were applied with respect to this ground. The in-plane magnetic field was applied perpendicular to the current direction, and the current in the QPCs was along the [110] crystal orientation. Alignment of the sample with the magnetic field was within 1°, as determined from Hall voltage measurements on the 2DEG. We have data from 12 different QPCs from the set of 16 that we cooled down. From these QPCs 4 could not be measured. For two this was due to the presence of strong telegraph noise in conductance signals. Two other QPCs did not show clear conductance plateaus.

For analyzing QPC conductance values we subtracted a magnetic field and temperature dependent series resistance (from the wiring and filters, Ohmic contacts and 2DEG) from the transport data that was obtained with a voltage-bias approach. The criterium here was to make the observed conductance plateaus coincide with integer multiples of $2e^2/h$ or e^2/h.

3.3 Spin splitting and energy splitting between QPC subbands

3.3.1 QPC conductance and energy splittings

Figure 3.1a presents the differential conductance G of a QPC as a function of V_g, with the source-drain voltage $V_{sd} \approx 0$. Increasing V_g from pinch-off ($G = 0$) lowers and widens the saddle-point-like potential that defines the short transport channel. Consequently, an increasing number of one-dimensional subbands gets energies below the Fermi level. In zero magnetic field, this results in a step of $2e^2/h$ in the conductance each time an additional subband starts to contribute to transport. We label these spin-degenerate subbands with a number N, starting with $N = 1$ for the lowest subband. With a high in-plane magnetic field B the spin degeneracy within each subband $N = 1, 2, 3...$ is lifted, and the conductance increases now in steps of e^2/h.

We use this type of data to determine the energy splitting ΔE between spin-up and spin-down levels within the subbands $N = 1, 2, 3$, and the spacing $\hbar\omega_{12}$ between the $N = 1$ and $N = 2$ subband (a measure for the degree of transverse confinement in the channel). The onset of transport through a next (spin-polarized) subband appears as a peak in transconductance ($\mathrm{d}G/\mathrm{d}V_g$) traces as in Figs. 3.2a,c,e, which we derive from traces as in Fig. 3.1a. We assume that each subband contributes in a parallel manner to the QPC conductance, and the transconductance curves can then be analyzed as a superposition of peaks, with one (two) peak(s) per (spin-split) subband. We then determine the peak spacings ΔV_g along the V_g axis by fitting one or two peaks per subband on the transconductance traces (using least squares fitting with a Gaussian peak shape). The specific shape of a step between the quantized conductance plateaus depends on the shape of the saddle-point-like potential that defines the QPC [20], and can result in asymmetric transconductance peaks. We checked that this is not a significant effect for our analysis.

Subsequently, transconductance data (not shown) from non-linear transport measurements is used for converting ΔV_g values into energy splittings [21]. Here, the onsets of conductance plateaus appear as diamond shaped patterns in the $V_{sd} - V_g$ plane. The width of these diamonds along the V_{sd} axis defines the subband spacing, and we use this to determine the spacing $\hbar\omega_{12}$ between the $N = 1$ and $N = 2$ subband. The slopes of the diamonds can be used to convert a gate-voltage scale into energy scale [21]. In this analysis of $\hbar\omega_{12}$ and conversion

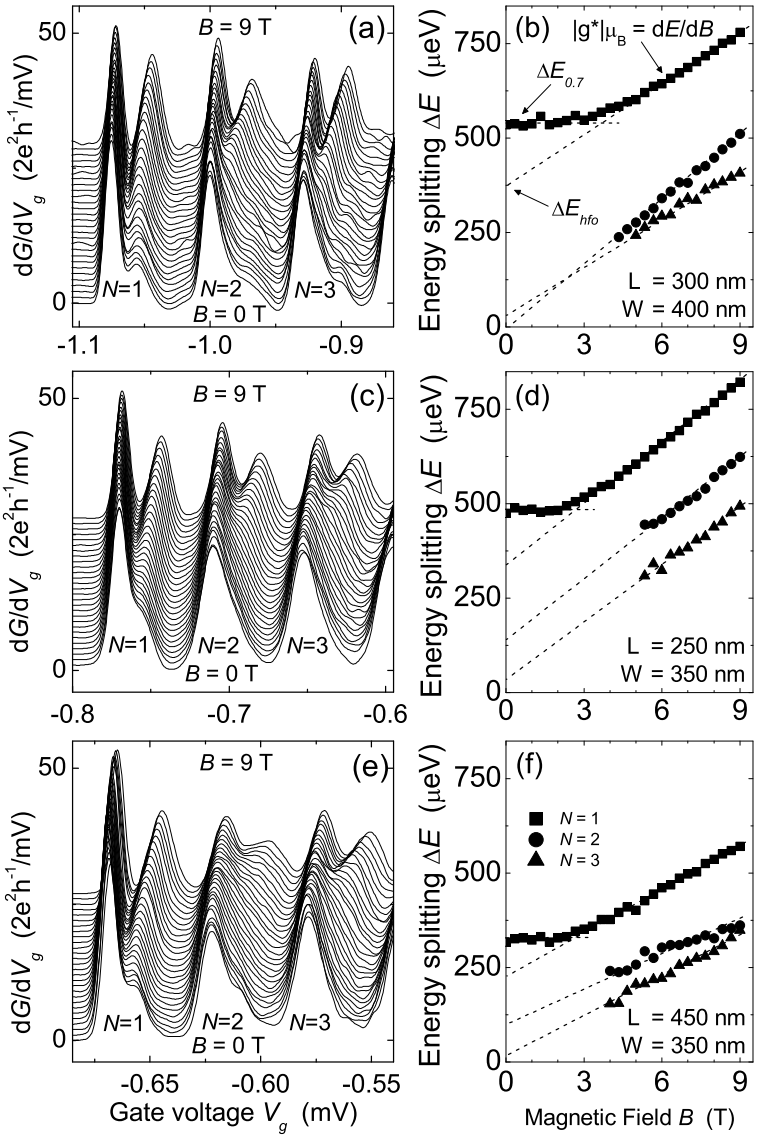

Figure 3.2: **(a)** Transconductance $\mathrm{d}G/\mathrm{d}V_g$ traces (offset vertically) obtained from the data in Fig. 3.1a (from the QPC with $L = 300$ nm and $W = 400$ nm). The 0.7 anomaly appears as a splitting of the transconductance peak for the $N = 1$ subband at $B = 0$ T. **(b)** Energy splittings ΔE obtained from the transconductance traces in **(a)**, as a function of magnetic field. The traces present ΔE for the subbands $N = 1, 2, 3$, see the legend in **(f)**. These ΔE traces are characterized (results presented in Fig. 3.4) with two or three parameters for each subband $N = 1, 2, 3$: An effective g-factor $|g^*|$, the offset from a linear Zeeman effect in high fields, characterized by the high-field offset ΔE_{hfo}, and for $N = 1$ at low fields the energy splitting of the 0.7 anomaly, $\Delta E_{0.7}$. See text for details. **(c)-(f)** Transconductance traces $\mathrm{d}G/\mathrm{d}V_g$ and energy splittings ΔE as in **(a)**, **(b)** obtained for a QPC with $L = 250$ nm and $W = 350$ nm in **(c)**, **(d)** and $L = 450$ nm and $W = 350$ nm in **(e)**, **(f)**. All data from measurements at 200 mK

of ΔV_g into spin splittings ΔE we observed a weak dependence on magnetic field and temperature, and took this in account.

The 0.7 anomaly is clearly visible in the data set presented in Fig. 3.1. The conductance trace for zero field in Fig. 3.1a shows besides pronounced steps of $2e^2/h$ an additional shoulder at $\sim 0.7(2e^2/h)$, which becomes more pronounced at higher temperatures (Fig. 3.1d). With increasing magnetic field, the 0.7 anomaly evolves into the first spin-resolved conductance plateau at e^2/h. In Figs. 3.2a,c,e the 0.7 anomaly appears as a zero-field splitting in the transconductance peak for $N = 1$, which evolves into two spin-split peaks in high fields. In earlier work this observation was the basis for assuming that the 0.7 anomaly results from a spontaneous removal of spin degeneracy in zero field [5, 6]. For the remainder of this chapter we will assume that the 0.7 anomaly is indeed related to such a spontaneous spin splitting, such that we can describe and characterize the splitting of the $N = 1$ transconductance peak in $B = 0$ in terms of an energy splitting ΔE between a spin-up and a spin-down subband. Note however, that this is an assumption, and that our experimental results do not provide evidence that the 0.7 anomaly is related to a spontaneous spin splitting. In particular, there is no evidence that such a splitting is related to a static ferromagnetic polarization, while the Kondo-like behavior of the 0.7 anomaly suggests that is could be a dynamical spin splitting [13]. In high fields, all 12 QPCs showed also for $N = 2$ and higher a pronounced spin splitting into two transconductance peaks, but these subbands did not clearly show a zero-field splitting.

We studied how the spin splittings ΔE for $N = 1, 2, 3$ increase with magnetic field from $B = 0$ T up to 9 T (Fig. 3.2b,d,f). We first concentrate on data for $N = 1$. At zero field ΔE shows the splitting associated with the 0.7 anomaly, that we label $\Delta E_{0.7}$. It is observed in all our QPCs with a typical value of 0.5 meV. At high fields ΔE has a linear slope similar to the Zeeman effect. However, linear extrapolation of this slope down to $B = 0$ shows that there is a large positive offset (unlike the usual Zeeman effect). We characterize the slope with an effective g-factor $|g^*| = \frac{1}{\mu_B}\frac{\mathrm{d}\Delta E}{\mathrm{d}B}$ (note that one should be careful to interpret $|g^*|$ as an absolute indication for the g-factor of electrons in a QPC, since different methods for extracting a g-factor can give different results [13, 19]). The high-field offset from a linear Zeeman effect is characterized with a parameter ΔE_{hfo}. Qualitatively, this type of data for ΔE looks similar for all 12 QPCs (Figs. 3.2b,d,f), and we use a suitable fitting procedure to characterize the traces for $N = 1$ with the parameters $\Delta E_{0.7}$, ΔE_{hfo} and $|g^*|$. Notably, two-parameter fitting using spin-$\frac{1}{2}$ energy eigenvalues with $\Delta E = \sqrt{(\Delta E_{0.7})^2 + (|g^*|\mu_B B)^2}$ does

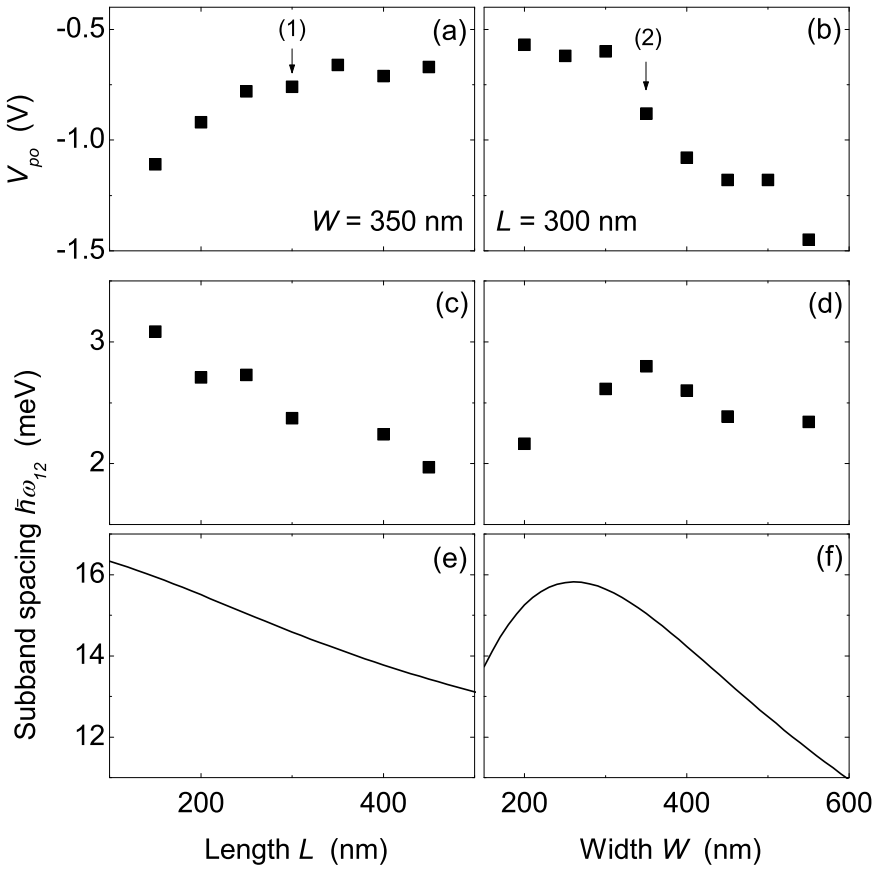

Figure 3.3: **(a)**,**(b)** The pinch-off voltage V_{po} as a function of QPC length L (with fixed width $W = 350$ nm), and as a function QPC width W (with fixed length $L = 300$ nm). Data points labeled with (1) and (2) are from two different devices with nominally identical values for L and W (see text for details). **(c)**,**(d)** The measured subband spacing $\hbar\omega_{12}$ as a function of L and W. **(e)**,**(f)** Calculated subband spacing $\hbar\omega_{12}$ as a function of L and W, from electrostatic modeling of the QPC potential. The results qualitatively reproduce the trend in the experimental data in **(c)**,**(d)**.

not yield good fits. For the traces as in Fig. 3.2b,d,f for $N = 2, 3$, we cannot resolve a spin splitting at low fields, only the parameters ΔE_{hfo} and $|g^*|$ can be derived. Further analysis of these results for $\Delta E_{0.7}$, ΔE_{hfo} and $|g^*|$ is presented in Section 3.4 on many-body effects.

3.3.2 Electrostatics and subband splitting

Figs. 3.3a,b present how the pinch-off voltage V_{po} (the value of V_g where the G starts to increase from zero) depends on QPC geometry. Figs. 3.3c,d presents

this for the subband spacing $\hbar\omega_{12}$, which provides a parameter for the strength of the transverse confinement in the QPC and is possibly of importance for several of the many-body effects in QPCs. The observed dependence of V_{po} on the QPC geometry (a more negative V_{po} for shorter and wider QPCs) agrees with the expected trend. This provides the first of several indications that part of the physics of our set of QPCs depends in a regular manner on L and W.

Furthermore, the variation of $\hbar\omega_{12}$ is in good agreement with an electrostatic analysis [22] of the degree of transverse confinement in the saddle-point-like potential of the QPC (presented in Figs. 3.3e,f). In summary, short and narrow QPCs yield the strongest transverse confinement (Figs. 3.3d-f). This is valid down to the point where the QPC width $W \lesssim 3d$ (where d the depth of the 2DEG below the wafer surface), which results in the maximum for $W = 350$ nm in Figs. 3.3d,f.

For this analysis, we calculate the confining electrostatic potential due to the depletion gates in the plane of the 2DEG. An important ingredient of the calculation is the threshold voltage V_t, which is the (negative) voltage that must be applied to a gate to reduce the electron density underneath it to zero,

$$V_t = -\frac{en_{2D}d}{\epsilon_r\epsilon_0}, \tag{3.1}$$

where n_{2D} is the 2DEG electron density (without gates) and d the depth of the 2DEG below the surface. We use the dielectric constant for GaAs $\epsilon = \epsilon_r\epsilon_0 = 12.9\epsilon_0$.

The subband spacing can be calculated from the transverse curvature of the saddle-point-like potential. However, this curvature changes with the applied gate voltage. Therefore, we calculate the curvature for all QPCs when the QPC is just pinched-off ($G = 0$), when the potential in the middle of the transport channel is equal to V_t. For these calculations we used the dimensions L, W and d of the measured devices. Qualitatively the trends in $\hbar\omega_{12}$ as a function of L and W are reproduced, but the calculated values for $\hbar\omega_{12}$ are significantly larger than the experimentally obtained values. From earlier work [22] it is known that it is hard to get quantitative agreement from this type of calculations. Furthermore, the maximum in $\hbar\omega_{12}$ versus W is found for a smaller value for W than we have observed experimentally, approximately when $W \sim 2d$.

The origin of differences between our simple calculations and experimental results is well understood. The treatment of the exposed surfaces between the depletion gates is an important aspect of the calculations. A different choice for the boundary condition of the exposed surface may result in a noticeable

difference in the confining potential [22, 23]. We used a so-called pinned-surface approach (because it is a simple analytical approach) where the Fermi level at the surface becomes pinned to the Fermi level in the 2DEG. However, a pinned surface requires charge to move from the 2DEG to the surface when the gate voltage is changed, in order to keep the surface potential constant. This process is strongly suppressed at low temperatures. Alternatively, the surface can be treated as a dielectric boundary, with a fixed charge density (frozen surface approach). Davies *et al.* [22] have compared the results for pinned and frozen surfaces and found that the maximum in $\hbar\omega_{12}$ shifts from $W \sim 2d$ to $W \sim 3d$ when a frozen surface is assumed instead of a pinned surface. This corresponds very well to the experimentally observed value of 350 nm. Furthermore, the model used here is based on the calculation of the electrostatic potential due to the gates alone. Other effects, as the contribution to the potential from donor ions and other electrons in the 2DEG are ignored. Self-consistent calculations [24] have shown that the values of $\hbar\omega_{12}$ decrease rapidly when electrons enter the conduction channel.

3.4 Many-body effects

3.4.1 Enhancement of the effective g-factor

Figures 3.4a,b present how the effective g-factor $|g^*|$ for $N = 1$ varies with L and W of the QPCs. It is strongly enhanced up to a factor ~ 3 with respect to the g-factor for bulk 2DEG material [25] (the temperature dependence of this $|g^*|$ data is shortly discussed in section 3.4.2). This has been observed before [6] and is attributed to many-body effects. Notably, the values of $|g^*|$ and $\hbar\omega_{12}$ in Figs. 3.3c,d are clearly correlated.

The enhancement of the effective g-factor has been explained in terms of exchange interactions (see [26] and references therein). Calculations of the exchange potential in a square (quantum well) confining potential have shown that the effective g-factor decreases when the 1D confining potential weakens and the 2D limit is approached [27]. For a harmonic confining potential, the results of this study predict that $|g^*|$ scales indeed with $\hbar\omega_{12}$. We observed this here for the lowest subband ($N = 1$) in dependence on QPC geometry. Earlier work [6] observed the same trend in a single QPC, using that the transverse confinement decreases with increasing subband index N.

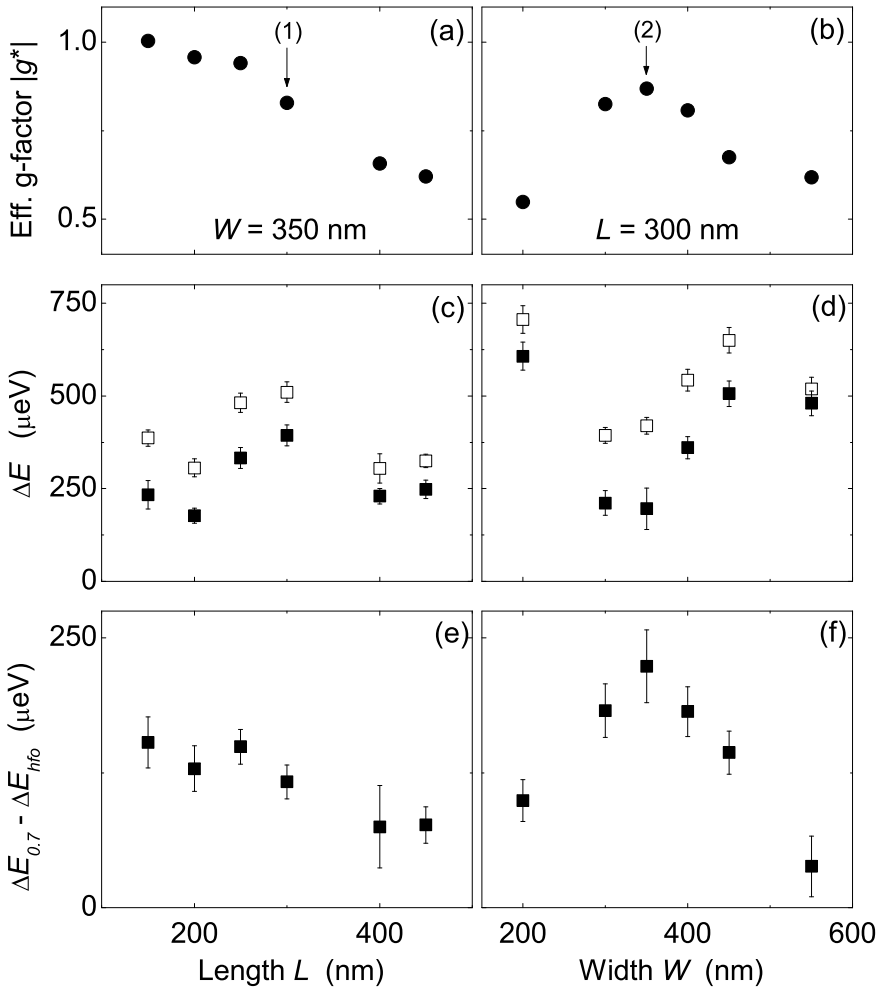

Figure 3.4: **(a)**,**(b)** Effective g-factor $|g^*|$ as a function of QPC length L (with fixed width $W = 350$ nm), and as a function QPC width W (with fixed length $L = 300$ nm). The effective g-factor $|g^*|$ is enhanced as compared to the bulk 2DEG value (up to a factor ~ 3) and shows a clear dependence on L and W, that is correlated with the dependence of the subband spacing $\hbar\omega_{12}$ in Fig. 3.3c,d. Data points labeled with (1) and (2) are from two different devices with nominally identical values for L and W (see text for details). **(c)**,**(d)** The 0.7 energy splitting $\Delta E_{0.7}$ and high-field offset ΔE_{hfo} for the $N = 1$ subband as a function of L and W. The values of $\Delta E_{0.7}$ and ΔE_{hfo} both vary with L and W in a irregular manner, but there is a strong correlation between $\Delta E_{0.7}$ and ΔE_{hfo}. **(e)**,**(f)** The difference between $\Delta E_{0.7}$ and ΔE_{hfo} as a function of L and W. This data again shows a correlation with the dependence of subband spacing $\hbar\omega_{12}$ on L and W. All data points are for the $N = 1$ subband from results measured at 200 mK. (Fig. 3.3c,d).

3.4.2 The 0.7 anomaly and exchange

Figs. 3.2b,d,f show that for all QPCs ΔE appears in high fields as the sum of the Zeeman effect and the constant contribution ΔE_{hfo}. This suggest that the splittings in high field have, in particular for $N = 1$, a significant contribution from a field-independent exchange effect that results from each subband being in a ferromagnetic spin-polarized state. In high fields such an interpretation is less ambiguous than for zero field (where the possibility of a ferromagnetic ground state for spin-polarized subbands is the topic of debate [28, 29]) since the Zeeman effect suppresses spin fluctuations. Thus, measuring ΔE_{hfo} can be used to determine this exchange splitting.

We now further analyze how this parameter ΔE_{hfo} and $\Delta E_{0.7}$ depend on L and W. The open squares in Figs. 3.4c,d present this for $\Delta E_{0.7}$. Overall, the dependence here is not very regular, possibly indicating that the exact appearance of the otherwise robust 0.7 anomaly is sensitive to small irregularities in the potential that defines the QPC (only the data in Fig. 3.4d suggests an anti-correlation with $\hbar\omega_{12}$). The black squares present how ΔE_{hfo} for $N = 1$ varies with L and W. Also here the dependence is irregular. Remarkably, however, the irregular variations of $\Delta E_{0.7}$ and ΔE_{hfo} are clearly correlated throughout our set of 12 QPCs. This means that $\Delta E_{0.7}$, which is derived from data in zero field, is correlated with ΔE_{hfo}, which is derived from data taken at fields in excess of 5 T. Further evidence for the significance of this correlation comes from data from the $N = 2$ and $N = 3$ subband (see Figs. 3.2b,d,f). We analyzed the data for $N = 2, 3$ in the very same way as for $N = 1$, and the most important observation is that the ΔE_{hfo} parameter for $N = 2, 3$ is much smaller than for $N = 1$, and often close to zero. A high ΔE_{hfo} value is only observed for $N = 1$, just as the 0.7 anamaly itself. Notably, for $N = 1$, $\Delta E_{0.7}$ and ΔE_{hfo} also have a similar order of magnitude. This analysis points to the conclusion that the spontaneous energy splitting of the 0.7 anomaly is dominated by the same effect that causes the high-field offset ΔE_{hfo}. As we discussed, this is probably an exchange contribution [30]. The error bar that we attribute to these values includes an error from the transconductance peak-fitting, one from the conversion of gate voltage to energy scale, and an error due to scatter in the ΔE datapoints as a function of B.

Fig. 3.4e,f presents data for the difference between $\Delta E_{0.7}$ and ΔE_{hfo}. Here, $\Delta E_{0.7} - \Delta E_{hfo}$ shows again a correlation with $\hbar\omega_{12}$. This indicates that the splitting of the 0.7 anomaly has (in addition to the exchange contribution that is also present in high fields) a contribution that scales with $\hbar\omega_{12}$. At this stage we cannot relate this new observation to earlier experimental or theoretical work.

Note that for the error bars in Figs. 3.4e,f we first subtracted the values of peak positions in terms of gate voltage, such that the error from gate voltage to energy scale conversion is accounted for only once.

We will now discuss the effect of increasing the temperature on the many-body phenomena in our QPCs. Figs. 3.5a-d show the conductance G at $V_{sd} \sim 0$ as a function of magnetic field for temperatures $T = 200$ mK, 450 mK, 825 mK, 1.5 K, 2.8 K and 4.2 K. As the temperature is increased the spin-degenerate plateaus and the spin-resolved plateaus both become less pronounced due to thermal smearing. In high magnetic fields the spin-resolved plateaus increase slightly in conductance with increasing temperature. At even higher temperatures the plateau at $0.7(2e^2/h)$ is the last remaining feature in the differential conductance. Notably, here the 0.7 anomaly appears to be present over the whole range of magnetic fields. The corresponding transconductance traces $\mathrm{d}G/\mathrm{d}V_g$ are plotted in Figs. 3.5e-h. As a result of the thermal smearing of the conductance plateaus, the peaks in $\mathrm{d}G/\mathrm{d}V_g$ become broader and decrease in height. The zero-field splitting in the transconductance peak for $N = 1$ has been identified as the 0.7 anomaly. When the temperature is increased, the 0.7 anomaly becomes more pronounced as was shown in the temperature dependence of the differential conductance G presented in Fig. 3.1d. Consequently the zero-field splitting in Figs. 3.5e-h also increases. For $T = 825$ mK and 1.5 K (Figs. 3.5f,g) even a small zero-field splitting of the $N = 2$ transconductance peak can be observed, suggesting the appearance of a $1.7(2e^2/h)$ plateau [6].

Using the temperature dependence of ΔE data (Fig. 3.6a), we find that the correlation between $\Delta E_{0.7}$ and ΔE_{hfo} remains intact at higher temperatures (Fig. 3.6c). Figure 3.6b shows that $|g^*|$ has a very different temperature dependence. This indicates that the g-factor enhancement and the 0.7 anomaly arise from different many-body effects.

3.4.3 Kondo signatures

The appearance of the 0.7 anomaly has been related to a peak in the differential conductance as a function of source-drain voltage around zero bias, for G values around e^2/h. Earlier work [13] showed that this zero-bias anomaly (ZBA), and its temperature and magnetic field dependence, have a very striking similarity with electron transport through a Kondo impurity that can be studied with quantum dots [31, 32]. For quantum dots, the Kondo effect is a many-body interaction of the localized electron(s) inside the dot with the delocalized electrons in the leads

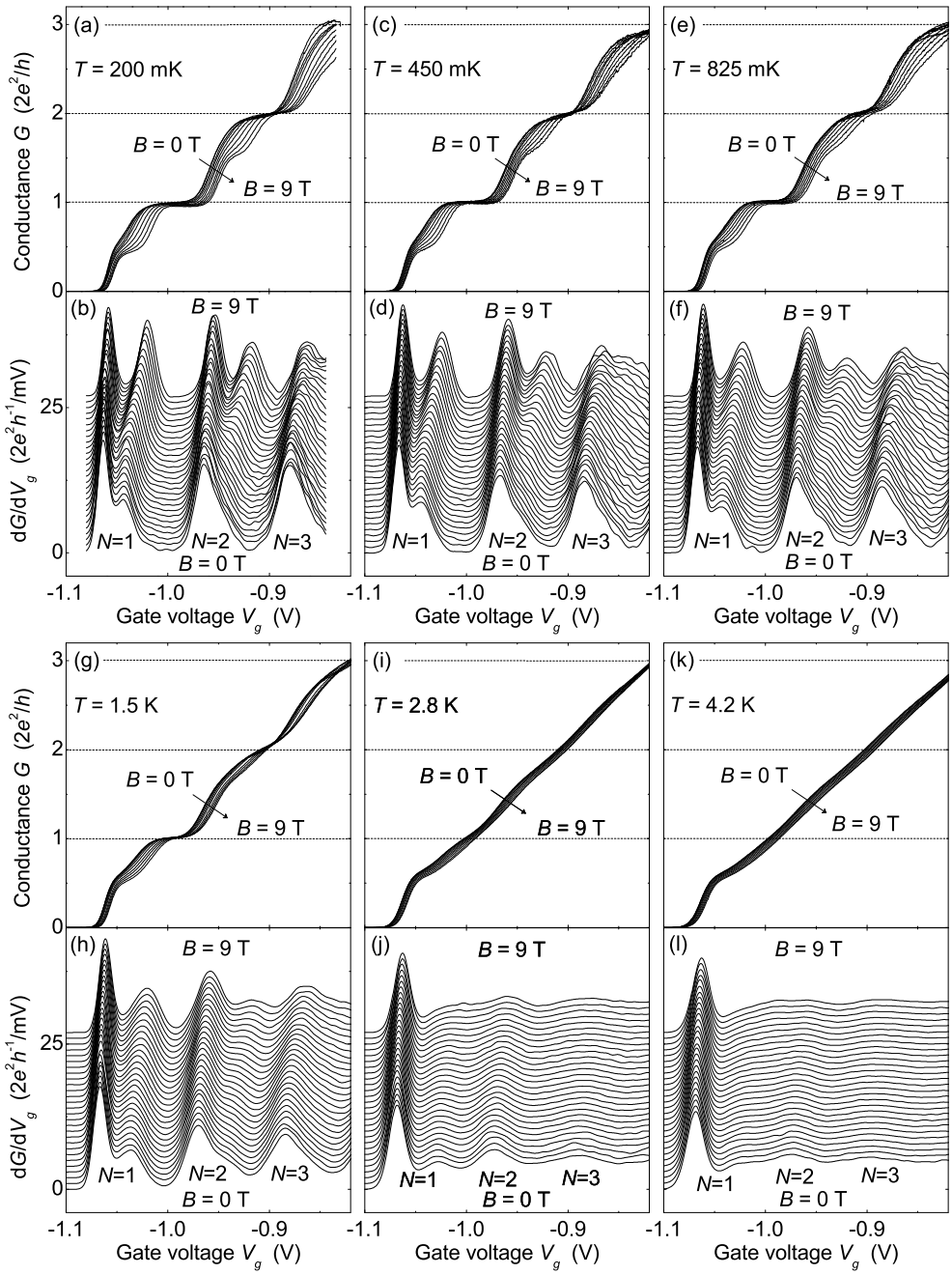

Figure 3.5: **(a)** Differential conductance G as a function of gate voltage V_g at 200 mK, for a QPC with $L = 300$ nm and $W = 400$ nm. The in-plane magnetic field is increased from $B = 0$ T to $B = 9$ T. **(b)** Transconductance $\mathrm{d}G/\mathrm{d}V_g$ traces (offset vertically for clarity) obtained by differentiating the data in (a). The conductance G and transconductance $\mathrm{d}G/\mathrm{d}V_g$ as in (a),(b) are shown for $T = 450$ mK in **(c)**,**(d)**, for $T = 825$ mK in **(e)**,**(f)**, for $T = 1.5$ K in **(g)**,**(h)**, for $T = 2.8$ K in **(i)**,**(j)** and for $T = 4.2$ K in **(k)**,**(l)**.

connected to the dot [31, 33, 32, 13]. Together these electrons form a spin-singlet state, effectively screening the local spin on the dot. In contrast to a quantum dot, where there is a clear localized state, a QPC is an open system where the formation of a bound state is much less obvious. A recent theoretical result [12] has shown that a self-consistent many-body state can indeed form inside a QPC, and that this can result in Kondo-like physics.

In this section we present the measurements of this ZBA in our set of QPCs. Most of our QPCs showed a clear ZBA in nonlinear conductance measurements. The temperature and magnetic field dependence of this data (Figs. 3.7a-d) is consistent with the earlier reports [13] that relate the 0.7 anomaly to transport through a Kondo impurity.

The relevant energy scale for Kondo physics is the Kondo temperature T_K. Below this temperature the magnetic impurity giving rise to Kondo physics is completely screened by the formation of a spin-singlet state and at zero-bias the differential conductance $G \cong 2e^2/h$. The Kondo temperature determines the width of the zero-bias peak. We observe that the peak width and height δG of the ZBA are not constant over the whole range $0 < \mathrm{G} < 2e^2/h$ (see also Fig. 6-12 in reference [19]). We choose to fit these parameters at $G \sim 0.3$, where the peak height has a relative maximum. The peak width and height are determined by fitting the non-linear conductance traces with a Gaussian shaped peak added to a parabola.

Figs. 3.7e,f show the peak width as a function of L and W (during our measurement run, one gate of Device 2 broke during an electronic malfunction, and we can only present data from 3 QPCs in the set with different values of W). The width of the ZBA does not show a clear dependence on L and W, and has a value of about 2 mV for all QPCs. For completeness, we also report the peak height δG in Figs. 3.7g,h as a function of L and W. We observe that for a single QPC δG varies with V_g, but the the values in Fig. 3.7g,h do give for each QPC a good representation of the typical value of δG throughout the V_g interval where the ZBA is observed. As a function of L and W, we observe here a stronger scatter in the values than for the peak width, but also here there is no clear relation with the QPC geometry. To conclude this section, we consider a correlation between the signatures of the Kondo effect and the values of $\Delta E_{0.7}$ (Fig. 3.7e,f). The irregular variation of the ZBA peak width with L and W suggests indeed a correlation with $\Delta E_{0.7}$, but here the evidence is very weak given the size of the error bar that we attribute to these values.

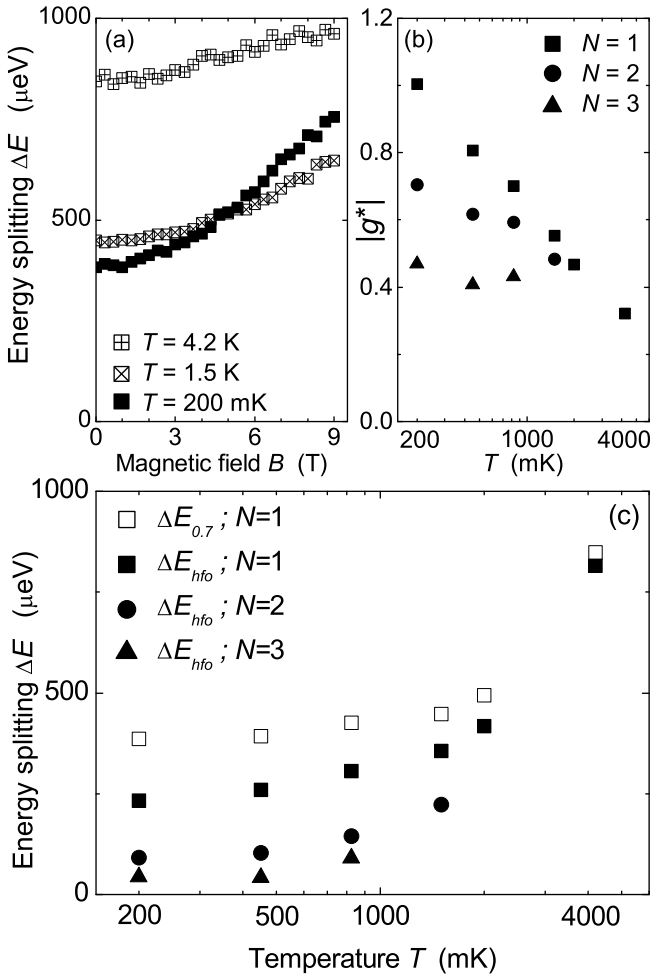

Figure 3.6: **(a)** Energy splitting for $N = 1$ as a function of magnetic field for different temperatures T, for a QPC with $L = 150$ nm and $W = 350$ nm. **(b)** Effective g-factor $|g^*|$ as a function of temperature for the same QPC. The g-factor enhancement is strongest for the $N = 1$ subband at the lowest temperature. For the $N = 2$ and $N = 3$ subband the g-factor is also enhanced at low temperatures. As the temperature is increased the g-factor enhancement is weaker for all subbands. **(c)** The 0.7 energy splitting $\Delta E_{0.7}$ and high-field offset ΔE_{hfo} as a function of temperature. The value for ΔE_{hfo} is highest for the $N = 1$ subband and decreases to zero with increasing subband number. As the temperature is increased, the $\Delta E_{0.7}$ value as well as the ΔE_{hfo} values for $N = 1, 2, 3$ strongly increase. The correlation between $\Delta E_{0.7}$ and ΔE_{hfo} remains present upon increasing the temperature.

3.5 Discussion and conclusions

We have studied many-body interaction effects in quantum point contacts. Our main point of interest was the dependence of these many-body electron interac-

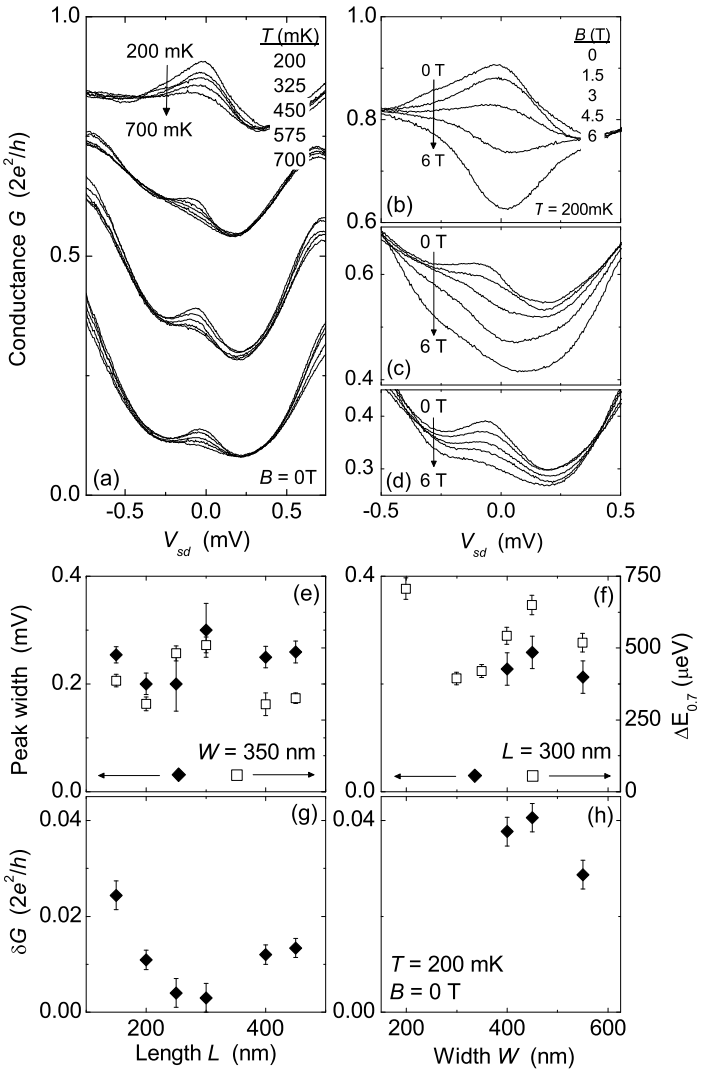

Figure 3.7: **(a)** Temperature dependence of the zero-bias anomaly (ZBA) for 4 fixed values of the gate voltage. The peak becomes more pronounced as temperature is lowered from 700 to 200 mK. **(b)-(d)** Magnetic field dependence of the ZBA for $G \sim 0.8$ (b), $G \sim 0.5$ (c) and $G \sim 0.3(2e^2/h)$ (d). The ZBA should split by upon application of an in-plane magnetic field [32, 13]. The peak in **(b)** does not split but collapses with B because $T_K < 2g^*\mu_B B$ in this regime [13]. The splitting in **(c)** and **(d)** is not very prominent, possibly due to our electron temperature of ~ 200 mK. **(e)**,**(f)** The width of the ZBA at $G \sim 0.3(2e^2/h)$ (left axis) as a function of QPC length L and width W. The peaks are fitted in zero magnetic field at $T = 200$ mK. The right axis shows $\Delta E_{0.7}$ (data from Figs. 3.4g,h). **(g)**,**(h)** Height of the ZBA also at $G \sim 0.3(2e^2/h)$ versus L and W for the same conditions as in **(e)**,**(f)**.

tions on the geometry of the QPC. We found a clear relation between the subband spacing and the enhancement of the effective electron g-factor. These parameters depend on geometry in a regular manner that we can understand from electrostatic modeling of the QPC potential. The many-body electron physics that causes the apparent energy splitting of the 0.7 anomaly does not show a clear dependence on QPC geometry, but we do find a clear correlation with a field-independent exchange effect that contributes to spin splittings in high magnetic fields. This suggests that the splitting of the 0.7 anomaly is dominated by this exchange contribution. We also measured a zero-bias anomaly in the non-linear conductance of our QPCs, that has been interpreted as a signature of the Kondo effect. Here, there is also no clear dependence on QPC geometry, but our data suggests that it is worthwhile to further study its correlation with the splitting of the 0.7 anomaly. These results are important for theory work that aims at developing a consistent picture of many-body effects in QPCs, and its consequences for transport of spin-polarized electrons and spin coherence in nanodevices. Our analysis of experimental data is very phenomenological, presenting parameters and correlations for which it is difficult to draw conclusions about the underlying physics. At the same time, part of state-of-the-art theory work now relies on numerical simulations of realistic QPC geometries (using spin-density-functional theory [12, 29] or other numerical approaches [28]) from which it is hard to derive analytical expression for the underlying physics. However, the validity of this numerical modeling can be easily tested for its consistency with the parameters and correlations that we reported here.

References

[1] B. J. van Wees *et al.*, Phys. Rev. Lett. **60**, 848 (1988).

[2] D. A. Wharam *et al.*, J. Phys. C **21**, L209 (1988).

[3] R. Fitzgerald, Phys. Today **55**, 21 (May 2002).

[4] K. Ensslin, Nat. Phys. **2**, 587 (2006).

[5] K. J. Thomas *et al.*, Phys. Rev. Lett. **77**, 135 (1996).

[6] K. J. Thomas *et al.*, Phys. Rev. B **58**, 4846 (1998).

[7] A. Kristensen *et al.*, Phys. Rev. B **62**, 10950 (2000).

[8] Y. Meir, K. Hirose, and N. S. Wingreen, Phys. Rev. Lett. **89**, 196802 (2002).

[9] A. A. Starikov, I. I. Yakimenko, and K.-F. Berggren, Phys. Rev. B **67**, 235319 (2003).

[10] D. J. Reilly, Phys. Rev. B **72**, 033309 (2005).

[11] L. DiCarlo *et al.*, Phys. Rev. Lett. **97**, 036810 (2006).

[12] T. Rejec and Y. Meir, Nature **442**, 900 (2006).

[13] S. M. Cronenwett *et al.*, Phys. Rev. Lett. **88**, 226805 (2002).

[14] G. Seelig and K. A. Matveev, Phys. Rev. Lett. **90**, 176804 (2003).

[15] K.A. Matveev, Phys. Rev. Lett. **92**, 106801 (2004).

[16] B. R. Bulka *et al.*, J. Phys.: Condens. Matter **19**, 255211 (2007).

[17] A. C. Graham *et al.*, Phys. Rev. Lett. **91**, 136404 (2003).

[18] A. C. Graham *et al.*, Phys. Rev. B **72**, 193305 (2005).

[19] S. M. Cronenwett, PhD thesis, Stanford University (2001).

[20] M. Büttiker, Phys. Rev. B **41**, 7906 (1990).

[21] N. K. Patel *et al.*, Phys. Rev. B **44**, 10973 (1991).

[22] J. H. Davies and I. A. Larkin, J. Appl. Phys. **77**, 4504 (1995).

[23] M. Chen, W. Porod, and D.J. Kirkner, J. Appl. Phys. **75**, 2545 (1993).

[24] S.E. Laux, D.J. Frank, and F. Stern, Surf. Sci. **196**, 101 (1988).

[25] R. M. Hannak *et al.*, Solid State Commun. **93**, 319 (1995).

[26] I. Pallecchi *et al.*, Phys. Rev. B **65**, 125303 (2002).

[27] A. Majumdar, J. Appl. Phys. **83**, 297 (1998).

[28] A. D. Klironomos, J. S. Meyer and K. A. Matveev, Europhys. Lett. **74**, 679 (2006).

[29] P. Jaksch, I. Yakimenko, and K.-F. Berggren, Phys. Rev. B **742**, 235320 (2006).

[30] E. J. Koop *et al.*, arXiv:0706.0792v1 [cond-mat.mes-hall] (2007).

[31] D. Goldhaber-Gordon *et al.*, Nature **391**, 156 (1998).

[32] S.M. Cronenwett, T.H. Oosterkamp, and L.P. Kouwenhoven , Science **281**, 540 (1998).

[33] L.P. Kouwenhoven and L.I. Glazman, Physics World **14**, 33 (2001).

Chapter 4

Spin accumulation and spin relaxation in a large open quantum dot

Abstract

We report electronic control and measurement of an imbalance between spin-up and spin-down electrons in micron-scale open quantum dots. Spin injection and detection was achieved with quantum point contacts tuned to have spin-selective transport, with four contacts per dot for realizing a non-local spin-valve circuit. This provides an interesting system for studies of spintronic effects since the contacts to reservoirs can be controlled and characterized with high accuracy. We show how this can be used to extract in a single measurement the relaxation time for electron spins inside a ballistic dot ($\tau_{sf} \approx 300$ ps) and the degree of spin polarization of the contacts ($P \approx 0.8$).

This chapter is based on Ref. 5 on p. 131.

4.1 Introduction

The ability to control and detect the average spin orientation of electron ensembles in non-magnetic conductors lies at the heart of spintronic functionalities [1]. We report here electronic control and detection of spin accumulation –an imbalance between the chemical potential of spin-up and spin-down electrons– in a large ballistic quantum dot in a GaAs heterostructure. We use quantum point contacts (QPCs) to operate a four-terminal quantum dot system, which is suited for realizing a non-local spin-valve circuit [2]. Before, such spin-valve circuits were realized with ferromagnetic contacts on various non-magnetic conductors [2, 3, 4], but for these systems it is hard to characterize the contact properties. An interesting aspect of our spintronic system is that it is realized with ultra-clean non-magnetic materials, while each spin-selective mode in the contacts can be controlled individually. We demonstrate that this can be exploited to measure and unravel for a single device the spin relaxation rate inside the dot, contributions to spin relaxation from coupling the dot to reservoirs, and the degree of polarization for spin-selective transport in the contacts. Thus, we report here the spin relaxation time for two different confinement geometries. Chaotic scattering inside such ballistic cavities can result in a spin relaxation mechanism that differs from that of bulk materials and very small few-electron quantum dots [5], but its full understanding is still a challenge to the community [6].

Figure 4.1a presents our device. Depletion gates on a heterostructure with a two-dimensional electron gas (2DEG) below the surface are used to define the four-terminal dot. QPCs are operated as spin-selective contacts, using that the subbands that carry the ballistic transport can be Zeeman split with a strong in-plane magnetic field, and that these modes can be opened up one by one by tuning gate voltages [7, 8]. The conductance of QPCs then increases in steps, with plateaus at Ne^2/h, where N the number of open modes. For odd (even) N the last opened mode carries only spin-up (spin-down). For the most typical form of our experiment we tune to the following setting. The QPC to the $I+$ reservoir has a single open mode, which is only available for spin-up electrons, while the $I-$ QPC is tuned to carry one mode for spin-up and one for spin-down, and we apply here a current I_{bias}. The contact resistance for electrons entering the dot via $I-$ is equal for spin-up and spin-down, while the current that leaves the dot carries only spin-up. Consequently, the chemical potential for spin-down electrons inside the dot will become higher than that for spin-up, up to a level that is limited by spin relaxation. This difference in chemical potential $\Delta\mu_{\uparrow\downarrow}$ can

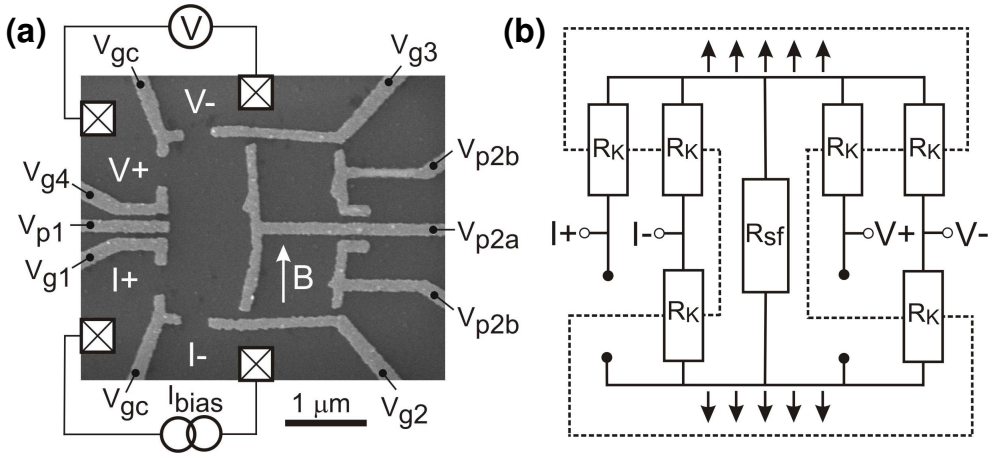

Figure 4.1: **(a)** Electron microscope image of the device, with labels for current and voltage contacts, and depletion gates V_{gi} and V_{pi}. Gate V_{p1} is a shape distorting gate. Fully switching gate V_{p2a} or gates V_{p2b} on or off sets the overall size of the dot, but fine tuning these gates is also used for controlling small shape distortions. **(b)** Resistor model for the most typical experiment (see text), for the case of ideal spin polarization of the contacts to the $I+$ and $V+$ reservoirs. The spin-up (top) and spin-down (bottom) populations inside the dot are contained within the dashed line. The spin-flip resistance R_{sf} represents spin relaxation inside the dot.

be measured as a voltage: with the $V+$ QPC tuned to have only one open mode for spin-up and the $V-$ QPC tuned to have one open mode for spin-up and one for spin-down, the voltage is $V = \Delta\mu_{\uparrow\downarrow}/2e$, which is for linear response expressed as a non-local resistance $R_{nl} = V/I_{bias}$.

4.2 Resistor Model

The resistor model in Fig. 4.1b is useful for analyzing how spin-relaxation mechanisms influence the measured signal in the above experiment. Each open mode for spin-up in a QPC is modeled as a resistor with value $R_K = h/e^2$ to the spin-up population in the dot, and similar for spin-down (we assume first perfect polarization of QPCs tuned to be spin selective). Spin-relaxation *inside* the dot is modeled as a resistor R_{sf} that carries a current from the spin-up to the spin-down population. Figure 1b illustrates that the contacts to the $I-$ and the $V-$ reservoir provide additional current paths for relaxation parallel to R_{sf} (spins rapidly mix in reservoirs, and reservoirs always have zero spin-accumulation).

This mechanism for spin relaxation *outside* the dot causes that in the limit of $R_{sf} \to \infty$ (no relaxation inside the dot), R_{nl} is limited to $R_K/4$. The voltage that is driving the relaxation inside the dot is $\Delta\mu_{\uparrow\downarrow}/e$, while the current through R_{sf} is $I_{sf} = e\Delta\mu_{\uparrow\downarrow}/2\Delta_m\tau_{sf}$, such that the spin-flip time τ_{sf} dictates R_{sf} according to $R_{sf} = 2\tau_{sf}\Delta_m/e^2$ [9]. Here $\Delta_m = 2\pi\hbar^2/m^*A$ is the mean energy spacing between spin-degenerate levels in a dot of area A. Consequently, measuring R_{nl} and deriving R_{sf} from its value can be used for determining τ_{sf}. While this resistor model does not account for various mesoscopic effects that occur in ballistic chaotic quantum dot systems, a theoretical study of an equivalent two-terminal spintronic dot [6] showed that it is valid in the regime that applies to our experiment (no influence of weak-localization and Coulomb blockade effects), and we indeed find that it is consistent with the measured spin signals that we report.

4.3 Experimental realization

The dot was realized in a GaAs/$Al_{0.32}Ga_{0.68}$As heterostructure with the 2DEG at 114 nm depth. At 4.2 K, the mobility was $\mu = 159$ m^2/Vs and the electron density $n_s = (1.5 \pm 0.1) \cdot 10^{15}$ m^{-2}. For gates we used electron-beam lithography and lift-off techniques, and deposition of 15 nm of Au on a Ti sticking layer. The reservoirs were connected to wiring via Ohmic contacts, which were realized by annealing Au/Ge/Ni from the surface. All measurements were performed in a dilution refrigerator at an effective electron temperature $T_{eff} \approx 100$ mK. For measuring R_{nl} we used lock-in techniques at 11 Hz with a current bias, where we made sure that the associated bias voltage $V_{bias} \leq 10$ μV. We carefully checked that RC-effects did not influence R_{nl} results. We used the T-shaped gate V_{p2a} or pair of gates V_{p2b} for setting the *overall size* of the dot (not to be confused with tuning small shape distortions for averaging out fluctuations, see below) at either an area of 1.2 μm^2 or 2.9 μm^2 (accounting for a depletion width of $\sim$ 150 nm around the gates).

4.4 Results of non-local experiments

Before presenting measurements of spin accumulation, we discuss two effects that make this experiment in practice less straight forward than in the above description. Quantum fluctuations in R_{nl} due to electron interference inside the dot [10] have an amplitude that is comparable to the spin signal [11], and R_{nl} can only be studied as a spin signal after averaging over a large number of fluctuations. The

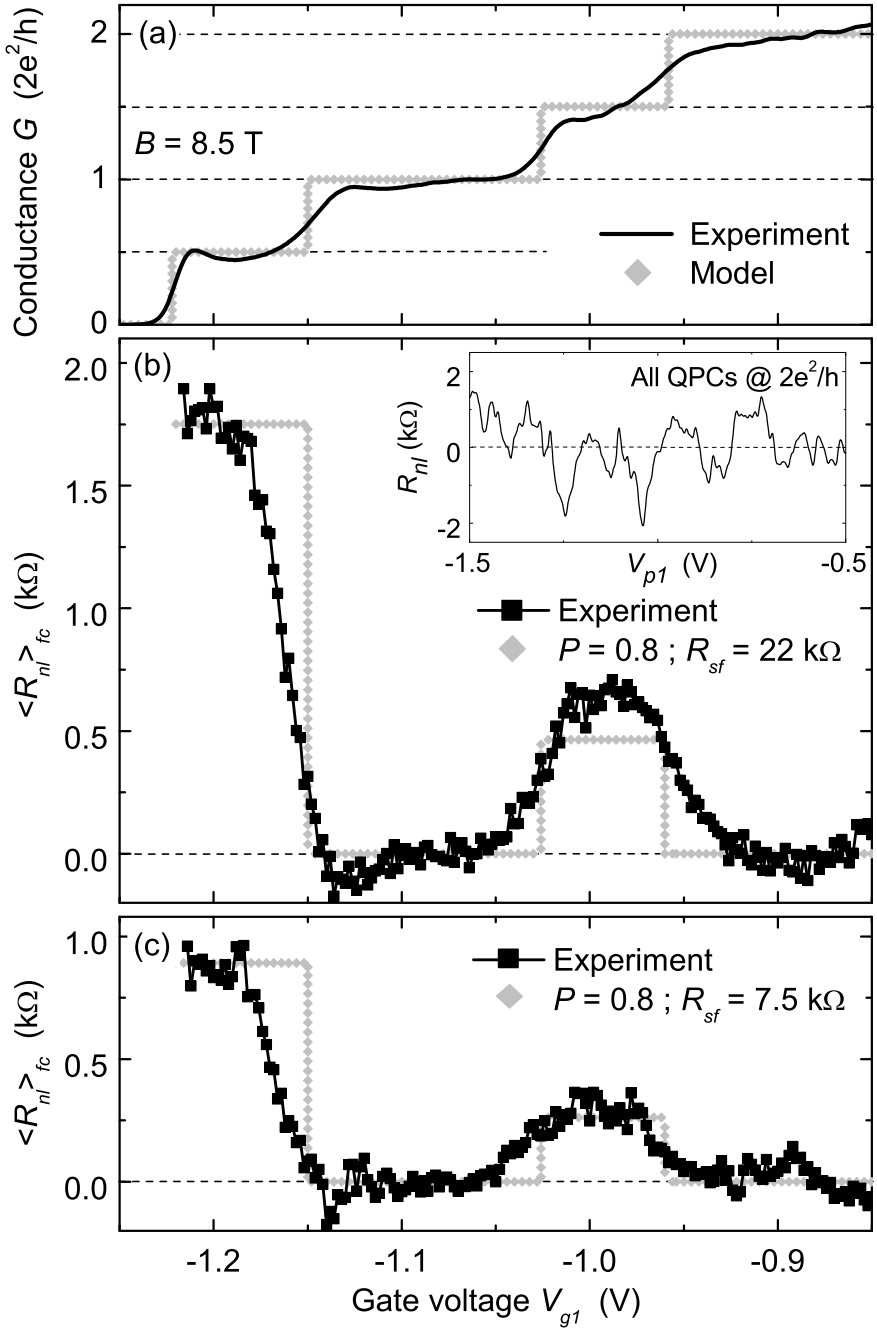

Figure 4.2: **(a)** Conductance G of the QPC to the $I+$ reservoir as a function of gate voltage V_{g1}, measured at $B = +8.5$ T. Gray diamonds indicate the values for conductance that we use in the resistor model, where we assume sharp transitions between conductance plateaus. **(b)**,**(c)** Non-local resistance results $\langle R_{nl} \rangle_{fc}$ as a function of gate voltage V_{g1} (controlling the number of open modes in the $I+$ QPC) for the dot with area 1.2 μm^2 **(b)** , and 2.9 μm^2 **(c)**. Gray lines show R_{nl} values from the resistor model, with the spin-flip resistance R_{sf} and polarization P as in the figure labels. The inset in **(b)** shows fluctuations of R_{nl} as a function of shape gate V_{p1} with all QPCs at a conductance of $2e^2/h$.

inset of Fig. 4.2b shows such fluctuations in R_{nl} as a function of the voltage on V_{p1}, which causes a small shape distortion of the dot. We discuss results as $\langle R_{nl} \rangle$ when presenting the average of 200 independent R_{nl} fluctuations, from sweeping with two different shape-distorting gates. Cross talk effects between gates were carefully mapped out and compensated for keeping the QPCs at their desired set points [12].

A second effect which, besides spin accumulation, may result in strong R_{nl} values is electron focusing [11]. Our sample was mounted with its plane at 0.73° with respect to the direction of the total magnetic field B. Consequently, there is a small perpendicular field $B_\perp$ and the associated electron cyclotron diameter equals the $I+$ to $V+$ contact distance (Fig. 4.1a) at $B = \pm 6$ T. We will mainly present results measured at $B = +8.5$ T, for which we found that focusing only weakly influences $\langle R_{nl} \rangle$ results. Further, we use that we can subtract a background contribution to $\langle R_{nl} \rangle$ from focusing (discussed below), and we present results where this is applied as $\langle R_{nl} \rangle_{fc}$. $B_\perp$ also breaks time-reversal symmetry (suppressing weak localization) when $|B| > 0.2$ T.

Figure 4.2b presents $\langle R_{nl} \rangle_{fc}$ as a function of the number of open modes in the $I+$ contact (tuned by V_{g1}), while the other QPCs are tuned as in Fig. 4.1b. On the left on this V_{g1} axis, the $I+$ QPC carries only one spin-up mode (conductance G_{I+} tuned to the e^2/h plateau, see also Fig. 4.2a). Here $\langle R_{nl} \rangle_{fc} \approx 1.8$ kΩ. Tuning V_{g1} to more positive values first adds an open spin-down mode to the $I+$ QPC (G_{I+} at $2e^2/h$), such that it is no longer spin selective and $\langle R_{nl} \rangle_{fc}$ drops here indeed to values near zero. Further opening of the $I+$ QPC tunes it to have two spin-up modes in parallel with one-spin down mode ($G_{I+} = 3e^2/h$). This causes again a situation with more spin-up than spin-down current in the $I+$ QPC, but less distinct than before and here $\langle R_{nl} \rangle_{fc}$ shows again a clear positive signal. Then, it drops to zero once more when the next spin-down mode is opened in the QPC. We obtain nominally the same results when the role of the current and voltage contacts is exchanged. Further, Fig. 4.2c shows that the large dot shows the same behavior, but with lower $\langle R_{nl} \rangle_{fc}$ values. This agrees with a lower value for R_{sf} for the large dot. From these measurement we can conclude that $\langle R_{nl} \rangle_{fc}$ is a signal that is proportional to the spin accumulation $\Delta\mu_{\uparrow\downarrow}$ in the dot.

The conductance of the $I+$ QPC, shown in Fig. 4.2a, displays multiple clear conductance plateaus that appear at the expected conductance values, although there are several bumps and dips in these plateaus. Especially at the e^2/h conductance plateau there is a pronounced resonance. However, a similar feature, a small peak followed by a dip for going to more positive gate voltages, can be seen

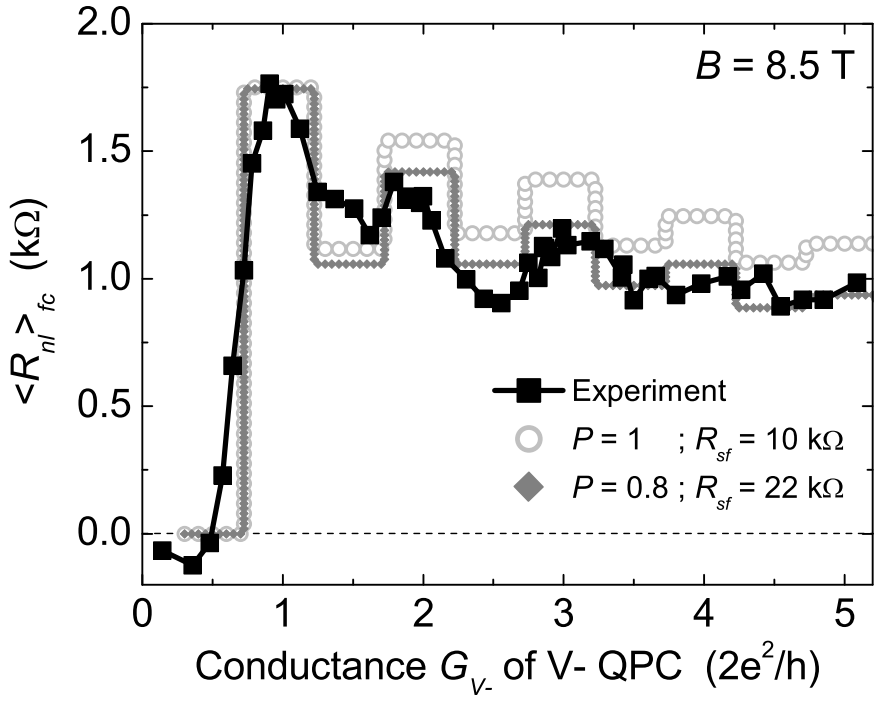

Figure 4.3: Averaged non-local resistance $\langle R_{nl}\rangle_{fc}$ as a function of the conductance G_{V-} of the V- QPC, for $A = 1.2\ \mu\text{m}^2$. Gray lines show R_{nl} values from the resistor model, with the spin-flip resistance R_{sf} and polarization P as labeled.

at the $2e^2/h$ plateau. In zero magnetic field also similar features appear for the first three conductance plateaus (not shown). Because the conductance plateaus do appear around the expected values, and the resonant feature appears in the same way for different plateaus, we think that the opening-up of subbands is not influenced significantly and our analysis as presented above is correct.

Figure 4.3 shows results from a similar experiment on the small dot (but also here the large dot showed the same behavior). Now $\langle R_{nl}\rangle_{fc}$ is measured as a function of the number of open modes in the $V-$ QPC (tuned by V_{g3}), while all other QPCs are again tuned as in Fig. 4.1b. Here we observe a signal close to zero when the $V-$ QPC carries only one spin-up mode ($G_{V-} = e^2/h$) since it then probes the same chemical potential as the $V+$ QPC. Opening it to $G_{V-} = 2e^2/h$ immediately results in a strong signal. Further opening this QPC then causes the signal to go up and down, qualitatively in reasonable agreement with the resistor model that assumes perfect polarization ($P = 1$) of each spin-selective mode in a QPC (see theory traces in Fig. 4.3, these go up and down in a step-like manner since we assume sharp transitions between conductance plateaus).

However, with quantitative agreement at $G_{V-} = 2e^2/h$ (for $R_{sf} = 10$ kΩ), this model with $P = 1$ shows an average slope down with increasing G_{V-} that is too weak. Instead, we find that the resistor model can show quantitative agreement over the full G_{V-} range (and with the results in Fig. 4.2) when we account for imperfect spin polarization of QPCs.

We model imperfect polarization in the resistor model as follows. We assume it only plays a role for QPCs set to a conductance of Ne^2/h, with N an odd integer (because the energy spacing between pairs of Zeeman-split subbands is large [8]). Spin-selective transport is then only due to the highest pair of subbands that contributes to transport, and *we define the polarization P only with respect to this pair*. This pair of subbands is then modeled as a resistor $R_\uparrow = 2R_K/(1+P)$ to the spin-up population in the dot, and a resistor $R_\downarrow = 2R_K/(1-P)$ to the spin-down population, which corresponds to $P = (R_\downarrow - R_\uparrow)/(R_\downarrow + R_\uparrow)$. This provides a simple model for R_{nl} with only R_{sf} and P as fitting parameters if we assume that all spin-selective QPCs and QPC settings can be modeled with a single P value. We find then a good fit to all the data in Figs. 4.2 and 4.3 for $P = 0.8 \pm 0.1$, with $R_{sf} = 22 \pm 3$ kΩ for the small dot and $R_{sf} = 7.5 \pm 1$ kΩ for the large dot. In Fig. 4.2b at $G_{I+} = 3e^2/h$, the experimental results are higher than the plotted model values. However, this turns into the opposite situation when using results obtained with the current and voltage QPCs exchanged. This indicates that P does not have exactly the same value for all QPCs and QPC settings. There is, however, always agreement with the model when accounting for the error bars of P and R_{sf}.

The values of R_{sf} correspond to $\tau_{sf} = 295 \pm 40$ ps for the small dot and $\tau_{sf} = 245 \pm 35$ ps for the large dot. In our type of system spin relaxation in the dot is probably dominated by Rashba and Dresselhaus spin-orbit coupling. How this mechanism results in a certain value for τ_{sf} then depends on the ballistic scattering rate at the edge of the dot. We performed numerical simulations of this mechanism, which yield that relaxation times indeed depend on the size of the dot, with typical values near 300 ps [5]. In our experiment, however, the error bars for τ_{sf} are too large for studying this dependence on the shape of our dots, but our method is suited exploring this topic in future work.

Figure 4.4 shows how focusing affects $\langle R_{nl} \rangle$ and $\langle R_{nl} \rangle_{fc}$. For QPCs tuned as in Fig. 4.1b the signal from spin accumulation drops to zero if either the $I+$ or the $V+$ QPC is tuned from e^2/h to $2e^2/h$ (no longer spin selective). However, when sweeping B we also measure large positive and negative $\langle R_{nl} \rangle$ values when the $I+$ QPC, the $V+$ QPC or both are at $2e^2/h$. For these three settings we

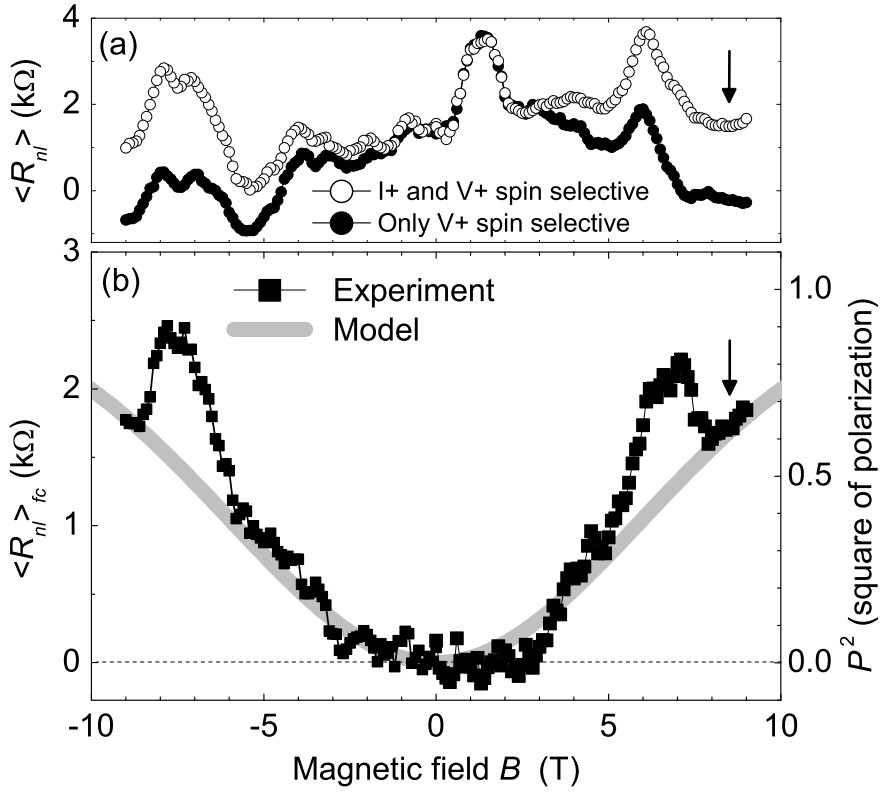

Figure 4.4: **(a)** Averaged non-local resistance $\langle R_{nl}\rangle$ as a function of B, for $I+$ and $V+$ at the e^2/h spin-polarized conductance plateau (open symbols), and for $I+$ at $2e^2/h$ (not spin selective) and only $V+$ at e^2/h (closed symbols). The $I-$ and $V-$ QPCs are at $2e^2/h$, $A = 1.2\ \mu\text{m}^2$. The difference in $\langle R_{nl}\rangle$ for the traces in (a) defines the focussing corrected non-local resistance $\langle R_{nl}\rangle_{fc}$, shown in **(b)**. The gray line in **(b)** is a fit of the model where the polarization P of QPCs (right axis) increases with Zeeman-splitting (see text). Arrows indicate B that was applied for measuring the data of Figs. 4.2, 4.3.

observed $\langle R_{nl}\rangle$ traces that are nominally the same (black symbols in Fig. 4.4a). The peaked structure is due to electron focusing effects [7, 11]. Only the peak at +6 T corresponds to direct focusing from the $I+$ into the $V+$ contact without an intermediate scatter event on the edge of the dot (it has the right B value and other peaks move to other B values when comparing the small and the large dot). Note, however, that all $\langle R_{nl}\rangle$ values are significantly higher when both the $I+$ and $V+$ QPC are tuned to be spin selective (open symbols in Fig. 4.4a). This difference between the open and black symbols defines the quantity $\langle R_{nl}\rangle_{fc}$ (Fig. 4.4b) and provides a signal that is mainly due to spin. This $\langle R_{nl}\rangle_{fc}$ data also

shows a peaked structure where $\langle R_{nl} \rangle$ shows strong focusing signals. This agrees with enhancement of electron focusing signals between spin-selective QPCs [7].

For interpreting $\langle R_{nl} \rangle_{fc}$ as a measure for spin accumulation, the experiment must be performed in a regime with many chaotic scatter events inside the dot during the electron dwell time. This is clearly not the case at the focusing peaks in Fig. 4.4b (at -7.5 T and $+6$ T). We therefore studied spin accumulation at $+8.5$ T where focusing from the $I+$ QPC scatters on the edge of the dot just before the $V+$ contact and where the signatures of focusing in $\langle R_{nl} \rangle$ are small. The agreement between the results of both Figs. 4.2 and 4.3, for both the small and large dot, and the resistor model supports the conclusion that these results were obtained in a chaotic regime.

As a final point we discuss that the degree of polarization $P = 0.8$ is in agreement with independently determined QPC properties. Steps between conductance plateaus are broadened by thermal smearing (a very weak contribution for our QPCs at 100 mK) and due to tunneling and reflection when the Fermi level E_F is close to the top of the QPC potential barrier for the mode that is opening. It is mainly this latter effect that causes $P < 1$ in our experiments. The role of tunneling and reflection in QPC transport is described with an energy dependent transmission $T(\epsilon)$ that steps from 0 to 1 when a QPC mode is opened. We study the effect of this on P by assuming that E_F is located exactly between the bottoms of a pair of Zeeman split subbands. For these two subbands we use $T(\epsilon)_{\uparrow(\downarrow)} = (\mathrm{erf}(\alpha(\epsilon - E_F - (+)E_Z/2)) + 1)/2$, a phenomenological description that agrees with studies of our QPCs [8]. Here $E_Z = g\mu_B B$ is the Zeeman splitting (for g-factor g and Bohr magneton μ_B) and α a parameter that sets the width of the step in $T(\epsilon)$. For $eV_{bias} < k_B T_{eff}$, the contributions of these two subbands to the QPC conductance are then $G_{\uparrow(\downarrow)} = (e^2/h) \int \mathrm{d}\epsilon \, (-\mathrm{d}f/\mathrm{d}\epsilon) \, T(\epsilon)_{\uparrow(\downarrow)}$, where f the Fermi function. With $P = (G_\uparrow - G_\downarrow)/(G_\uparrow + G_\downarrow)$ we now calculate how P increases with B due to an increasing Zeeman splitting. In the resistor model the dependence of R_{nl} on P is close to $R_{nl} \propto P^2$. We therefore plot P^2 in Fig. 4.4b (gray line, with scaling of the right axis such that it overlaps with the experimental results) for parameters that give the consistent result $P = 0.8$ at $B = 8.5$ T. For this we use $|g| = 0.44$ (as for bulk GaAs) and an α value that is derived from a full-width-half-max of 0.2 meV for the peak in $\mathrm{d}T(\epsilon)/\mathrm{d}\epsilon$. The latter parameter agrees with the values 0.20 to 0.35 meV that we found when characterizing this for our QPCs [8]. Notably, we cannot calculate such a consistent result if we assume that the many-body effects that we observed in our QPCs [8] enhance the Zeeman splitting (showing for example $|g| \approx 1.1$). This indicates that these

effects do not play a role for spin injection and detection with QPCs, as was also found in Ref. [7].

4.5 Signatures of spin transport in the 2-terminal conductance

We investigate signatures of spin accumulation and spin relaxation in the two-terminal conductance of our QD, as an alternative to the non-local measurement geometry [6, 13]. This method should, in principle, make the experiment less complex since only two QPCs have to be set simultaneously, instead of four in the non-local experiment. In practice this method is complicated by the additional requirement that one needs broad, flat (spin-selective) conductance plateaus to reliably determine the signatures of spin accumulation in the series conductance of the dot [6, 13].

The system is tuned to the following setting. The QPC to the $I+$ reservoir is tuned to have a single open mode, which is only available for spin-up electrons, while the QPC to the $I-$ reservoir is tuned to carry one mode for spin-up and one mode for spin-down. Initially all other QPCs are pinched-off. With these settings the series conductance of the QPCs is $\frac{1}{4}(2e^2/h)$ if there is no spin relaxation and $\frac{1}{3}(2e^2/h)$ if there is strong spin relaxation. The measured value of conductance will typically lie in between these two limits and can be used to extract the spin relaxation time [13]. Further we can measure the 2-terminal series conductance while we open a third QPC to a large (floating) electron reservoir. This provides an additional relaxation mechanism for loss of spin accumulation, and will allow us to not only extract a value for the spin flip time, but also to identify contributions to spin relaxation from coupling the dot to reservoirs, and the degree of polarization for spin-selective transport in the contacts.

Here we will present some preliminary data on this type of experiment. We have corrected for quantum fluctuations in G due to electron interference inside the dot by averaging over 200 independent fluctuations. The measurements were done at $B = 9$ T, but we have not studied the effects of focussing carefully.

Fig. 4.5a presents $\langle G \rangle$ as a function of the number of open modes in the $I+$ contact (tuned by V_{g1}). The $I-$ contact was tuned to have one spin-up and one spin-down mode. When the $I+$ QPC is tuned to a spin degenerate plateau we measure the same two-terminal conductance for each of the three different dot areas. We do expect to measure a difference in conductance when the $I+$ QPC

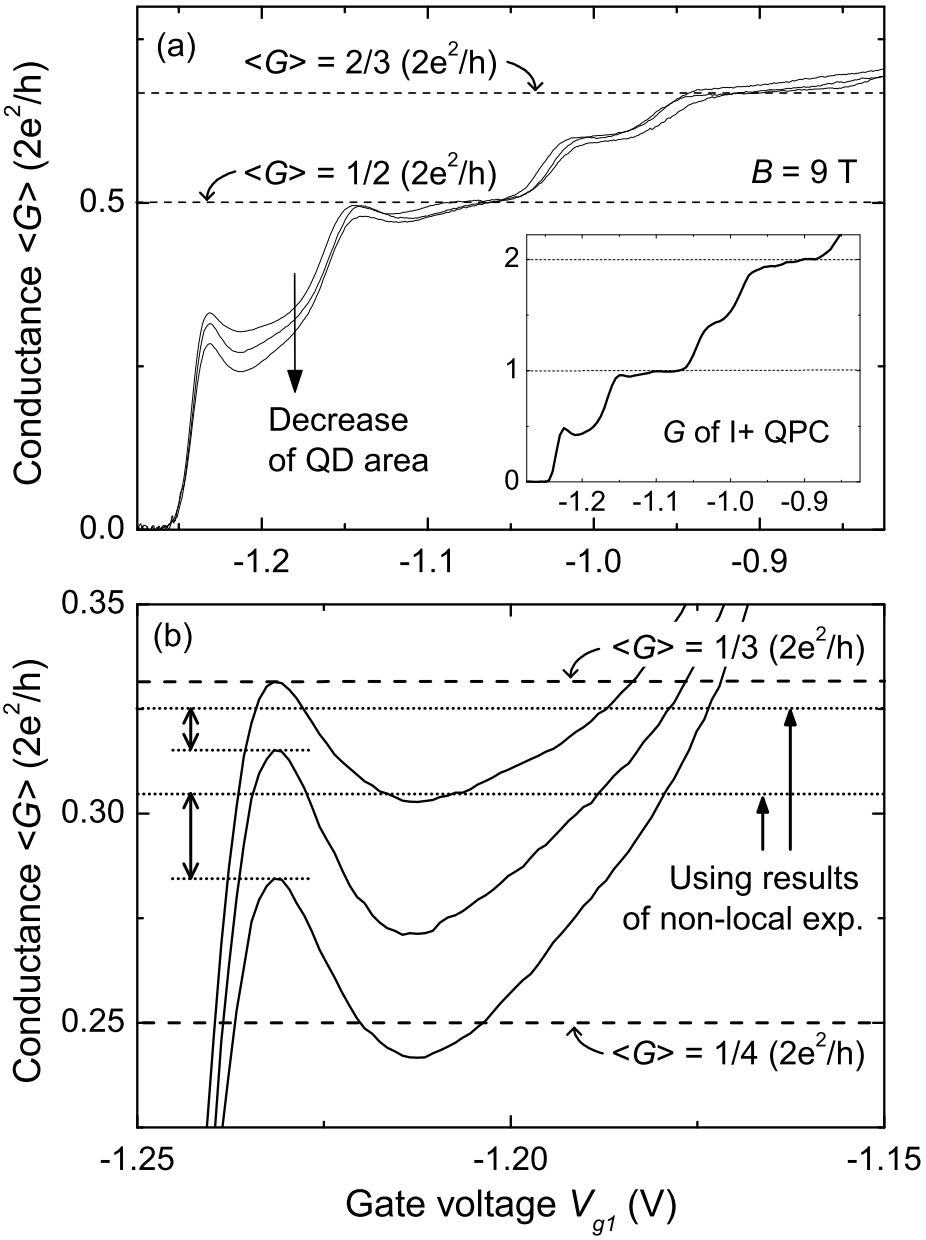

Figure 4.5: **(a)** Average two-terminal conductance $\langle G \rangle$ as a function of gate voltage V_{g1} (controlling the number of open modes in the $I+$ QPC), for the dot with area 1.2 μm^2, 2.9 μm^2, and 10000 μm^2 measured at $B = 9$ T. The $I-$ QPC is set to $2e^2/h$. The dashed lines indicate conductance values where both QPCs are set to spin degenerate plateaus. **(b)** Enlarged view of the data in **(a)** at the gate voltage range where the conductance of the $I+$ QPC is around e^2/h. Dashed lines indicate the two limits for spin relaxation. Dotted lines and arrows on the left indicate the difference between current experiment and expected values using results of the non-local experiment.

is at a spin selective plateau. Indeed, when the $I+$ QPC is tuned to the e^2/h plateau we observe a clear difference between the three traces, we find a smaller value for the conductance for a decrease in dot area. When the $I+$ QPC is tuned to $3e^2/h$ we do not observe any significant difference.

We now focus on the situation where the $I+$ is tuned to e^2/h. We then expect to measure plateau heights that are in between the two limits of $\frac{1}{4}(2e^2/h)$ and $\frac{1}{3}(2e^2/h)$. However, as shown in Fig. 4.5a, the conductance plateau is far from a broad, flat plateau. This is a result of the resonance in the e^2/h plateau of the $I+$ QPC shown in the inset of Fig. 4.5a (and in Fig. 4.2a for B = 8.5 T). The question is therefore what value of the conductance we should use as plateau height. We choose to use the value of the conductance at the small peak near V_{g1} = -1.23 V, for two reasons. Firstly, in the measured conductance of the QPC to the $I+$ reservoir, the conductance value at the peak is exactly equal to $0.5(2e^2/h)$. Secondly, at the peak in the series conductance for the largest dot with area $\sim$ 10000 μm^2, the value of the conductance is, as expected, equal to $\frac{1}{3}(2e^2/h)$, the limit where all spins can relax. The reason why we did not choose any other combination of QPCs for this experiment is that none of the other QPCs had a broad, flat e^2/h plateau, or, in other words, a plateau that would allow easier determining of the exact value of the conductance at the plateau.

Earlier in this chapter we have measured the relaxation time for the two smallest dots and, using the resistor model, we can use these times to calculate the two-terminal conductance that we expect to measure. Here we have used τ_{sf} = 295 ps for a dot of 1.2 μm^2 and τ_{sf} = 245 ps for a dot of 2.9 μm^2. We also used polarization $P = 0.8$ for the contacts. If we compare these calculated values to the values we measure here, we find that we observe here in both cases a lower value for conductance (also if we include error bars of τ_{sf} and P). This could mean we measure much longer relaxation times in this experiment, however we believe that these measured conductances are not reflecting properties of the spin accumulation in the dot, but are determined by the same phenomenon that causes the resonant-like feature to appear. Therefore we decided not to continue with this type of experiment on this particular device.

4.6 Conclusions

In conclusion, we have observed spin accumulation in a large open quantum dot in a non-local measurement and extracted values for τ_{sf} and P. We find values of $\tau_{sf} = 295 \pm 40$ ps for a dot of 1.2 μm^2 and $\tau_{sf} = 245 \pm 35$ ps for a dot

of 2.9 μm^2. These values are much lower than reported values from studies on large high-mobility 2DEG areas. This is probably due to enhanced dephasing by spin-orbit effects which results from frequent scattering on the edge of the dot. We can reproduce this effect qualitatively with Monte-Carlo simulations, presented in Chapter 5 of this thesis. The values of $P = 0.8 \pm 0.1$ that we find, are consistent with the short length ($\sim$100 nm) of our QPCs. The short length causes a broad energy window where the onset of the transmission of each QPC mode builds up, such that two Zeeman split modes still overlap considerably in a field of 9 T. Notably, our data set is consistent with a Zeeman energy that is simply $g\mu_B B$ with $g = 0.44$, indicating that many-body effects in QPC that can enhance Zeeman splittings do not play a role in our type of experiment. We have been made aware of related results obtained by S. M. Frolov *et al.* [14] with a narrow Hall bar.

We have presented a method for extracting spin relaxation times from the two-terminal conductance of a quantum dot, inspired by experimental results of Zumbühl *et al.* [13] and theory paper by Beenakker [6]. We have studied this two-terminal conductance for dots with three different areas, but unfortunately the spin-resolved plateau at e^2/h for one of the contacts was disturbed by a pronounced resonance. Therefore we could not extract reliable numbers for spin relaxation time or polarization using this method.

We thank A. I. Lerescu, B. H. J. Wolfs and D. M. Zumbühl for useful discussions, and the Dutch Foundation for Fundamental Research on Matter (FOM) and the Netherlands Organization for Scientific Research (NWO) for funding.

References

[1] For a recent review see D. D. Awschalom and M. E. Flatté, Nat. Phys. **3**, 153 (2007).

[2] F. J. Jedema *et al.*, Nature **410**, 345 (2001).

[3] X. Lou *et al.*, Nat. Phys. **3**, 197 (2007).

[4] N. Tombros *et al.*, Nature **448**, 571 (2007).

[5] E. J. Koop *et al.*, arXiv:0804.2968.

[6] C. W. J. Beenakker, Phys. Rev. B **73**, 201304(R) (2006).

[7] R. M. Potok *et al.*, Phys. Rev. Lett. **89**, 266602 (2002).

[8] E. J. Koop *et al.*, J. Supercond. Nov. Magn. **20**, 433 (2007).

[9] M. Johnson, Phys. Rev. Lett. **70**, 2142 (1993).

[10] Y. Alhassid, Rev. Mod. Phys. **72**, 895 (2000).

[11] A. I. Lerescu *et al.*, arXiv:0705.3179.

[12] D. R. Stewart, PhD thesis, Stanford University (1999).

[13] D. M. Zumbühl *et al.*, 2001 March Meeting Bulletin of the American Physical Society (unpublished), Abstract C25.006 (2001).

[14] S. M. Frolov *et al.* arXiv:0801.4021 (2008).

Chapter 5

Confinement-enhanced spin relaxation for electron ensembles in large quantum dots

We present a numerical study of spin relaxation in a semiclassical electron ensemble in a large ballistic quantum dot. The dot is defined in a GaAs/AlGaAs heterojunction system with a two-dimensional electron gas, and relaxation occurs due to Dresselhaus and Rashba spin orbit interaction. We find that confinement in a micronscale dot can result in strongly enhanced relaxation with respect to a free two-dimensional electron ensemble, contrary to the established result that strong confinement or frequent momentum scattering reduces relaxation. This effect occurs when the size of the system is on the order of the spin precession length, but smaller than the mean free path.

This chapter is based on Ref. 4 on p. 131.

5.1 Introduction

Due to spin-orbit interaction (SOI), the state of electron spins is influenced by electron transport in electronic devices. This has been recognized as a source for dephasing and relaxation for spins [1, 2], as well as a means for controlled spin manipulation [3] in research that aims at developing spintronic devices [2, 4, 5]. In this article we present a numerical study of spin relaxation in an electron ensemble that is scattering inside a micronscale device structure. We are interested in the case where devices are made of clean semiconductor heterostructures and studied at low temperatures. For our studies we assume realistic material parameters for a system with a two-dimensional electron gas (2DEG) at a GaAs/AlGaAs heterojunction. For a free 2DEG in these materials, a well established result is that the average spin orientation of an ensemble decays due to precession in spin-orbit fields. For moderate electron mobilities, this so-called D'yakonov-Perel' (DP) mechanism for spin relaxation [6, 7] has the property that the spin relaxation time T_1 increases when the mobility (and thereby the time scale τ_s for elastic momentum scattering) decreases, as $T_1 \propto \tau_s^{-1}$.

A similar trend is observed when the degree of electron confinement in a device structure is increased. Stronger confinement gives more frequent scattering on the boundaries of the system, and hence reduces the relaxation. This has been recognized in the increase of T_1 on the transition from 2D to 1D systems [8]. In the limit quantum confinement in extremely small devices (much smaller systems than we consider for the present study), relaxation and dephasing due to SOI is then strongly reduced, and other relaxation mechanisms can become dominant. This applies for example to spin dephasing in few-electron quantum dots, which can be mainly due to interaction with nuclear spins [10, 11, 9]. Although more frequent scattering due to stronger confinement thus seems similar to reducing the mobility in bulk materials, the results that we present here show that frequent scattering due to confinement can also result in the opposite, namely confinement-enhanced relaxation.

The key result of the present study is well presented by the traces for spin relaxation time T_1 as a function of the size L of a square quantum dot in Fig. 5.1a. The trace for the case that an external magnetic field $B_{ext} = 0$ T and 2DEG mobility $\mu = 100$ m^2/Vs, shows that T_1 is constant for $L > 10$ μm. Here L is so large that the electron ensemble behaves as in a free 2DEG. When decreasing L below 10 μm, T_1 increases because spin relaxation in suppressed by more frequent scattering on the edge of the system. The trace for $B_{ext} = 10$ T and

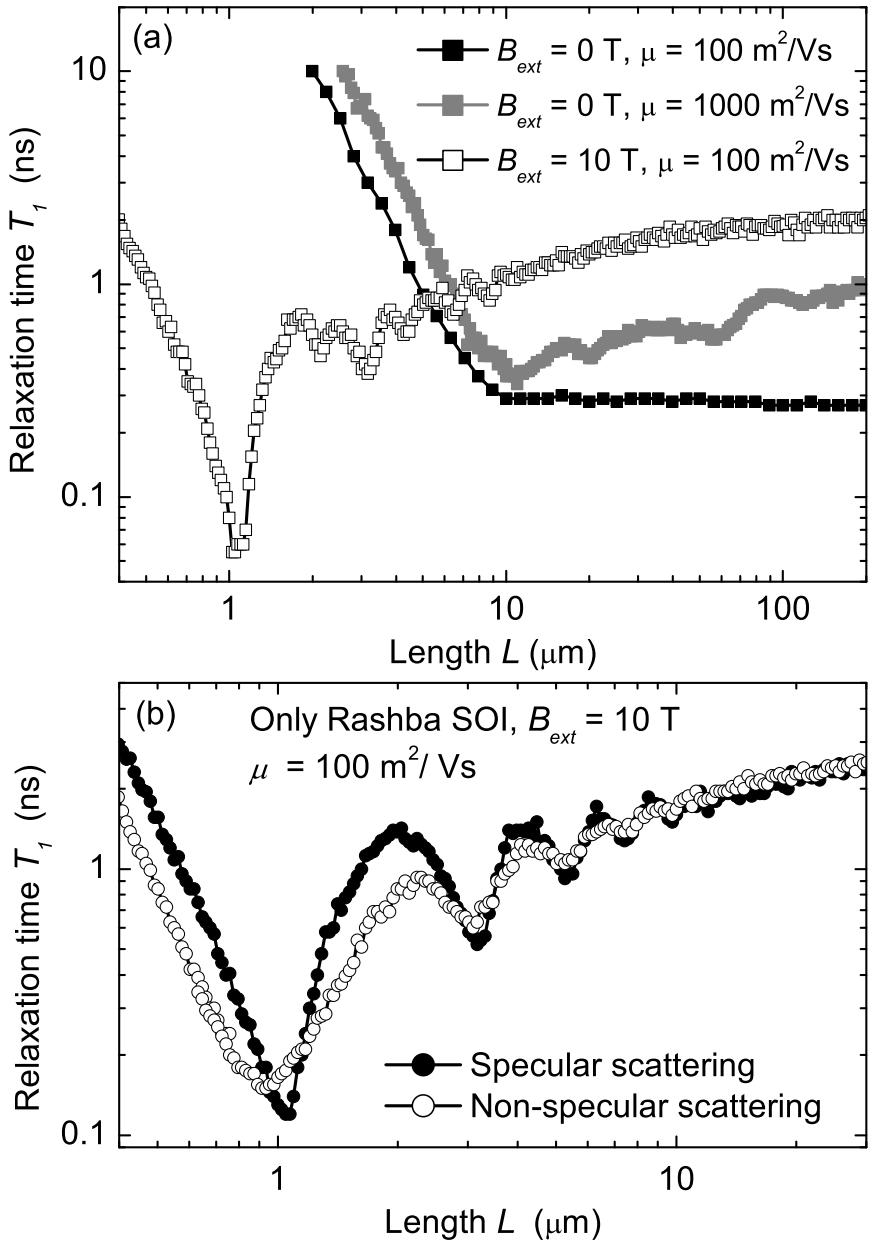

Figure 5.1: **(a)** Spin ensemble relaxation in a quantum dot system of size L. The relaxation time T_1 is calculated as a function the size L for a square system. For mobility $\mu = 100$ m^2/Vs we plot T_1 for zero external magnetic field (filled black symbols) and for $B_{ext} = 10$ T (open symbols). The gray symbols show T_1 for zero external magnetic field and $\mu = 1000$ m^2/Vs. **(b)** Relaxation time as a function of L for a system with only Rashba SOI. Calculations for specular and non-specular reflections give qualitatively the same results, but the magnitude of the resonant structure in the traces of T_1 as a function of L is larger in the case of specular reflections.

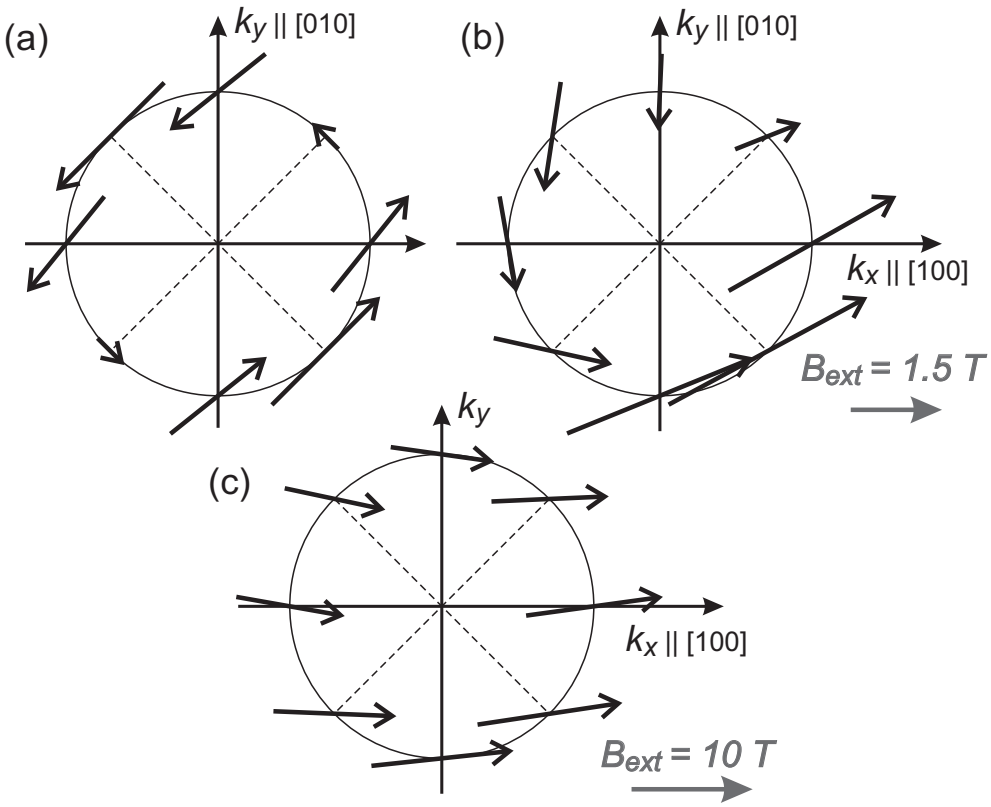

Figure 5.2: **(a)** Schematic representation of the direction and magnitude of the SOI fields. Since we assume all electrons move with the same magnitude for k-vector k_F, we can represent the motion of electrons in all directions as a circle in the (k_x,k_y)-plane. The arrows that are sketched at certain points on this Fermi circle, represent the strength and direction of the SO field $\mathbf{B}_{SO}$ for that k-vector. **(b)** Magnitude and direction of the total effective magnetic field when an external field $B_{ext} = 1.5$ T is applied along the [100]-direction. **(c)** Idem for an external field $B_{ext} = 10$ T. In this plot the length of all arrows has been scaled down by a factor 5 as compared to **(a)** and **(b)**.

2DEG mobility $\mu = 100$ m^2/Vs (typical parameters for research on spin effects in micronscale quantum dots [13] and wires [14]), however, shows radically different behavior. Now T_1 first slowly decreases when decreasing L from the 2D regime (very large L), and shows a pronounced dip for $L \approx 1$ μm. Confinement now strongly enhances relaxation, instead of the more familiar result that confinement reduces relaxation. Moreover, in the range with 1 μm $< L <$ 10 μm, T_1 has a highly structured dependence on L. Only when decreasing L below $L \approx 1$ μm, T_1 shows again a strong and monotonic increase as for the confinement-suppressed

relaxation in $B_{ext} = 0$ T.

We obtain these results with a numerical Monte Carlo approach. This has the advantage that we can study precessional relaxation for realistic conditions, where the total magnetic field is the sum of several spin-orbit contributions and an external field. In reality, samples typically have both Rashba and Dresselhaus SOI that are comparable in magnitude [15], and in experiments one often needs to apply strong external magnetic fields for realizing spin transport in non-magnetic semiconductors [16, 13, 14]. The combination of spin-orbit contributions and external magnetic fields may strongly influence the relaxation behavior in these type of devices [17, 18]. Earlier studies of these relaxation phenomena were often restricted to more tractable cases, as for example with only Rashba SOI [19] (no Dresselhaus SOI), and no external fields. Below, we will summarize our numerical method, and then focus on studying the dependence of T_1 on the degree of confinement in micronscale quantum dots. We will also show that in regimes and for parameters that were studied before, our simulations give the conventional results.

5.2 Spin-orbit coupling

We use a description where spin-orbit (SO) coupling acts as a k-vector dependent effective magnetic field on the electron spins. In a 2DEG it is dominated by two sources [15]. The first arises due to the inversion asymmetry in the potential profile of the heterostructure and results in an effective Rashba magnetic field $\mathbf{B}_R$ [20]. The second effect arises due to the lack of inversion symmetry in the GaAs crystal lattice, which is of the zinc-blende type, and yields for a 2DEG the linear and cubic Dresselhaus fields $\mathbf{B}_{D1}$ and $\mathbf{B}_{D3}$ [21, 1]. The effective SO field $\mathbf{B}_{SO}$ in a 2DEG can thus be described as the vector sum of these three components, given by [15, 1]

$$\mathbf{B}_R = C_R(\hat{\mathbf{x}}k_y - \hat{\mathbf{y}}k_x), \tag{5.1}$$

$$\mathbf{B}_{D1} = C_{D1}(-\hat{\mathbf{x}}k_x + \hat{\mathbf{y}}k_y), \tag{5.2}$$

$$\mathbf{B}_{D3} = C_{D3}(\hat{\mathbf{x}}k_x k_y^2 - \hat{\mathbf{y}}k_y k_x^2), \tag{5.3}$$

where C_R, C_{D1} and C_{D3} are the coupling parameters, $\hat{\mathbf{x}}$ is the unit vector in the [100]-direction, and $\hat{\mathbf{y}}$ in the [010]-direction. Our results are calculated using the SO parameters that were reported by Miller *et al.* [15], $C_R = -1.96 \cdot 10^{-8}$ Tm, $C_{D1} = -1.57 \cdot 10^{-8}$ Tm, and $C_{D3} = -1.18 \cdot 10^{-24}$ Tm^3.

The total SO field is then anisotropic in momentum space as is shown in Fig. 5.2a. Each time an electron scatters and its direction of motion changes it will precess around a different axis set by $\mathbf{B}_{SO}$. For our set of SO parameters these fields $\mathbf{B}_{SO}$ lie more or less parallel to the [110]-direction for almost all k-directions. Figures 5.2b,c show the effect of adding an external magnetic field $\mathbf{B}_{ext}$, which is independent of momentum direction. We consider here the situation that $\mathbf{B}_{ext} \parallel \hat{\mathbf{x}}$. The total effective magnetic field $\mathbf{B}_{tot}$ is then the vector sum of the SO fields and the external magnetic field. When the magnitude B_{ext} of $\mathbf{B}_{ext}$ is comparable to that of the SO fields, as shown in Fig. 5.2b for $B_{ext} = 1.5$ T, the total effective magnetic fields are no longer mainly parallel to the [110]-direction and there is larger spread in the directions of the precession axes $\mathbf{B}_{tot}$. Figure 5.2c shows that for very large external magnetic fields, shown here for $B_{ext} = 10$ T, the total effective magnetic fields $\mathbf{B}_{tot}$ align with $\mathbf{B}_{ext}$ along the [100]-direction. This again reduces the spread in the direction of the precession axes $\mathbf{B}_{tot}$.

5.3 Method

In our numerical approach we use a classical description of the electron motion, and a quantum mechanical description of the dynamics of the electron spin. We thus assume that electrons have at all times a well-defined k-vector, and electrons move along classical trajectories with specular scattering on the boundaries of the system, and scattering in a random direction on static potential fluctuations due to impurities. Electrons never escape from the system. Although in micronscale quantum dots the motion of electrons is confined, the mean level spacing is much smaller than temperature, $\Delta_m \ll k_B T$, and this allows for this semiclassical description. Further, we consider the case that all the electrons that carry the spin orientation are near the Fermi level. Thus, we assume that all electron always move with the Fermi velocity (k-vectors with magnitude k_F), independent of the momentum direction. This is a valid approximation for $k_B T, \Delta E_{Z,SO} \ll E_F$ (with respect to the bottom of the conduction band), where $\Delta E_{Z,SO}$ is the Zeeman splitting due to the SO field alone. Obviously, the validity of our approach breaks down in the limit of very small dots, where electrons are highly localized due to quantum confinement. In practice, this occurs for quantum dots with size L below ~ 400 nm, but our results for this regime always show a very strong suppression of precessional relaxation, which is the semiclassical equivalent for suppressed relaxation for quantum confined electrons [10, 11].

Our simulation then works as follows. It starts at $t = 0$ with each electron

at a random position in a square shaped dot of size L, and with a k-vector in a random direction. We always consider the case that at $t = 0$ the spin state is prepared in the positive $\hat{\mathbf{x}}$-direction. For each electron, we follow its state in time, and its momentum direction will change at each scattering event. During each ballistic trajectory between scatter events, the electron has a well-defined k-vector, and we calculate the effective spin-orbit field during this trajectory with Eqs. 5.1-5.3. The precession angle α_i during a single trajectory is then given by

$$\alpha_i = \frac{g\mu_B \mathbf{B}_{tot}}{\hbar} \cdot t_i, \tag{5.4}$$

where t_i is the traveling time $t_i = l_i/|v|$. The rotation operator working on the initial spin state to determine the new spin state is a function of α_i and of the unit vector $\mathbf{U}_i = \mathbf{B}_{tot}/|\mathbf{B}_{tot}| = (u_{x_i}, u_{y_i}, u_{z_i})$ around which the spin is precessing and is given for a single trajectory by [12]

$$R_i = \begin{pmatrix} \cos(\frac{\alpha_i}{2}) - iu_{z_i}\sin(\frac{\alpha_i}{2}) & (-iu_{x_i} - u_{y_i})\sin(\frac{\alpha_i}{2}) \\ (-iu_{x_i} + u_{y_i})\sin(\frac{\alpha_i}{2}) & \cos(\frac{\alpha_i}{2}) + iu_{z_i}\sin(\frac{\alpha_i}{2}) \end{pmatrix}. \tag{5.5}$$

After each scattering event the electron will precess around a new effective magnetic field, and we follow the quantum mechanical spin evolution in the total effective magnetic field during each ballistic trajectory. The rotation operator along the entire trajectory can be represented as the product of the individual operators along the n straight sections of the trajectory

$$R = R_n \cdots R_2 R_1. \tag{5.6}$$

We thus find the spin state of each electron as a function of time.

The spin evolution is calculated for an ensemble of (at least) 10^3 electrons. This mimics the averaging over many electrons in an electron transport experiment, since large quantum dots behave in practice as a chaotic ballistic cavity [13]. In our model the magnitude of the average spin orientation for the ensemble decays to zero because each electron has its own scattering trajectory, such that the relative difference between the precessional dynamics of individual electrons increases in time. We will always refer to this as spin relaxation for the ensemble (with decay time T_1), rather than dephasing, because we concentrate on the loss of average spin orientation in the direction of the external magnetic field that we apply. Note however, that in our description each individual electron always keeps precessing coherently in its particular spin-orbit field. Consequently, the underlying mechanism is equivalent to that of spin dephasing for an ensemble,

and in particular for our simulations with $B_{ext} = 0$ T one could argue that the loss of spin orientation should be named dephasing.

The average spin orientation is calculated for the whole ensemble as a function of time, independent of the position of the individual electrons. In this study we concentrate on the average spin polarization $\langle S_x \rangle$ in the $\hat{\mathbf{x}}$-direction. We find in all cases that we consider here that the decay time for $\langle S_x \rangle$ equals that of $\langle S \rangle$, where $\langle S \rangle = \sqrt{\langle S_x \rangle^2 + \langle S_y \rangle^2 + \langle S_z \rangle^2}$, because no significant polarization develops in the $\hat{\mathbf{y}}$ or $\hat{\mathbf{z}}$-direction. The relaxation time T_1 is then defined as the time when $\langle S_x \rangle$ is reduced to $1/e$ of its initial value at $t = 0$. We used electron density $1.0 \cdot 10^{15}$ m^{-2} and mobility 100 m^2/Vs, unless stated otherwise. We neglect inelastic scattering mechanisms and electron-electron interactions.

The momentum direction for an electron changes after specular scattering on the boundary of the system. This process we will refer to as edge scattering and the typical length scale involved here is L, where the area of the quantum dot system is $A = L^2$. A second effect causing a change in momentum direction is scattering on static fluctuations in the potential due to impurities. Here, a scatter event changes the momentum into a random direction. We incorporate this into our modeling as follows. When an electron is moving ballistically through the system, the probability that it did *not* scatter due to impurities decreases as e^{-t/τ_s} (where τ_s is the average impurity scatter time) and this probability is reset to 1 after each impurity scatter event. We thus define the mean free path $L_{mfp} = |v_F|\tau_s$ as the length in between scatter events when only considering impurity scattering.

Another important length scale in our system is the so-called precession length $\langle L_{pr} \rangle$. This is defined as the length of the trajectory where a spin has precessed over an angle π. In our system this length scale is k-vector dependent due to the anisotropy of SO fields. Therefore, we define $\langle L_{pr} \rangle$ as the length of the trajectory for precession over an angle π around the average total effective magnetic field $\langle |\mathbf{B}_{tot}| \rangle$, where we average over all k-directions to account for the anisotropy for the SO contribution to the total field.

Evaluating the relative size of these three length scales, L, L_{mfp}, and $\langle L_{pr} \rangle$, for a specific system helps to understand many properties of the relaxation time. Before discussing results for quantum dots, it is instructive to discuss two regimes that occur for a free 2DEG (L very large). For such systems, Fig. 5.3 presents traces with T_1 as a function of L_{mfp}. We first focus on the case with $B_{ext} = 0$ T, for which $\langle L_{pr} \rangle = 8$ μm. If $L_{mfp} \ll \langle L_{pr} \rangle$, the precession angle in between scatter events is small. Consequently, the spin state only slowly diffuses away from

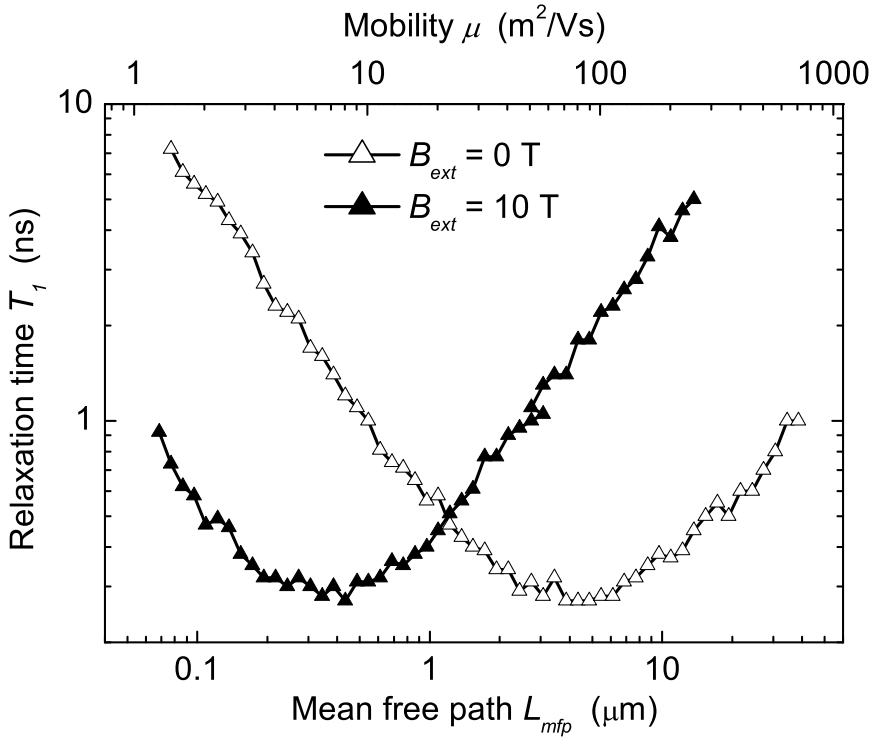

Figure 5.3: Relaxation time T_1 as a function of the mean free path L_{mfp} for a free 2DEG. The top axis shows the corresponding value for mobility μ. Calculations for zero external field and $B_{ext} = 10$ T.

its initial direction in a random walk-like process. Here scattering suppresses relaxation. This regime is known as the motional narrowing regime [22], and the relaxation time is inversely proportional to the scatter time, $T_1 \propto \tau_s^{-1}$. When $L_{mfp} \gg \langle L_{pr} \rangle$, the spins will coherently precess over at least one full rotation between scatter events. Without momentum scattering, the ensemble shows spin relaxation since each electrons precesses in a different field, but each electron will maintain its component in the direction of its precession axis. Only when a scatter event occurs this coherent precession is disturbed, such that further relaxation for the ensemble can occur. In this regime $T_1 \propto \tau_s$. The crossover between these two regimes (where T_1 shows a minimum) occurs for $L_{mfp} \approx \langle L_{pr} \rangle$. Switching on an external magnetic field of 10 T for this system, reduces the length scale $\langle L_{pr} \rangle$ to 1.1 μm. For T_1 as a function of L_{mfp}, this only results in a shift of the entire curve, with the minimum now occurring at the new value where $L_{mfp} \approx \langle L_{pr} \rangle$. We conclude here that our calculations for Fig. 5.3 reproduce the conventional result [2].

5.4 Results

We now turn to discussing results for quantum dots, for which L can be smaller than $\langle L_{pr} \rangle$ and L_{mfp}. Figure 5.1a shows simulations of the relaxation time as a function of dot size L. We first discuss the result for zero external magnetic field (which gives $\langle L_{pr} \rangle = 8$ μm) and mobility $\mu = 100$ m^2/Vs (corresponding to $L_{mfp} = 5$ μm). For this system, a decrease of L in the regime with $L < \langle L_{pr} \rangle$ results in higher T_1 values. We will refer to this regime as the quasi-0D regime. Here frequent scattering suppresses precession, as for motional narrowing in the 2D regime. Here, we observe that $T_1 \propto L^{-2}$, a dependence on L that was also found for studies on the suppressed relaxation in long quasi-1D channels of width L [8, 23]. For $L > \langle L_{pr} \rangle$ we do not observe any change in T_1. This will be denoted as the 2D regime, for which $L \gg \langle L_{pr} \rangle, L_{mfp}$.

For $B_{ext} = 10$ T (and again $\mu = 100$ m^2/Vs) the behavior is dramatically different (also shown in Fig. 5.1a). When coming from the 2D regime, there is no longer simply an increase in T_1 when lowering L towards the regime where $L \ll \langle L_{pr} \rangle, L_{mfp}$. Instead, there is a regime, here for 0.6 μm $< L <$ 10 μm, where T_1 is strongly suppressed. Moreover, the decrease in T_1 when lowering L from 10 μm to 1 μm shows a structured pattern. For this value of the external magnetic field the precession length is reduced to $\langle L_{pr} \rangle = 1.1$ μm. The mean free path is still $L_{mfp} = 5$ μm, such that switching on a strong field opens up a regime with $\langle L_{pr} \rangle \lessapprox L < L_{mfp}$ in between the 2D and the quasi-0D regimes. Notably, switching on a strong magnetic field for a system in the 2D regime increases T_1 by about one order of magnitude. However, switching on a field for a system in the same material with $L \approx 1$ μm causes T_1 to go down more than 2 orders of magnitude. Now confinement enhances relaxation.

For $B_{ext} = 0$ T and $\mu = 100$ m^2/Vs we do not see a dependence of T_1 on L in the regime where $L > \langle L_{pr} \rangle$, because for that system $L_{mfp} \approx \langle L_{pr} \rangle$. However, also in zero external magnetic field we can open up a regime where $\langle L_{pr} \rangle \lessapprox L < L_{mfp}$ by choosing a higher value for mobility. This is demonstrated for $\mu = 1000$ m^2/Vs (which gives $L_{mfp} = 50$ μm) in Fig. 5.1a. Now for 7 μm $< L <$ 100 μm the relaxation time decreases when decreasing L, and again T_1 shows a structured pattern (*i.e.* the structure on this trace here is not noise from averaging over a finite ensemble).

The reduction in T_1 due to stronger confinement is thus a general effect and appears whenever $\langle L_{pr} \rangle \lessapprox L < L_{mfp}$. These are typical conditions for micronscale quantum dots when large external magnetic fields are applied. Notably, the values

that we obtain here for T_1 are very close to the values that we recently observed in spin accumulation experiments in micronscale quantum dots [13]. We found $T_1 \approx 300$ ps for a quantum dot with $L \approx 1.1$ μm and $B_{ext} = 8.5$ T. This indicates that our simulations generate realistic numbers.

We will now analyze the relaxation mechanism for this confinement-enhanced relaxation. To study why there is strong dip and structure in the dependence of T_1 on L, we choose a simplified model system where we only consider the Rashba SOI and an external magnetic field $B_{ext} = 10$ T. Both Dresselhaus SOI contributions have been set to zero. Using only Rashba has the advantage that the magnitude for the SO fields is identical for all k-vectors. The structure in T_1 appears more regular here (see Fig. 5.1b). This proves that the effects that we present here do not only occur for very particular SO parameters.

We have repeated this calculation where we programmed non-specular reflections on the walls of the quantum dot, such that after hitting a side of the quantum dot the electron is reflected with random angle back into the quantum dot (open symbols in Fig. 5.1b). The structure on T_1 still appears, which confirms that self-repeating patterns are not the origin of this effect. We observe, however, that the amplitude of the structure on T_1 is reduced for this setting. This is caused by an increased variation in the length of trajectories in between scatter events for non-specular reflections. We checked this by making histograms of the trajectory lengths for specular and non-specular reflections (not shown).

For both traces in Fig. 5.1b, we find that the minimums in T_1 appear at odd multiples of the average precession length $\langle L_{pr} \rangle$, and local maximums occur at even multiples of $\langle L_{pr} \rangle$. This means that for systems with a size equal to an odd multiple of $\langle L_{pr} \rangle$ the electrons scatter (on average) after precessing (again, on average) over an angle of exactly π (mod 2π) between scatter events, furthest away from their original state. This causes fast relaxation. For systems with a size equal to an even multiple of $\langle L_{pr} \rangle$, the electrons scatter on average after precessing 2π (mod 2π), so when they are back in their original state. Then relaxation is slower as compared to the local minimums. However, note that for these local maximums there is overall still a reduction of T_1 due to confinement as compared to free 2DEG: in this regime, more frequent scattering on the edge of the system always enhances relaxation. The character of the relaxation mechanism itself is thus similar to the regime with $\langle L_{pr} \rangle \ll L_{mfp}$ for 2D systems, where $T_1 \propto \tau_s$. The additional feature here is the structure on T_1 as a function of L, which signals that the overall relaxation mechanism is either somewhat resonantly enhanced or suppressed when the time-of-flight across the dot matches even or odd multiples

of the spin precession time for an angle π. Notably, the results for free 2DEG in the regime with $T_1 \propto \tau_s$ (Fig. 5.3) do not show structure on T_1 because there is a larger spread in the scatter times τ_s. We checked that when we program that impurity scattering in a random direction always occurs after a fixed time τ_s (no spread), we also observe structure on T_1 as a function of L_{mfp} for a free 2DEG (not shown).

The most extreme suppression of T_1 due to confinement is in ballistic quantum dots ($L \ll L_{mfp}$) when the size of the system $L = \langle L_{pr} \rangle$. Figure 5.2c indicates that this is a counter-intuitive result when this condition is met in strong external fields. The various precession axes get more and more aligned when the external field is increased to 10 T in $\hat{\mathbf{x}}$-direction, while the spins are prepared in this direction. Nevertheless, the lowest T_1 value that occurs for the various traces in Fig. 5.1a is for a quantum dot system of $L = 1.1$ μm in a field of $B_{ext} = 10$ T. Due to the initial spin state in the $\hat{\mathbf{x}}$-direction, spins are initially precessing with relatively small cone angles around these effective magnetic fields, and all electrons will maintain a large component in the $\hat{\mathbf{x}}$-direction. This results only in a small reduction of $\langle S_x \rangle$. Further relaxation for the ensemble only progresses when spins hop onto wider precession cone angles, which only occurs at a scatter event. Thus, more scattering leads to more rapid relaxation, in particular when L is an odd multiple of $\langle L_{pr} \rangle$, and most rapidly when $L = \langle L_{pr} \rangle$. The reason that this results in a very fast relaxation mechanism for small systems in strong magnetic fields is that the precession and scatter times that underlie this mechanism are then very short.

5.5 Conclusions

In conclusion, we have shown that the relaxation time T_1 for a spin population in a certain 2DEG material can be strongly decreased when bringing the size of the system from free 2DEG down to micronscale quantum dots. The strongest suppression is found for ballistic systems of a size L that equals the precession length $\langle L_{pr} \rangle$. Here, frequent scattering on the edge of the dot rapidly drives precession onto wider and wider cone angles, and this effect is resonantly enhanced in all systems where L equals an odd multiple of $\langle L_{pr} \rangle$. We believe our results are very useful for comparison to experimental results on this type of systems, since we can use realistic device and SO parameters. Furthermore, the T_1 values that we calculate match very well with our recent experimental results on micronscale quantum dots as presented in Chapter 4 of this thesis [13].

We thank M. J. van Veenhuizen, A. I. Lerescu, J. Liu and T. Last for useful discussions. This work was supported by the Dutch Foundation for Fundamental Research on Matter (FOM) and the Netherlands Organization for Scientific Research (NWO). During the preparation of this manuscript we became aware of similar work underway by S. Lüscher *et al.* [24].

References

[1] For a recent review see R. H. Silsbee, J. Phys.: Cond. Mat. **16**, R179 (2004).

[2] For a recent review see J. Fabian, A. Matos-Abiague, C. Ertler, P. Stano, I. Zutic, Acta Physica Slovaca **57**, 565 (2007); arXiv:0711.1461 (2007).

[3] S. Datta and B. Das, Appl. Phys. Lett **56**, 665 (1990).

[4] I. Ẑutić, J. Fabian, and S. Das Sarma, Rev. Mod. Phys. **76**, 323 (2004).

[5] D. D. Awschalom and M. E. Flatté, Nature Phys. **3**, 153 (2007).

[6] M. I. D'yakonov and V. I. Perel', Sov. Phys. JETP **33**, 1053 (1971); Sov. Phys. Solid State **13**, 3023 (1972).

[7] M. I. D'yakonov and V. Y. Kachorovskii, Sov. Phys. Semicond **20**, 110 (1986).

[8] A. A. Kiselev and K. W. Kim, Phys. Rev. B **61**, 13115 (2000).

[9] R. Hanson *et al.*, Rev. Mod. Phys. **79**, 1217 (2007).

[10] A. V. Khaetskii and Y. V. Nazarov, Phys. Rev. B **61**, 12639 (2000).

[11] A. V. Khaetskii and Y. V. Nazarov, Phys. Rev. B **64**, 125316 (2001).

[12] C. Cohen-Tannoudji, B. Diu, and F. Laloë, *Quantum Mechanics* (John Wiley and Sons, New York, 1977), p. 698.

[13] E. J. Koop *et al.*, arXiv:0801.2699 (2008).

[14] S. M. Frolov *et al.*, arXiv:0801.4021 (2008).

[15] J. B. Miller *et al.*, Phys. Rev. Lett. **90**, 076807 (2003).

[16] R. M. Potok *et al.*, Phys. Rev. Lett. **89**, 266602 (2002).

[17] J. A. Folk *et al.*, Phys. Rev. Lett. **86**, 2102 (2001).

[18] B. I. Halperin *et al.*, Phys. Rev. Lett. **86**, 2106 (2001).

[19] Cheng-Hung Chang, A. G. Mal'schukov, and K. A. Chao, Phys. Rev. B **70**, 245309 (2004).

[20] Y. A. Bychkov and E. I. Rashba, Sov. Phys. JETP, **39**, 78 (1984).

[21] G. Dresselhaus, Phys. Rev. **100**, 580 (1955).

[22] C. P. Slichter, *Principles of Magnetic Resonance*, Springer series in Solid-State Sciences Vol. 1, 3rd ed. (Springer-Verlag, Berlin, 1989), p. 213.

[23] A. G. Mal'shukov and K. A. Chao, Phys Rev. B **61**, R2413 (2000).

[24] S. Lüscher, S. M. Frolov, and J. A. Folk (unpublished).

Chapter 6

Non-local detection of resistance fluctuations of an open quantum dot

Abstract

We investigate quantum fluctuations in the non-local resistance of an open quantum dot which is connected to four reservoirs via quantum point contacts. In this four-terminal quantum dot the voltage path can be separated from the current path. We measured non-local resistance fluctuations of several hundreds of Ohms, which have been characterized as a function of bias voltage, gate voltage and perpendicular magnetic field. The amplitude of the resistance fluctuations is strongly reduced when the coupling between the voltage probes and the dot is enhanced. Along with experimental results, we present a theoretical analysis based on the Landauer-Büttiker formalism. While this theory predicts non-local resistance fluctuations of about 20 times larger amplitude than what has been observed, agreement with theory is very good if it is scaled with a factor that accounts for the influence of orbital dephasing inside the dot. This latter case is in reasonable agreement with an independently determined time scale for orbital dephasing in the dot.

This chapter is based on Ref. 8 on p. 131.

6.1 Introduction

When a conducting solid-state system is smaller than the phase coherence length of the electrons, its electrical conductance is significantly influenced by quantum interference. For diffusive thin films this results in phenomena known as universal conductance fluctuations and weak localization [1, 2, 3, 4]. Similar conductance fluctuations and localization phenomena are observed in micron-scale ballistic quantum dots, since these behave in practice as chaotic cavities due to small shape irregularities in the potential that defines the dot. These conductance fluctuations have been extensively studied for two-terminal quantum dots [5, 6, 7, 8], *i.e.* systems with only a source and a drain contact. However, for quantum dots this two-terminal conductance is often influenced by Coulomb blockade and weak localization effects, which complicate an analysis when one aims at studying other effects.

We present here a study of fluctuations in electron transport in a *four*-terminal ballistic quantum dot. The dot is coupled to four reservoirs via quantum point contacts (QPC). In such a system, the voltage path (with probes at voltage V_+ and V_-) can be separated from the path that is used for applying a bias current I (see Fig. 6.1). Consequently, one can measure so-called *non-local* [9, 10, 11, 12] voltage signals that are purely due to quantum fluctuations of the chemical potential [13] inside the dot, and for which a naive classical analysis predicts a signal very close to zero. For linear response, this is expressed as a non-local resistance $R_{nl} = (V_+ - V_-)/I$ (this non-local resistance will fluctuate around a value that is very close to zero Ohm, and is therefore studied in terms of resistance rather than conductance). Increasing the number of open channels in the voltage probes will result in enhanced dephasing for the electronic interference effects. With a four-terminal system, one can study this directly since it results in a reduction of the amplitude of the non-local resistance fluctuations. Notably, such a reduction of the fluctuation amplitude does not occur upon increasing the number of open channels in a two-terminal system [14]. Furthermore, such a four-terminal systems could be used for studying signals that are due to spin. In a strong magnetic field QPCs can be operated as spin-selective injectors or voltage probes [15]. This can be used to generate and detect an imbalance in the chemical potential for spin-up and spin-down electrons [16], similar to non-local spin-valve effects observed in metallic nanodevices [17]. Also here, a four-terminal dot is an interesting alternative to work on spin physics in dots with two-terminal devices [18, 19, 20]. However, if such a system is smaller than the electron phase

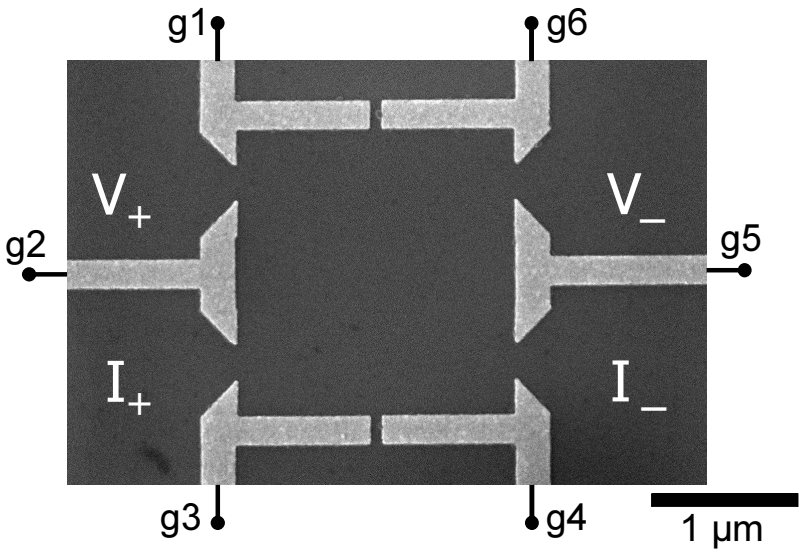

Figure 6.1: Electron microscope image of the device studied in this article. The position of the reservoirs used for current biasing (I_+ and I_-) and voltage probes (V_+ and V_-) is indicated, as well as the numbering of the gates labeled $g1$-$g6$. Unless stated otherwise, all results presented in this article were obtained in this non-local configuration.

coherence length, the non-local signals with information about spin will also show fluctuations that result from interference of electron trajectories [21].

In this chapter, we focus on our first experiments with such a four-terminal quantum dot. We aimed at characterizing the non-local resistance fluctuations, and studying the influence of the voltage probes on the typical amplitude of these fluctuations. As a comparison with our experimental results we present a numerical simulation of the non-local resistance, based on the Landauer-Büttiker formalism [9, 22] and the kicked rotator [23, 24].

The outline of the chapter is as follows: Section 6.2 presents the experimental realization. In section 6.3, we present measurements of the non-local resistance as a function of bias voltage, gate voltage, and magnetic field, and confirm that the observed fluctuations in the non-local resistance are the four-terminal equivalent of universal conductance fluctuations in two-terminal systems. In section 6.4, we analyze how the typical amplitude of the measured non-local resistance fluctuations depends on the number of open channels in the voltage probes. Section 6.5 presents our theoretical analysis with a comparison to the experimental results, before ending with conclusions.

6.2 Experimental realization

Our device was fabricated using a GaAs/$Al_xGa_{1-x}As$ heterostructure containing a two dimensional electron gas (2DEG) 75 nm below the surface, purchased from Sumitomo Electric Co. At 4.2 K, the mobility was $\mu = 86$ m^2/Vs and the electron density was $n_s = 2.4 \cdot 10^{15}$ m^{-2}. The dot was designed with an area of 2×2 μm^2. Figure 6.1 shows and electron microscope image of the device. Six depletion gates were deposited on the surface (15 nm of Au with a Ti sticking layer) and were used for defining the dot in the 2DEG. We estimate that the depletion width around the gates was about 100 nm, such that the electron gas area A_{dot} inside the dot was about 3.2 μm^2. With these six gates the dot could be coupled to the four reservoirs via QPCs in a controllable manner. All four QPCs showed clear quantized conductance steps [25, 26] in measurements where only the corresponding pair of gates were depleting the 2DEG. Note that throughout this article we use that a QPC with a conductance of $2e^2/h$ is defined as having one open channel (denoted as $N = 1$), *i.e.* we neglect spin when counting channels. The four reservoirs were connected to macroscopic leads via Ohmic contacts, which were realized by annealing a thin Au/Ge/Ni layer that was deposited on the surface.

All the measurements were performed with the sample at a temperature of 130 mK. However, the temperature dependence of our data saturated when cooling below $\approx$ 400 mK, so we will assume this value for the effective electron temperature. We used a current bias I with standard ac lock-in techniques at 13 Hz. Unless stated otherwise, we used $I = 1$ nA. The non-local resistance R_{nl} was then recorded as the zero-bias differential resistance dV/dI, with V defined as $V \equiv V_+ - V_-$. We used a floating voltmeter to measure V, thus being insensitive to the voltage across the dot along the current path, and thereby insensitive to Coulomb blockade and weak localization effects. On the current path, only the I_- reservoir was connected to the grounded shielding of our setup, and all gate voltages were applied with respect to this ground.

A magnetic field could be applied, with an angle of 7° with respect to the 2DEG plane (determined from standard Hall measurements and electron focusing effects, discussed below). The perpendicular component of this field was used for studying the dependence of the non-local resistance on perpendicular magnetic field. The component of the magnetic field parallel with the 2DEG plane was oriented perpendicular to the current path. While this parallel field was about ten times stronger than the perpendicular field, the orbital effects associated

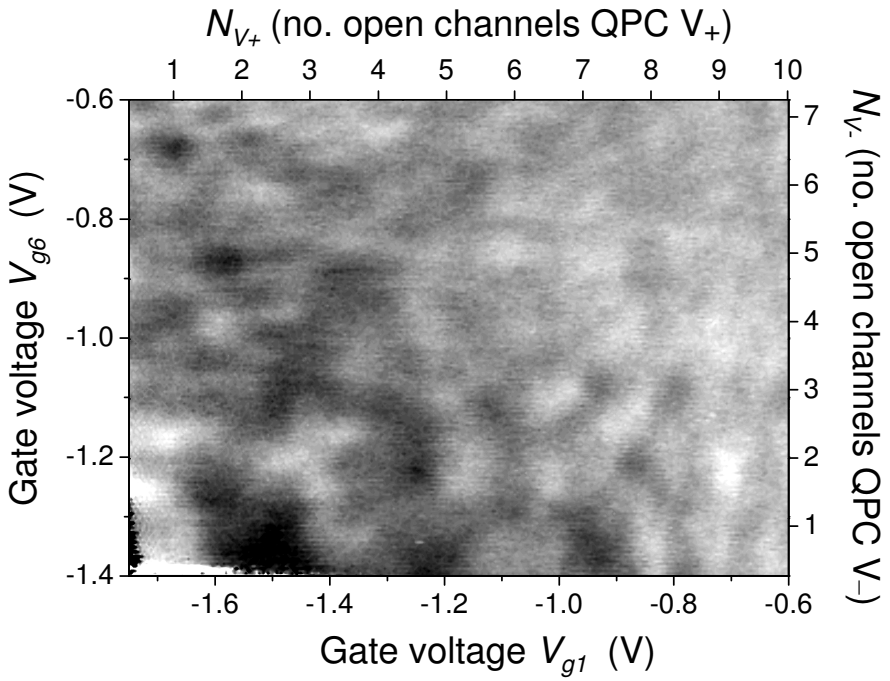

Figure 6.2: Gray scale plot of the non-local resistance R_{nl} as a function the voltages applied to gates $g1$ and $g6$. The axes also show the corresponding number of open channels for the V_+ and V_- probes. The gray scale shows R_{nl} at a scale from $-500\ \Omega$ (black) to $500\ \Omega$ (white). The value of R_{nl} fluctuates around zero Ohm, with a typical amplitude that decreases when the number of open channels in the V_+ and V_- probes increases. The QPCs formed by gates $g2$ and $g3$, as well as $g4$ and $g5$ (defining the current path) had a fixed conductance of $2e^2/h$ each. Data taken in zero magnetic field at 130 mK.

with this parallel field are negligibly small, and it can be disregarded for all of the experimental results presented here (and weak enough to not significantly reduce the amplitude of resistance fluctuations [27, 28, 29]).

6.3 Non-local resistance fluctuations

Figure 6.2 shows the non-local resistance R_{nl} as a function of the voltage applied to gate $g1$ and gate $g6$. The other four gate voltages were kept constant during this measurement, with the QPCs in the current path at a conductance of $2e^2/h$ each (one open channel, $N = 1$). The range of gate voltage for $g1$ and $g6$ used here corresponds to opening the voltage-probe QPCs from nearly pinched off

($N = 0$) up to about $N = 8$ open channels. As a function of these gate voltages, the non-local resistance shows a random pattern of fluctuations around zero Ohm, with maximums and minimums up to about $\pm 500\ \Omega$. Notably, the change in gate voltage needed to change R_{nl} significantly (one fluctuation), is very similar to the change in gate voltage needed for increasing the number of open channels in a QPC by one. This corresponds to changing the shape of the potential that forms the dot by a distance of about half a Fermi wavelength, which is consistent with the length scale needed for significantly changing a random interference pattern of electron trajectories. These non-local resistance fluctuations as a function of the gate voltage on $g1$ and $g6$ were highly reproducible, and indeed a so-called finger print of the sample. The identical measurement repeated after 4 days (during which we performed strong magnetic field sweeps and a temperature cycle up to 4.2 K) showed nominally the same fluctuation pattern as in Fig. 6.2.

In Fig. 6.3 we present results of studying the dependence of the amplitude of the non-local resistance fluctuations on the amplitude of the applied bias current I. The figure shows measurements of R_{nl} as a function of the gate voltage V_{g1}. The results show several fluctuations that are reproducible, but decreasing in amplitude upon increasing the amplitude of the bias current. In this experiment, the conductance of the other three QPCs was fixed at $2e^2/h$. The amplitude of the fluctuations reduces when the measurement averages over contributions of electrons in uncorrelated orbitals, that is, averaging over electrons that differ in energy by more than the Thouless energy [3, 4]. When the current bias is increased, the corresponding voltage bias V_{bias} increases as well (see labels in the Fig. 6.3), and this is used to experimentally estimate the Thouless energy E_{Th} for our system. The amplitude of the fluctuations starts to decrease significantly around $V_{bias} \approx 125\ \mu$V. This is close to a theoretical estimate [30, 31] for $E_{Th} = \frac{\hbar v_F}{L} \approx 80\ \mu$eV, where v_F the Fermi velocity and L the effective width of the dot.

We now turn to measurements of the non-local resistance as a function of perpendicular magnetic field, presented in Fig. 6.4a. Here the conductance of all four QPCs was fixed at $2e^2/h$. The trace of R_{nl} shows random fluctuations of similar amplitude as observed in the gate voltage dependence. For estimating the typical magnetic field scale that significantly changes the value of R_{nl} (the correlation field ΔB_c), we apply an established method from such studies on similar two-terminal quantum dot systems (following Refs. [32, 33]). For this, we took the averaged power spectrum $S_B(f_B)$ of traces as in Fig. 6.4a (only using the low-field data in the range ± 140 mT, see below). On a logarithmic scale, $S_B(f_B)$ closely resembles a straight line with negative slope in the fre-

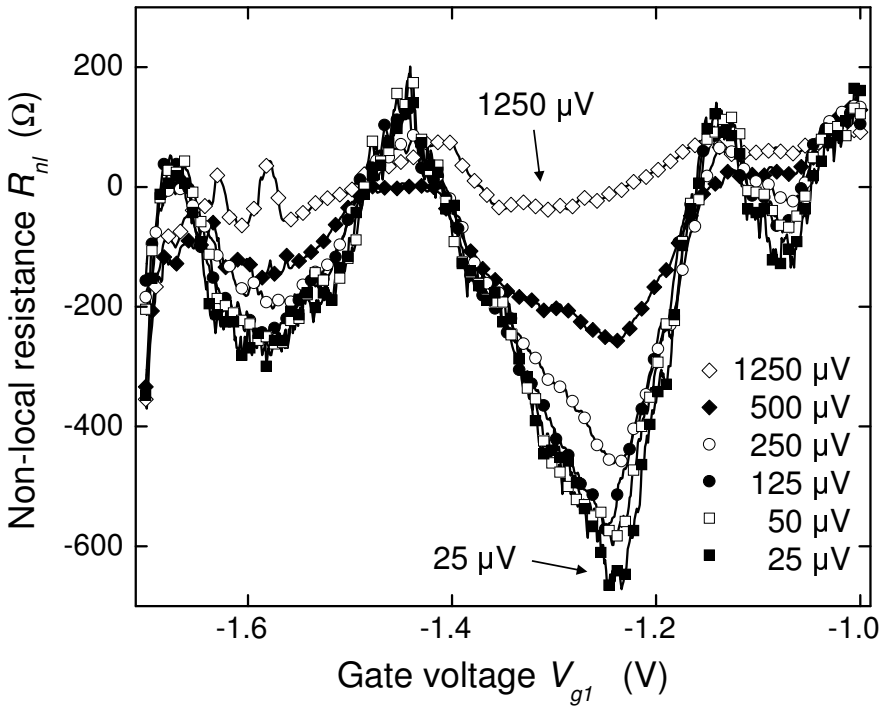

Figure 6.3: The non-local resistance R_{nl} as a function of the voltage V_{g1} applied to gate $g1$, taken for different amplitudes of the bias current I in the lock-in detection scheme (from 1 nA up to 50 nA). The legend shows the corresponding values for the voltage drop across the quantum dot along the current path, obtained as $V_{bias} \approx I \times \frac{2}{2e^2/h}$. The curves show a reduction of the amplitude of the non-local resistance fluctuations with increasing V_{bias}. The conductance of the QPC formed by $g5$ and $g6$ (defining the V_- probe) is set at $2e^2/h$. For further experimental parameters see Fig. 6.2.

quency range between $f_B = 0.05$ and 0.5 cycles per mT (and then levels off), very similar to the results from the studies with two-terminal dots [32, 33]. We fit this part of the spectrum to the form predicted by semiclassical theory [32, 33], $S_B(f_B) = S_B(0)(1 + 2\pi\alpha\phi_0 f_B) \cdot \exp(-2\pi\alpha\phi_0 f_B)$, where $\phi_0 = h/e$ the flux quantum, and α the inverse of an effective area for orbitals in the dot which defines $\Delta B_c = \alpha\phi_0$. This yields $\Delta B_c = 2.1 \pm 0.8$mT (the large error bar must be assumed since we could only measure a small number of independent fluctuations for this analysis). This is in good agreement with theory for universal conductance fluctuations [3], which predicts $\Delta B_c \approx \frac{\phi_0}{A_{dot}} = 1.3$ mT (simply expressing the magnetic field needed for adding one flux quantum ϕ_0 through the area of the dot). It is commonly observed that ΔB_c is enhanced by a factor up to about

~ 2 due to flux cancelation effects for electrons that move ballistically between the edges of the dot [34, 2, 30]. The measured value for ΔB_c is also in agreement with the observation of a weak-localization peak around zero magnetic field [3] observed in the two-terminal resistance (breaking the time-reversal symmetry), which has a width of the same order of magnitude as ΔB_c.

For confirming that changing the field by more than ΔB_c gives access to a statistically independent set of fluctuations, we studied fluctuations in R_{nl} as a function of gate voltage V_{g1}, for different values of the perpendicular field (Fig. 6.4b). This data confirms that changing the perpendicular magnetic field in steps of 14 mT gives access to completely different patterns of random fluctuations in R_{nl}.

The inset of Fig. 6.4a shows the appearance of much higher peaks in R_{nl} (up to 3 kΩ) for perpendicular magnetic fields stronger than $\pm$140 mT. We could confirm that these peaks are due to electron focusing and skipping orbit effects. With only the three gates $g1$, $g2$ and $g3$ depleting the 2DEG, our device is identical to devices used for electron focusing experiments by Van Houten *et al.* [35], and we observe very similar focusing peaks as in this work at only one polarity of the magnetic field. With the dot formed, these effects cause peaks in R_{nl} at both polarities of the magnetic field. The onset of these effects at $\pm$140 mT agrees with a focusing radius of about 1 μm.

6.4 Influence of voltage probes

The presence of additional voltage probes on a quantum dot system will act as source of dephasing for the electrons in the dot, and this effect should increase when the coupling between the dot and the probe reservoirs is enhanced. Earlier work recognized that non-local voltage probes on a mesoscopic system are a source of dephasing [36, 37], and in theoretical work an additional voltage probe is often used to model a source of dephasing [38, 39]. This can be directly studied with our system. The amplitude of the non-local resistance fluctuations (which result from electron phase coherence) should decrease when the voltage probes are tuned to carry more open channels. To study this effect we used data sets of the type presented in Fig. 6.2. We concentrate on the case where the time-reversal symmetry is broken ($\beta = 2$) by applying weak magnetic fields, since this allows us to get statistics from a larger set of data.

For a data set as in Fig. 6.2, the total number of open channels in the voltage probes ($N_{V+} + N_{V-}$) is lowest in the bottom left corner of the graph, and highest

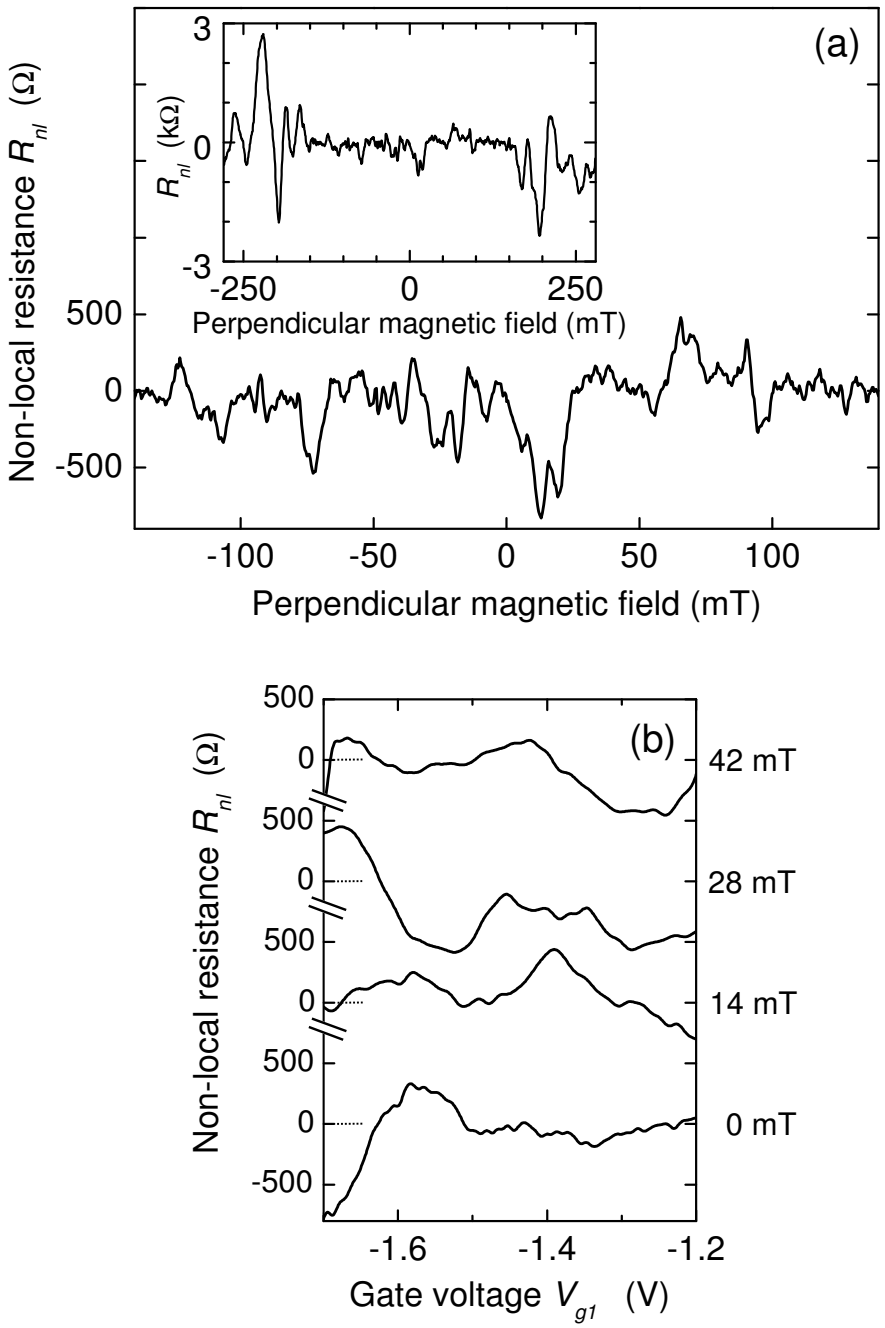

Figure 6.4: **(a)** The non-local resistance R_{nl} as a function of magnetic field. The magnetic field is given on the scale of the perpendicular component of the total applied field. For this measurement all four QPCs are defined to have a conductance of $2e^2/h$. The inset presents the same data for a wider range of the magnetic field, showing the onset of electron focusing effects for perpendicular fields larger than ± 140 mT. The curves in **(b)** show the non-local resistance as a function of the voltage applied to gate $g1$ at different values of the perpendicular magnetic field. The conductance of the QPC formed by $g5$ and $g6$ (defining the V_- probe) is kept at $2e^2/h$. For further experimental parameters see Fig. 6.2.

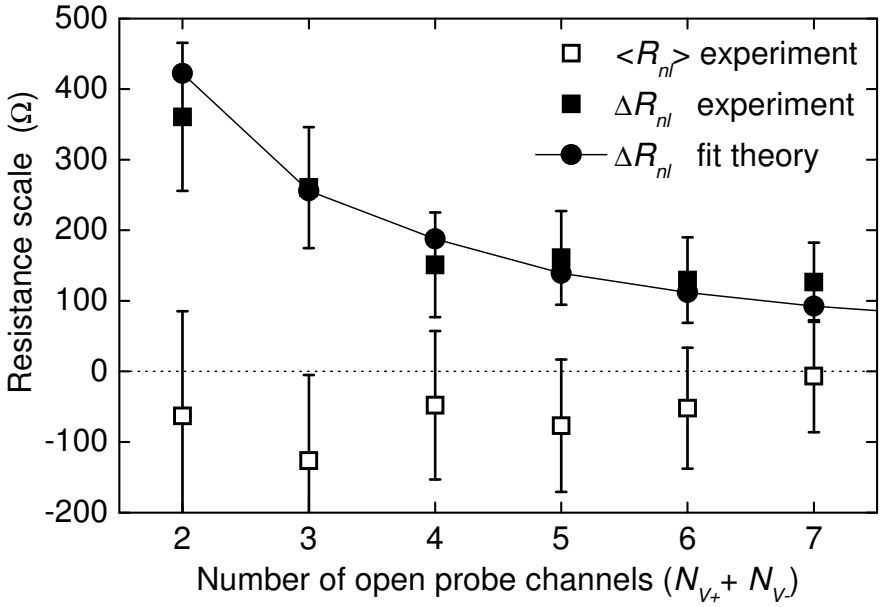

Figure 6.5: Dependence of the mean $\langle R_{nl} \rangle$ and rms standard deviation ΔR_{nl} of fluctuations in the measured non-local resistance R_{nl}, as a function of the total number open of channels in the voltage probes $N_{V+} + N_{V-}$ (squared dots). The statistics are from sets of data as in Fig. 6.2, but with time-reversal symmetry broken by weak magnetic fields ($\beta = 2$). The round dots with solid line present a fit of the theoretical model that describes the values of ΔR_{nl} (see text for details).

in the top right corner. Inspection of R_{nl} in Fig. 6.2 confirms that the typical amplitude of the fluctuations decreases when the voltage probes get more open channels. For a more quantitative analysis of this observation, we determined the mean $\langle R_{nl} \rangle$ and root-mean-square (rms) standard deviation ΔR_{nl} of the non-local resistance for traces recorded at a fixed number of channels in the voltage probes. This can be obtained by following R_{nl} along lines with constant $N_{V+} + N_{V-}$. The theory in the next section shows that, on such a line, ΔR_{nl} should also show a weak dependence on N_{V+} - N_{V-}. However, we do not have sufficient data to study this, and simply average along lines with constant $N_{V+} + N_{V-}$. The results of this analysis are presented in Fig. 6.5. The large error bars for $\langle R_{nl} \rangle$ and ΔR_{nl} in Fig. 6.5 are due to the fact that we could only record a finite number of independent data sets with fluctuations in R_{nl} (see Ref. [40] for further details).

The results in Fig. 6.5 confirm that $\langle R_{nl} \rangle$ is very close to zero, for all values of $N_{V+} + N_{V-}$. More interestingly, ΔR_{nl} smoothly decreases as a function $N_{V+} +$

N_{V-}, demonstrating directly the dephasing influence of the voltage probes for the electrons in the quantum dot. The typical fluctuation amplitude approaches zero when the dot becomes fully open (very strong coupling to a reservoir). For a quantitative evaluation of this observation, we will first present a theoretical model in the next Section.

6.5 Theoretical analysis and discussion

For our theoretical modeling we consider a ballistic chaotic cavity connected to four reservoirs through quantum point contacts. A net current I flows between two of the contacts (from I_+ to I_-), while there is no net current flowing into two contacts used as voltage probes (contacts V_+ and V_-). We use the Landauer-Büttiker formalism to derive the relations between the current I and the voltages of the four contacts [21],

$$I = \frac{1}{2}\left(\frac{2e^2}{h}\right)[((N_1 - T_{11}) + (N_2 - T_{22}) + T_{12} + T_{21})\,\frac{V_{bias}}{2} + (T_{23} - T_{13})V_3 + (T_{24} - T_{14})V_4], \tag{6.1a}$$

$$V_3 = \frac{V_{bias}}{2}\frac{(N_4 - T_{44})(T_{31} - T_{32}) + T_{34}(T_{41} - T_{42})}{(N_3 - T_{33})(N_4 - T_{44}) - T_{34}T_{43}}, \tag{6.1b}$$

$$V_4 = \frac{V_{bias}}{2}\frac{(N_3 - T_{33})(T_{41} - T_{42}) + T_{43}(T_{31} - T_{32})}{(N_3 - T_{33})(N_4 - T_{44}) - T_{34}T_{43}}, \tag{6.1c}$$

where we used (for concise labeling) notation according to

$$\begin{aligned} I_+ &\leftrightarrow 1, \\ I_- &\leftrightarrow 2, \\ V_+ &\leftrightarrow 3, \\ V_- &\leftrightarrow 4. \end{aligned}$$

Here the T_{ij} are the transmission probabilities from contact i to j, while the N_i are the number of open channels in contact i. The voltages V_i are all defined with respect to a ground [41] which is defined such that $V_1 = +V_{bias}/2$ and $V_2 = -V_{bias}/2$, where $V_{bias} = V_1 - V_2$ is the voltage across the dot in the current path that is consistent with a bias current I. The measured voltage V in the experiments corresponds to the quantity $V = V_3 - V_4$, and the non-local resistance is then

$$R_{nl} = \frac{V_3 - V_4}{I}. \tag{6.2}$$

We obtain the mean and root-mean-square (rms) of the R_{nl} by generating a set of random scattering matrices with the kicked rotator [23, 24]. The kicked rotator gives a stroboscopic description of the dynamics in the quantum dot, which is a good approximation of the real dynamics for time scales larger then the time of flight across the dot. The particular implementation we used is described in detail in Ref. [42]. In a certain parameter range, this model gives results which are equivalent to random matrix theory [3]. In our simulations we use parameters in this range, the details of which can be found in Ref. [42].

Figure 6.6 presents the results from these numerical simulations. We focus on analysis of the fluctuations in R_{nl}, since the mean values of R_{nl} simply always gave zero, in agreement with the experimental results [21]. Figure 6.6a shows the dependence of the fluctuations in R_{nl} on the total number of open channels in the voltage probes $N_{V+} + N_{V-}$, for systems with time-reversal symmetry ($\beta = 1$) and broken time-reversal symmetry ($\beta = 2$). The results in Fig. 6.6b show that the fluctuations in R_{nl} have (besides a strong dependence on $N_{V+} + N_{V-}$ as in Fig. 6.6a) a weak dependence on the difference N_{V+} - N_{V-} (presented only for the case $\beta = 2$). This is not further studied in detail, and the results in Fig. 6.6a present values that are averaged over all the possible combinations N_{V+} - N_{V-}, as in the analysis of the experimental results.

Qualitatively, the theoretical results of Fig. 6.6a agree very well with the experimental results of Fig. 6.5. However, while the model system gives non-local resistance R_{nl} values that fluctuate with an rms value of a few kΩ, the experimental values ($\beta = 2$) are only of order 200 Ω. The numerical and experimental values differ by a factor of about 20, as illustrated by the fit in Fig. 6.5: Fitting the theoretical data points of Fig. 6.6 on the experimental values, using a simple pre-factor that scales the theoretical values as fitting parameter, gives $0.05 \approx \frac{1}{20}$ for this pre-factor.

The discrepancy between the numerical and the experimental results is most likely due to orbital dephasing for electrons inside the quantum dot. Moreover, such dephasing is possibly consistent with the simple scaling that was needed to obtain agreement between theory and experiment. Theory for two-terminal quantum dots gives that the influence of dephasing on the amplitude of conductance fluctuations is that it scales the amplitude down by a factor $(1 + \tau_d/\tau_\phi)$, where τ_d is the mean dwell time in the dot and τ_ϕ is the dephasing time [43, 38]. Assuming a similar approach for our system, then gives $(1 + \tau_d/\tau_\phi) \approx 20$. However, it is at this stage not clear whether this theory work for two-terminal dots can be applied to our system, and we can also not rule out that the effective

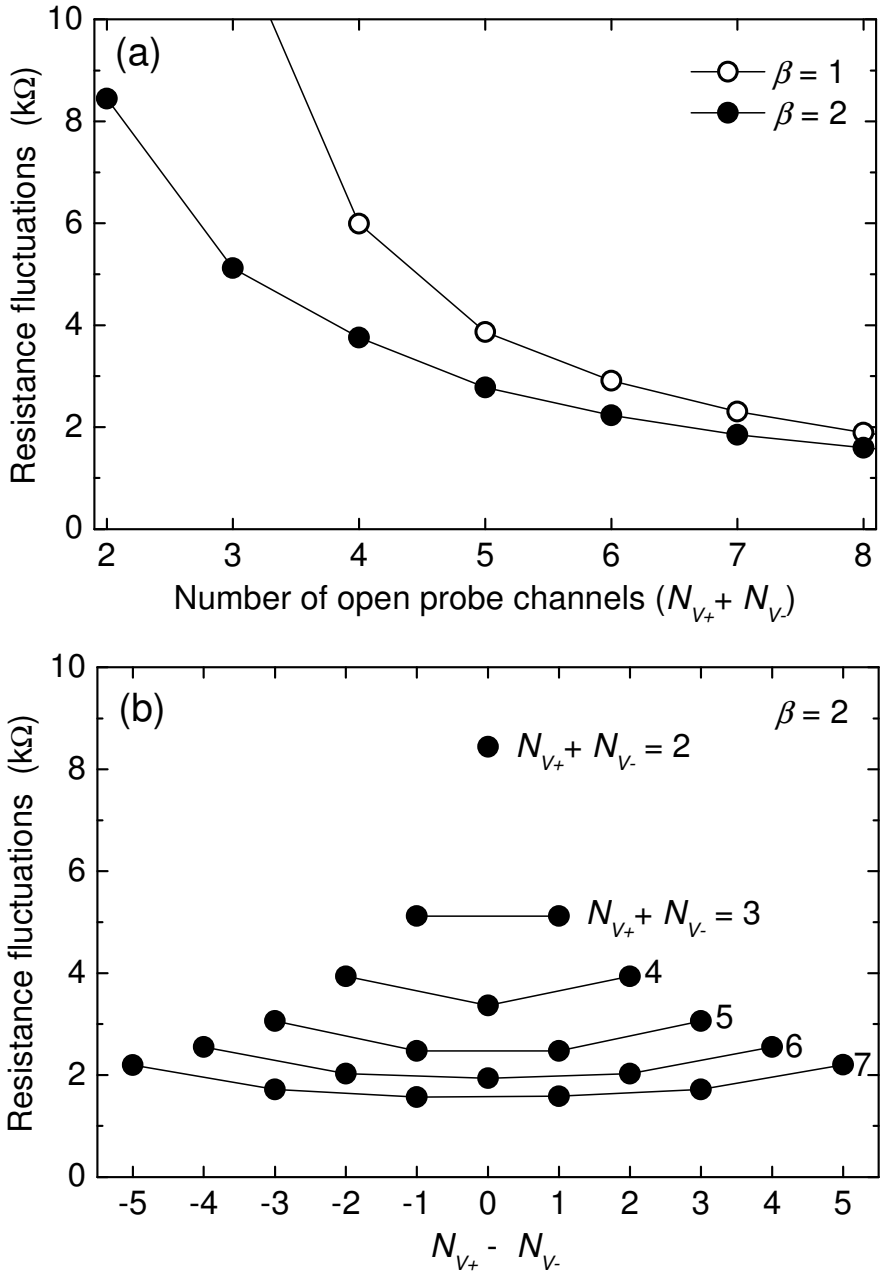

Figure 6.6: **(a)** Theoretical rms values of fluctuations in the non-local resistance (ΔR_{nl}), as a function of the total number open of channels in the voltage probes $N_{V+} + N_{V-}$. The two curves present results for a system with ($\beta = 1$) and without ($\beta = 2$) time-reversal symmetry. The QPCs for the current path were assumed to have a conductance of $2e^2/h$. The data is obtained from a Landauer-Büttiker description of the quantum dot system and numerical simulations based on random matrix theory. **(b)** Theoretical rms values of fluctuations in R_{nl}, as a function of the difference in number open of channels in the two voltage probes, $N_{V+} - N_{V-}$, at fixed values of $N_{V+} + N_{V-}$. The data in a) presents ΔR_{nl} values for $N_{V+} + N_{V-}$, that have been averaged over all possible combinations of $N_{V+} - N_{V-}$.

electron temperature of about 400 mK plays a role in reducing the fluctuation amplitude. Nevertheless, it is interesting to compare the factor $(1 + \tau_d/\tau_\phi)$ that we need to use here to independently determined values for τ_d and τ_ϕ.

For the dwell time we use the expression[32] $\tau_d = h/N_\Sigma\Delta_m$, where N_Σ the total number of open modes in the contacts to the dot, and $\Delta_m = 2\pi\hbar^2/m^*A_{dot}$ the mean spacing between energy levels in the dot. This gives $\tau_d \approx 470$ ps for our system tuned to have all four QPCs at $N = 1$. The most reliable method for estimating the dephasing time τ_ϕ is based on a measurement of the depth of the weak localization dip in the two-terminal conductance [30, 5]. In such measurements on our system (with all four QPCs tuned to $N = 1$) we observed a weak localization dip of $\delta g = 0.045 \pm 0.01(e^2/h)$ in a background of $0.88(e^2/h)$ (the large error bar is again due to the fact that we could only average over a few independent fluctuations in the two-terminal conductance). Following Refs. [30, 5], we derive the dephasing time using $\delta g = (e^2/h) \cdot N/(2N + N_\phi)$ and $\tau_\phi = h/N_\phi\Delta_m$. Here N_ϕ is the number of open modes to a fictitious voltage probe that is responsible for dephasing in the dot, and N is now the number of modes per lead for a two-terminal dot, so we set it to $N = 2$ for our system with four QPCs tuned to $N = 1$. This yields $N_\phi \approx 40$ and $\tau_\phi = 46 \pm 12$ ps for our system at ~ 400 mK, in reasonable agreement with earlier two-terminal studies on similar systems [30, 5, 31].

The independently determined values for τ_d and τ_ϕ give for the factor $(1 + \tau_d/\tau_\phi) \approx 11$, which differs only by a factor ~ 2 from the value 20 that we obtained from the scaling. This supports the assumption that the reduction in the fluctuation amplitude ΔR_{nl} is due to orbital dephasing inside the dot. However, the above analysis is only valid for all QPCs of the dot tuned to $N = 1$. While we can apply a single scaling factor for all values of $N_{V+} + N_{V-}$ in Fig. 6.5, τ_d decreases in fact significantly with increasing $N_{V+} + N_{V-}$. Moreover, it is tempting to consider that the reduction in ΔR_{nl} can be understood by assuming that dephasing in the dot increases the value of $N_{V+} + N_{V-}$ to an effective value of $N_{V+} + N_{V-} + N_\phi$. However, this is clearly not in agreement with the observed drop in ΔR_{nl} over the interval $N_{V+} + N_{V-}$ in Fig. 6.5. This indicates that new theoretical work specific for the role of dephasing for a four-terminal dot is needed for a complete understanding of the data in Fig. 6.5.

6.6 Conclusions

We investigated quantum fluctuations in electron transport with a ballistic, chaotic quantum dot that was strongly coupled to four reservoirs via quantum point contacts. The four-terminal geometry allowed for studying fluctuations in the non-local resistance. We used the dependence of the non-local resistance fluctuations on bias voltage, gate voltage and magnetic field to show that these are the equivalent of universal conductance fluctuations in two-terminal systems, and we showed that with a four-terminal system these fluctuations can be studied without being hindered by Coulomb-blockade and weak-localization effects. Furthermore, the four-terminal geometry was used to demonstrate directly that the amplitude of fluctuations in electron transport is reduced when the coupling between a quantum dot system and voltage probes is enhanced. Here, we obtain good qualitative agreement with a model based on Landauer-Büttiker formalism and random matrix theory, but a quantitative evaluation indicates that there is an intrinsic orbital dephasing mechanism that reduces the amplitude of the non-local resistance fluctuations. Our results are of importance for further work with four-terminal quantum dots on dephasing and electron-spin dynamics in such systems, where the electron-transport signals of interest will always have fluctuations of the type that is reported here.

We thank Dominik Zumbühl and Carlo Beenakker for discussions, and the Dutch Foundation for Fundamental Research on Matter (FOM) for financial support.

References

[1] B. L. Al'tshuler and P. A. Lee, Physics Today, Issue of December 1988, p. 36.

[2] C. W. J. Beenakker and H. van Houten, Sol. State Phys. **44**, 1 (1991).

[3] C. W. J. Beenakker, Rev. Mod. Phys. **69**, 731 (1997).

[4] Y. Imry, *Introduction to Mesoscopic Physics*, Oxford University Press, Oxford, 2002.

[5] A. G. Huibers, M. Switkes, and C. M. Marcus, Phys. Rev. Lett. **81**, 200 (1998).

[6] A. G. Huibers *et al.*, Phys. Rev. Lett. **81**, 1917 (1998).

[7] E. R. P. Alves and C. H. Lewenkopf, Phys. Rev. Lett. **88**, 256805 (2002).

[8] D. M. Zumbühl *et al.*, Phys. Rev. B **72**, 081305 (2005).

[9] M. Büttiker, Phys. Rev. Lett. **57**, 1761 (1986).

[10] A. Benoit *et al.*, Phys. Rev. Lett. **58**, 2343 (1987).

[11] W. J. Skocpol *et al.*, Phys. Rev. Lett. **58**, 2347 (1987).

[12] H. Haucke *et al.*, Phys. Rev. B **41**, 12454 (1990).

[13] M. Büttiker, Phys. Rev. B **40**, 3409 (1989).

[14] H. U. Baranger and P. A. Mello, Phys. Rev. Lett. **73**, 142 (1994).

[15] R. M. Potok *et al.*, Phys. Rev. Lett. **89**, 266602 (2002).

[16] A. Venkatesan *et al.*, 2007 March Meeting Bulletin of the American Physical Society (unpublished), Abstract H12.00012.

[17] F. J. Jedema, A. T. Filip, and B.J. van Wees, Nature **410**, 345 (2001).

[18] J. A. Folk *et al.*, Science **299**, 679 (2003).

[19] D. M. Zumbühl *et al.*, 2001 March Meeting Bulletin of the American Physical Society (unpublished), Abstract C25.006.

[20] C. W. J. Beenakker, Phys. Rev. B **73**, 201304 (2006).

[21] J. H. Bardarson, I. Adagideli, and P. Jacquod, Phys. Rev. Lett. **98**, 196601 (2007).

[22] R. Landauer, IBM J. Res. Dev. **1**, 223 (1957).

[23] F. M. Izrailev, Phys. Rep. **196**, 299 (1990).

[24] Y.V. Fyodorov and H.-J. Sommers, JETP Lett. **72**, 422 (2000).

[25] B. J van Wees *et al.*, Phys. Rev. Lett. **60**, 848 (1988).

[26] D. A. Wharam *et al.*, J. Phys. C: Solid State Phys. **21**, L209 (1988).

[27] P. Debray *et al.*, Phys. Rev. Lett. **63**, 2264 (1989).

[28] J. A. Folk *et al.*, Phys. Rev. Lett. **86**, 2102 (2001).

[29] D. M. Zumbühl *et al.*, Phys. Rev. B **69**, 121305 (2004).

[30] C. M. Marcus *et al.*, Chaos Solitons Fractals **8**, 1261 (1997); cond-mat/9703038.

[31] A. G. Huibers *et al.*, Phys. Rev. Lett. **83**, 5090 (1999).

[32] C. M. Marcus *et al.*, Phys. Rev. B **48**, 2460 (1993).

[33] I. H. Chan *et al.*, Phys. Rev. Lett. **74**, 3876 (1995).

[34] C. W. J. Beenakker and H. van Houten, Phys. Rev. B **37**, 6544 (1988).

[35] H. van Houten *et al.*, Phys. Rev. B **39**, 8556 (1989).

[36] K. Kobayashi *et al.*, J. Phys. Soc. Japan, **71**, 2094 (2002).

[37] G. Seelig *et al.*, Phys. Rev. B **68**, 161310 (2003).

[38] P. W. Brouwer and C. W. J. Beenakker, Phys. Rev. B **51**, 7739 (1995).

[39] P. W. Brouwer and C. W. J. Beenakker, Phys. Rev. B **55**, 4695 (1997).

[40] Analysis of the error bars is in particular relevant for low values of $N_{V+} + N_{V-}$, for which we could only obtain a few independent fluctuations. We used that we had the largest amount of data for traces with $N_{V+} + N_{V-} = 7$. Here we had sufficient data to estimate $\Delta R_{nl} = 126 \pm 56\ \Omega$. For traces with lower $N_{V+} + N_{V-}$, we used that the number of independent fluctuations n_f along a trace with constant $N_{V+} + N_{V-}$ is simply proportional to $N_{V+} + N_{V-}$ for data sets as in Fig. 6.2, since it is proportional to the trace length through the data set. We assume a gaussian distribution for the fluctuations. Then, we used that for a finite number n_f of independent fluctuations, the error bar for $\langle R_{nl} \rangle$ depends on n_f as $1/\sqrt{n_f}$, and for ΔR_{nl} (on the same scale) as $1/\sqrt{2n_f}$.

[41] Note that this definition for ground differs from the grounding used the in the experiment. However, since in our experiments the values of the gate voltages were much larger than the values of V_{bias}, our theoretical model is a valid description of the experiment.

[42] J. H. Bardarson, J. Tworzydło, and C. W. J. Beenakker, Phys. Rev. B **72**, 235305 (2005).

[43] H. U. Baranger and P. A. Mello, Phys. Rev. B **51**, 4703 (1995).

Chapter 7

The annealing mechanism of AuGe/Ni/Au ohmic contacts to a two-dimensional electron gas

Ohmic contacts to a two-dimensional electron gas (2DEG) in GaAs heterostructures are often realized by annealing of AuGe/Ni/Au that is deposited on its surface. We studied how the quality of this type of ohmic contact depends on the annealing time and temperature, and how these parameters depend on the depth of the 2DEG below the surface. Combined with transmission electron microscopy and energy-dispersive X-ray spectrometry studies of the annealed contacts, our results allow for identifying the annealing mechanism and describing a model that can predict optimal annealing parameters for a certain heterostructure.

This chapter is based on Ref. 3 on p. 131.

7.1 Introduction

Epitaxially grown GaAs/AlGaAs heterostructures that contain a two-dimensional electron gas (2DEG) are widely used for electron transport studies in low-dimensional systems [1]. Establishing electrical contacts to the 2DEG is a crucial step in device fabrication with these heterostructures. A commonly used recipe for making ohmic contacts is annealing of a AuGe/Ni/Au alloy that has been deposited on the heterostructure surface [2]. High-quality heterostructures are often only available in a limited quantity, and it is desirable to minimize the heating that is needed for annealing the contacts to avoid damaging the heterostructure. A model that predicts optimal annealing times and temperatures for a heterostructure with the 2DEG at a certain depth is therefore very valuable.

We present here a study of the annealing mechanism for this type of ohmic contact, and a model that can predict optimal annealing parameters for a certain heterostructure. We used electron transport experiments to study how the quality of AuGe/Ni/Au based ohmic contacts depends on annealing time and temperature, and how these parameters change with the depth of the 2DEG below the surface. These results confirm that the annealing mechanism cannot be described by a single simple diffusion process. Cross-sectional studies of annealed contacts with Transmission Electron Microscope (TEM) and Energy Dispersive X-ray (EDX) techniques were used for identifying a more complex annealing mechanism, that is in agreement with the results from our electron transport studies.

The AuGe/Ni/Au contact was first introduced by Braslau *et al.* [3] to contact n-GaAs, and several studies aimed at understanding the contact mechanism for this type of contact [4, 5, 6, 7, 8, 9]. Later studies focussed on the formation of an ohmic contact to a 2DEG in a GaAs/AlGaAs heterostructure [10, 11, 12], but do not report how the optimal annealing parameters depend on the depth of the 2DEG below the surface. A number of these studies suggest that a contact is formed because a pattern of Au/Ni/Ge spikes that originate from the metallization penetrate the heterostructure, just beyond the depth of the 2DEG. We observe, instead, a mechanism where metal-rich phases only penetrate the heterostructure over a distance that is shorter than the depth of the 2DEG. The mechanism that results in a good contact is then similar to a process that has been described [5] for contacts to n-GaAs: during annealing, the AuGe/Ni/Au on the surface segregates in Ni and Au domains, where the Ni domains contain most of the Ge. These domains penetrate the heterostructure and grow towards the

2DEG in large grains rather than narrow spikes. For optimal electrical contact conditions the Au and Ni grains do not reach the 2DEG. The contact resistance decreases and the contact becomes ohmic because Ge diffuses deeper, forming a highly doped AlGaAs region between the 2DEG layer and metal-rich phases at the surface [3]. Recently Sai Saravanan *et al.* found that also Ni and Au diffuse deeper into the heterostructure in comparable concentrations as Ge [12]. Nevertheless, we find that even for very long annealing times, when the contact resistance has significantly increased compared to the optimal contact, the Au and Ni-rich phases still do not penetrate the 2DEG.

7.2 Fabrication

We studied annealed AuGe/Ni/Au contacts to three GaAs/AlGaAs heterostructures with the 2DEG at a heterojunction at 70 nm (wafer A), 114 nm (wafer B), and 180 nm (wafer C) below the surface of the wafer. These wafers have similar values for the 2DEG electron density n_s and mobility μ (around $2 \cdot 10^{15}\,\mathrm{m}^{-2}$ and $100\mathrm{m}^2/\mathrm{Vs}$, respectively, results for 4.2 K and samples kept in the dark during cool down). For all three wafers the layer structure (from the surface down) is very similar besides the depth of the 2DEG. The top layer is a ~ 5 nm n-GaAs capping layer, then a $Al_xGa_{1-x}As$ doping layer (Si at $\sim 1 \cdot 10^{18}\,\mathrm{cm}^{-3}$) with $x \approx 0.32$, of thickness 30 nm (A), 72 nm (B) or 140 nm (C). After this follows an undoped $Al_xGa_{1-x}As$ buffer layer (~ 35 nm thick). The 2DEG is located at the interface with the next layer, which is a thick undoped GaAs layer.

We studied 200 x 200 $\mu\mathrm{m}^2$ contacts that were defined by optical lithography on a 1 mm wide and 2 mm long etched mesa. An electron-beam evaporator was used for deposition of subsequently 150 nm AuGe of eutectic composition (12 wt% Ge), 30 nm of Ni and 20 nm of Au. Subsequent annealing took place in a pre-heated quartz furnace tube in a N_2 flow to prevent oxidation. We have used three different annealing temperatures, 400 °C, 450 °C and 500 °C (all higher than the AuGe eutectic melting temperature of 363 °C). The samples were placed on a quartz boat and then moved into the center of the oven for a various annealing times. Figure 7.1a shows the temperature of the surface of the quartz boat as a function of time for an oven temperature of 450 °C. We assume that the sample temperature closely follows the temperature of the quartz boat, since we assured a good thermal contact over the full surface of the sample.

We measured the current-voltage (IV) characteristics of all contacts to determine optimal annealing parameters. We found that a suitable and sufficient

definition for an optimal ohmic contact is a contact with the lowest zero-bias resistance at 4.2 K. The typical resistance for such a contact is $\sim 20\ \Omega$, but we have observed resistances as low as 5 Ω. All contacts defined as optimal in this manner showed highly linear IVs up to at least 1 mV (over and under annealed contacts did show non-linear IVs due to effects like Schottky or tunnel barriers in the contacts). Further, all these optimal contacts showed a strong monotonous reduction of the contact resistance upon lowering the sample temperature from 300 K to 4.2 K. Highly over and under annealed contacts showed an increase of the contact resistance upon cooling to 4.2 K.

7.3 Electrical measurements

We used a current-biased 4-terminal configuration to measure the voltage drop across a single contact, with two terminals attached to the metal bond wire to the ohmic contact, and two others attached via the 2DEG (this allowed us to use a standard sample design in our fabrication facility). We are aware that the Transmission Line Method (TLM) [13] is a better method for determining the exact value of a contact resistance, but this is not needed for our approach. We compare resistances of various annealed contacts that were fabricated under identical conditions besides the variation in annealing time and temperature. Within such a set, we determine which contacts have the lowest contact resistance. When reproducing our results with contacts that were fabricated in a different batch (using the same electron-beam evaporator, but after replenishing the AuGe target), we find that the values of the lowest contact resistance can be different up to a factor 2 around the typical result. We attribute these batch-to-batch fluctuations to variations in the exact composition of the AuGe/Ni/Au layer that we deposit. The optimal annealing times, however, show batch-to-batch fluctuations of only 10%. Thus, our approach for determining optimal annealing conditions does not depend on the absolute value of the contact resistance.

Figure 7.1b shows a typical result, from which we determine the optimal annealing time for contacts to wafer C for the case of annealing with the oven at 450 °C. Contact resistance data that is denoted as $\langle R \rangle$ is the average resistance measured on a set of 8 identical contacts, the error bar is an indication for the standard deviation. The results in Fig. 7.1b show a clear minimum in contact resistance for annealing times near 5 minutes. We fit a parabola (phenomenological ansatz) to the $\log\langle R \rangle$ values of these data points, and define the optimal annealing time as the time coordinate of the minimum of the parabola. In this

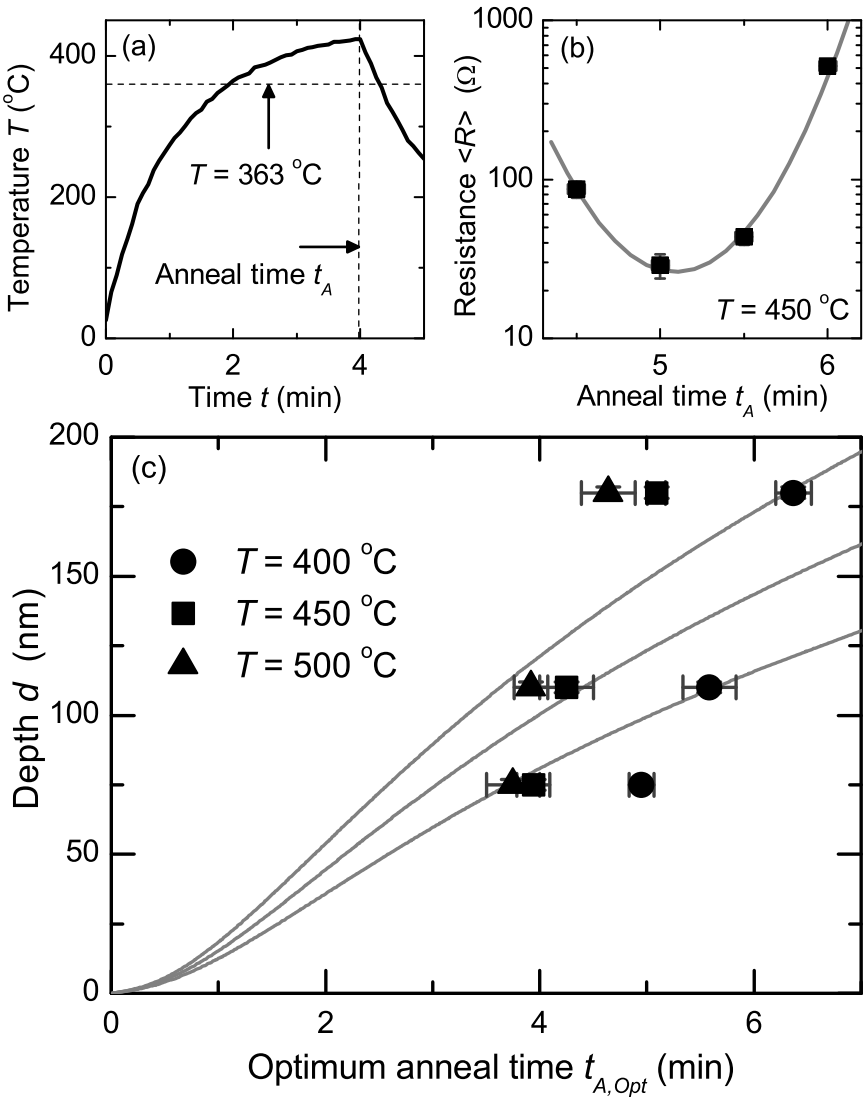

Figure 7.1: **(a)** Temperature of the quartz boat as a function of time for an oven temperature of 450 °C. Horizontal dashed line indicates the AuGe melting temperature $T = 363$ °C. The vertical dashed line indicates our definition of the annealing time t_A, the time at which the boat is taken out of the oven. **(b)** Average contact resistance $\langle R \rangle$ as a function of annealing time t_A for contacts on wafer C, annealed at 450 °C. A parabolic fit is made to estimate the annealing time where the resistance has a minimum. **(c)** Overview of optimal annealing times $t_{A,Opt}$ as a function of depth d of the 2DEG beneath the wafer surface for $T = 400$, 450 and 500 °C. The three gray lines (bottom to top for 400, 450 and 500 °C) are results of fitting a simple diffusion model to the experimental data (see text), which does not yield good fits.

manner, the optimal annealing times $t_{A,Opt}$ are obtained for contacts on wafers A, B and C, annealed at each of the temperatures.

Figure 7.1c presents these optimal annealing times. As expected, the optimal annealing time increases as the temperature is decreased, and increases as the depth d of the 2DEG increases. While it is known that several simultaneous diffusion processes play a role in contact formation [5], we will, for the sake of argument, show that a simple diffusion model has little value for predicting how optimal annealing times depend on the depth d and the annealing temperature. For this simple diffusion model, we assume that a certain dopant (with fixed concentration C_0 at the surface) diffuses into the heterostructure. The relevant solution to Fick's second law is then

$$C = C_0 \; erfc\frac{x}{\sqrt{4Dt}}. \tag{7.1}$$

Here C is the doping concentration at time t and depth x into the heterostructure, and D is the diffusion constant ($erfc$ is complementary error function). Since the temperature of our sample is not constant (see Fig. 7.1a) we will use the measured temperature profile $T(t)$ to integrate the diffusion constant over time, and use in Eq. 7.1 $\int D(t)dt$ instead of Dt, where

$$D(t) = D_0 \; exp(-\frac{E_a}{k_B T(t)}), \tag{7.2}$$

where E_a is an activation energy. We assume that an optimal contact then always occurs for a certain value for C/C_0 at the depth of the 2DEG ($x = d$). We define the annealing time as the time from start to the moment when the boat is taken out of the oven, but integrate over the entire time span that the sample is at elevated temperatures, (as shown in Fig. 7.1a, fully including the cooling down). This gives a model with the activation energy E_a, diffusion constant D_0 and concentration C/C_0 as fitting parameters.

The gray lines Fig. 7.1c shows the best fitting result that reasonably covers all 9 data points in a single fit. Besides the fact that the shape of the traces only poorly matches the trend in the data, the parameter values give unreasonable results. The temperature dependence alone governs the fitting result for E_a, giving here 0.15 eV. This is on the low side for typical values for diffusion in GaAs materials ($\sim$ 1 eV) [7]. For fixed E_a, various combinations of C/C_0 and D_0 give identical results. When assuming a typical value $D_0 \sim 3 \cdot 10^{-7}$ m^2/s (for diffusion of Au in GaAs [7]), this fit yields C/C_0 very close to 1, i.e. completely saturated diffusion. This is in contradiction with the clear dependence on depth

that we observe (and this remains the case when allowing for E_a up to ~ 1 eV, but then the fit does not cover all 9 data points at all). Thus, we find that predicting optimal annealing times with simple diffusion (according to $t_{A,Opt} \propto d^2$ at fixed temperature) does not work and that a more complex model needs to be considered.

7.4 Cross-sectional TEM imaging

We have studied the contact formation using cross-sectional TEM imaging of contacts at several stages during the annealing process. The samples were prepared for TEM imaging by using a Focussed Ion Beam (FIB) to slice out a micrometer thin piece of the measured contact. By further thinning using the FIB, the thickness was reduced to 100 nm.

Figure 7.2a shows an overview of an optimally annealed contact on wafer C which was annealed for 5 minutes at 450 °C. The composition of the various phases has been determined by Energy Dispersive X-ray (EDX) analysis and is illustrated in Fig. 7.2b. From bottom to top we recognize the GaAs substrate, and an AlAs/GaAs superlattice to smoothen the surface of the substrate. On top of that we find another layer of epitaxially grown GaAs and a layer of AlGaAs. The 2DEG is at the interface of these two layers. The GaAs capping layer that was originally on top of the AlGaAs layer is no longer visible. Instead we see large grains of Au and Ni that have penetrated below the original wafer surface. Both of these phases contain some out-diffused Ga and As, and the Ni forms a new phase absorbing most of the Ge. We find that the Au grains do not contain any Ge, consistent with the findings of Kuan *et al.* [5]. The wide and curved dark lines going over all the heterostructure layers (most clearly visible in the GaAs layers) are due to strain induced by the FIB sample preparation and are not related to the diffusion process.

We find that the Au and Ni grains do not have to penetrate the 2DEG in order to establish a good electrical contact. We can rule out that we do not see grains reaching the 2DEG due to the small thickness of the sample slice, since we observed no substantial variation in the penetration depth of a large number of Au and Ni grains going along the sample slice. We examined two slices from two different samples, both with a length of 100 μm, after electrical measurements confirmed that these contacts were indeed optimally annealed.

The TEM image in Fig. 7.2c shows a larger region of an optimally annealed contact. Large Au and Ni grains that have penetrated the AlGaAs layer can

be identified. Figure 7.2d shows an over annealed contact on wafer C, that was annealed for 7 minutes at 450 °C. Remarkably, the Au and Ni grains did not penetrate much further into the AlGaAs, and do still not reach the 2DEG. The most significant change with respect to Fig. 7.2c is that Au is diffusing underneath the Ni grains, reducing the total Ni–AlGaAs interface area. The results of Kuan *et al.* [5] indicate that this process is mainly responsible for the increase in contact resistance when a sample is being over annealed.

Kuan *et al.* [5] report that the contact resistance is sensitive to the ratio of the total contact area between Au regions and AlGaAs, and that of Ni regions. The Au–AlGaAs interface is considered a region of poor conductance because the Au grains (in contrast to Ni grains) do not contain any Ge, such that it cannot act as a source for diffusion of Ge into the heterostructure. However, it is to our knowledge not yet understood why the diffusion of Au underneath the Ni grains at later stages of annealing (when a large amount of Ge already diffused out of Ni) results in a strong increase of the contact resistance.

7.5 Diffusion model

Our qualitative picture of the formation of an ohmic contact is then as follows. In the initial stages of the diffusion process Au and Ge separate, and most Ge forms a new phase with the Ni. At the same time, these Ge-rich Ni grains move to the wafer surface due to a wetting effect, which results in the situation that the wafer surface is covered with neighboring Au and Ni grains. Next, both the Au and Ni grains penetrate into the heterostructure, which is compensated by a back flow of As and Ga into the Au and Ni grains. Meanwhile, Ge diffuses out of the Ni grains into the AlGaAs layer, and a good ohmic contact is formed when the AlGaAs layers are sufficiently doped with Ge al the way up to the 2DEG. In between the metal-rich phases and the 2DEG also some diffused Ni and Au can be found. At the same time Au is diffusing underneath the Ni grains, which have the lowest contact resistance with the doped AlGaAs layer. This increases the interface resistance between the metallization on the surface and the doped AlGaAs layer. Thus, the formation of an optimal contact is a competition between these two processes.

We use the above description to construct a model that predicts the optimal annealing time for a given annealing temperature and 2DEG depth d. The contact resistance is then the series resistance of the resistance of the Ge-doped AlGaAs region (R_{Ge}) and the interface resistance between the surface metallization and

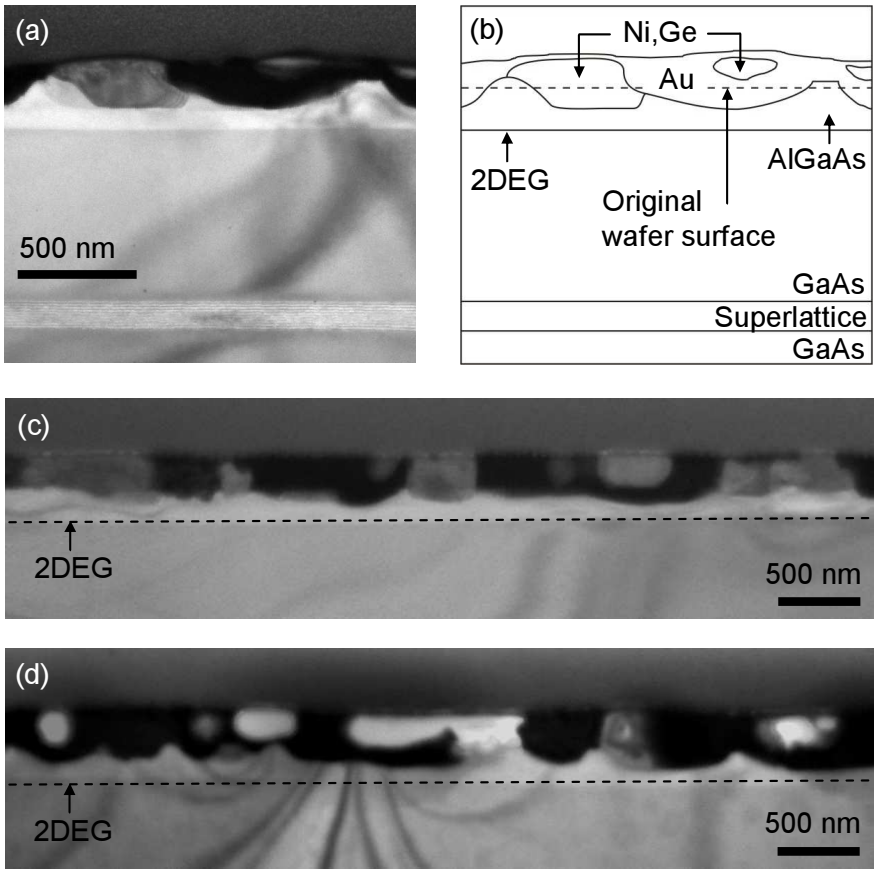

Figure 7.2: **(a)** Cross-section TEM image of a contact on wafer C, annealed for the optimal annealing time at 450 °C. **(b)** A sketch of the TEM image in **(a)** to specify the various layers and phases. **(c)** Larger area TEM image of the same contact as in **(a)** showing large Au (black) and Ni grains (dark gray) contacting the AlGaAs. **(d)** Similar image for a highly over annealed contact. The Au and Ni grains still do not penetrate the 2DEG, but Au has diffused underneath the Ni grains, which increases the contact resistance.

this Ge-doped AlGaAs layer (R_{if}). We will first assume an anneal temperature T that is constant in time. We model the resistance of the Ge-doped AlGaAs region using the result from work on n-GaAs that the contact resistance is inversely proportional to the doping concentration [8]. Thus, we assume that

$$R_{Ge} \propto \int \frac{1}{C(x)/C_0} dx, \tag{7.3}$$

where $C(x)/C_0$ is the local Ge concentration at depth x as in Eq. 7.1, and where the integral runs from the depth of the Au and Ni grains to the depth of the

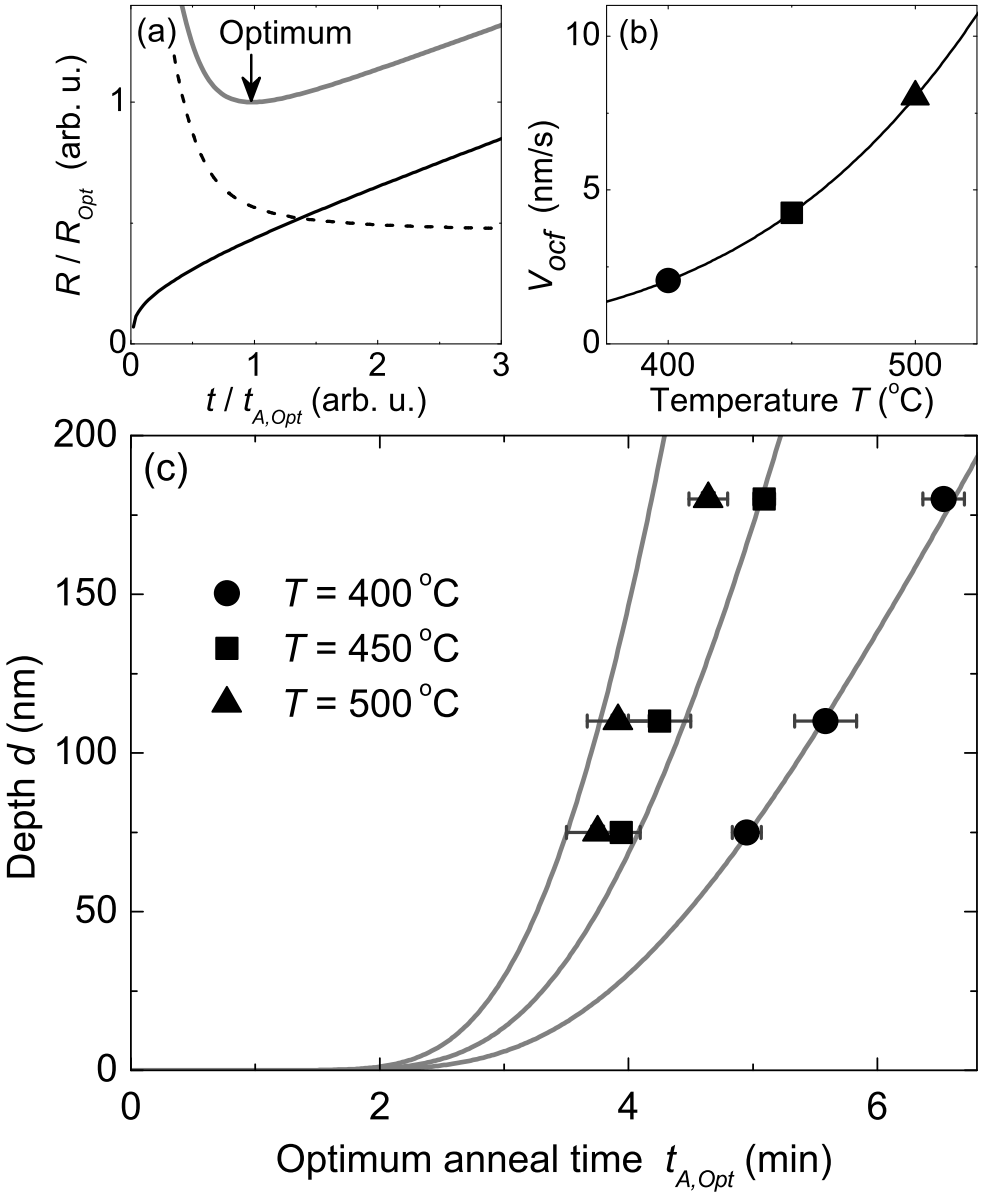

Figure 7.3: **(a)** Model for the resistance of an ohmic contact as a function of annealing time at constant temperature. The resistance R_{Ge} of the AlGaAs layers (dashed line) decreases in time due to increased Ge doping. The interface resistance R_{if} between the surface metallization and the Ge-doped AlGaAs layers (solid black line) increases in time due to a decreasing Ni–AlGaAs interface area. The time where the sum of these two resistances (gray solid line) shows a minimum defines the optimum annealing time $t_{A,Opt}$. **(b)** Effective velocity of optimal contact formation v_{ocf} as a function of temperature (Eq. 7.6), plotted for parameters that give the best fit in **(c)**. **(c)** Change in optimal annealing time as the 2DEG depth is (same experimental data as in Fig. 7.3. The solid gray lines (left to right for 500, 450 and 400 °C) represent fits using the model of Eqs. 7.5 and 7.6 (see text for details).

2DEG. The behavior of this equation is that R_{Ge} first rapidly decreases, and then curves off to saturate at a level that is proportional to d (dashed curve in Fig. 7.3a).

To model R_{if}, we assume that the increase in resistance for over annealed contacts is related to the decrease in Ni–AlGaAs interface area. Imagine, for simplicity, a single, square shaped Ni grain with area $A_{Ni} = L_{Ni}^2$. We model the reduction of this area as a sideways diffusion process of Au, again with a time-dependence as simple diffusion analogues to Eq. 7.1. The length of a side is then reduced as $L_{Ni}(t) \sim L_0 - 2\sqrt{4D_{Au}t}$, where L_0 is the initial grain size, and D_{Au} the diffusion constant for this process, such that

$$R_{if} \propto \frac{1}{(L_0 - 2\sqrt{4D_{Au}t}\,)^2}. \tag{7.4}$$

For a very wide parameter range, this model gives that R_{if} increases more or less linearly in time (solid black curve in Fig. 7.3a). A resistance increase that is much stronger than linear only sets in when the total interface area approaches zero, when the contact is already strongly over annealed. The total contact resistance is the sum of R_{Ge} and R_{if} (gray solid curve Fig. 7.3a), and the optimal annealing time is then defined as the time where this sum shows a minimum value.

We can reduce the number of fitting parameters for this modeling to only two with the following approach. For R_{Ge} in Eq. 7.3, we assume parameters where R_{Ge} saturates at a value below, but on the order of the optimal contact resistance R_{opt}. We also assume that this saturation occurs in a time scale on the order of a few times the optimal annealing time. For R_{if} in Eq. 7.4, we assume that it has a value below R_{opt} for $t = 0$, and that it increases more or less in a linear fashion to a value of order R_{opt}. This increase should take place in a time scale on the order of the optimal annealing time. Numerically investigating this model then shows that it has for a very wide parameter range the behavior that the increase of optimal annealing time $t_{A,Opt}$ with increasing 2DEG depth d is close to linear. We can express this using an effective velocity for optimal contact formation v_{ocf},

$$t_{A,Opt} = d/v_{ocf}. \tag{7.5}$$

Furthermore, numerical investigation of the temperature dependence shows that v_{ocf} behaves according to

$$v_{ocf}(T) = v_0\ exp(-\frac{E_a}{k_B T}) \tag{7.6}$$

when the diffusion processes that underlie Eq. 7.3 and Eq. 7.4 are both thermally activated with a similar activation energy E_a. We can now fit this model to our

experimental data only using Eq. 7.5 and Eq. 7.6, such that we only have v_0 and E_a as fitting parameters. In doing so, we take again into account that the temperature $T(t)$ is not constant during annealing, and use again profiles as in Fig 7.1a.

The results of this fitting are presented in Fig. 7.3c, and v_{ocf} as a function of temperature for these fitting parameters ($E_a = 0.6$ eV and $v_0 = 7.6 \cdot 10^{-5}$ m/s) is plotted in Fig. 7.3b. While it is a crude model, the fits are very reasonable, showing that the model is useful for predicting optimal annealing times. Furthermore, the value for E_a is a realistic number [7]. Our model also predicts that the minimum value of the resistance that can be achieved for optimally annealed contacts increases with increasing 2DEG depth. We did not observe such a clear trend, probably because the resistance of optimal contacts is so low that one needs to include contributions from 2DEG square resistance around and underneath the contact when evaluating absolute values (further discussed below).

Our model for the annealing mechanism implies that optimal contacts have a rather uniform Ge concentration throughout the AlGaAs layers, which results in a value for R_{Ge} of about 10 Ω. This implies that the bulk resistivity in the doped Ge-doped AlGaAs layer is around 4 Ωm. In turn, this implies that in-plane electron transport under an optimal contact from the metallization on the surface to 2DEG on the side of the contact still mainly takes place in the original 2DEG layer. If the square resistance $R_\square$ for transport in the the original 2DEG layer does not strongly increase during annealing ($R_\square$ for 2DEG before annealing is typically 5 Ω), this also implies that the resistance of optimal contacts should be inversely proportional to the contact area. Thus, measuring whether the contact resistance depends on contact area or on the circumference of a contact can give further insight in the annealing mechanism.

We carried out such a study, by varying the shape of contacts. All results that we discussed up to here were obtained with square contacts with an area A of 0.04 mm^2 and a circumference $C_L = 4L$ of 0.8 mm. For the dependence on contact shape, we measured various sets where we varied the circumference C_L while keeping the area constant at 0.04 mm^2, and various sets where we varied the area while keeping the circumference constant at 0.8 mm. We varied the shape from smooth circular shape to square shapes with a zig-zag edge at the 50 micronscale, to avoid getting too much resistance contribution from square resistance of 2DEG right next to a contact (for these devices we used electron-beam lithography). All contacts were fabricated and annealed in one single batch to ensure that it is meaningful to compare the values of contact resistance.

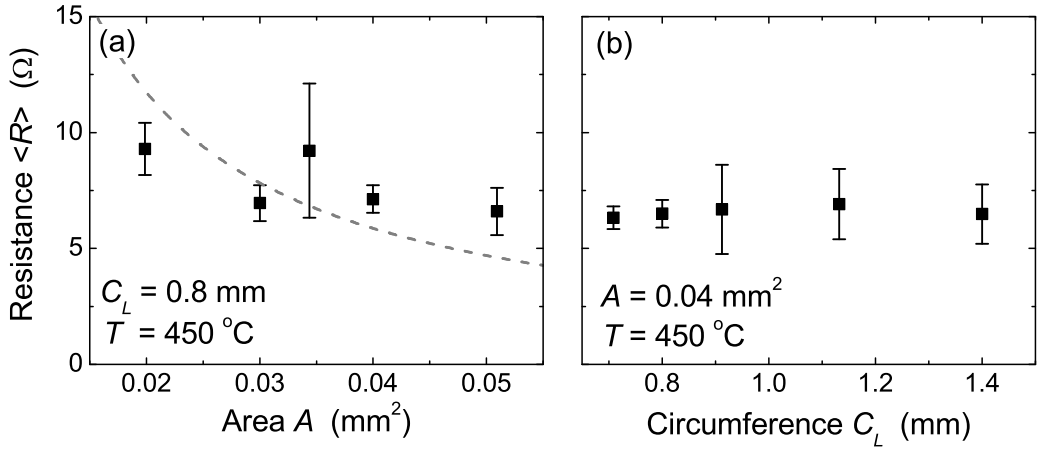

Figure 7.4: Contact resistance $\langle R \rangle$ as a function of **(a)** contact area A for constant circumference $4L$ and **(b)** contact circumference C for constant area A. The error bars here represent the standard deviation from measuring R on 8 identical contacts. The dashed line in **(a)** is a fit using $\langle R \rangle \propto 1/A$.

On contacts that are not annealed, we can observe a tunnel current, as expected for Schottky barriers. Here, the effective resistance is inversely proportional to area. For optimally annealed contacts on wafer A, we found that the contact resistance was independent on circumference, while only showing a very weak dependence on area (much weaker than inversely proportional to area), see Fig. 7.4. The fact that the dependence on shape does here not show a clear dependence as $\langle R \rangle \propto 1/A$ agrees with the fact that the $\langle R \rangle$ values are comparable to the square resistance of the 2DEG, such that the latter gives a significant contribution to the total contact resistance. Fully understanding the contact resistance then requires incorporating all square resistance contributions from underneath and around the 2DEG. Since we found it impossible to estimate these effects with a small error bar, we turned to measuring under annealed contacts instead.

On two sets of under annealed contacts on wafer A, where we used a different anneal time t_A (average contact resistance of 30 Ω and 500 Ω), we found (within error bar) no dependence on area or circumference. We can only explain this result if we assume that the 2DEG square resistance underneath the contact is significantly increased (to values comparable to the total observed contact resistance) for under annealed contacts. This probably results from the in-diffusing Ge, which already introduces strain and scatter centers in the 2DEG layer before optimal contact conditions are reached. For optimal annealed contacts (here

with total resistance of typically 7 Ω, independent of circumference), the square resistance underneath a contact must have returned to a value of less than 10 Ω. Apparently, the resistance increase due to strain and scatter centers is overcompensated by increased Ge doping near the 2DEG layer.

The summary of this study is that we never obtain a clear dependence on circumference, and only a weak dependence on area for optimal contacts. We can, nevertheless, draw the following conclusions. For an optimal ohmic contact, it is *not* the case that electron transport between the surface metallization and the surrounding 2DEG mainly occurs at the edge of a contact. Instead, the full contact area plays a role, and in-plane electron transport under an optimal contact mainly takes place in the original plane of the 2DEG. In addition, we find it impossible to evaluate the absolute values of the contact resistance of our devices with an accuracy within a factor 2, since the resistance of an optimal contact has a contribution from the square resistance underneath the contact, and its value is influenced by the annealing process. We can therefore not study the property of our model that the optimal contact resistance value should be proportional to d. Instead, we should evaluate whether the enhanced square resistance underneath a contact needs to be incorporated in our model. We find that this is not needed for the following reasons: for over annealing it does not play a role, since we observe the same over-annealing mechanism as observed on bulk n-GaAs. Optimally annealed contacts occur when the square resistance underneath the contacts has again values well below 10 Ω. Here we observe a weak area dependence and no dependence on circumference, such that we can rule out that the effect dominates the contact resistance here. Thus, the only effect is that it temporarily enhances the total contact resistance by about a factor 2 while the annealing progresses towards optimal contact conditions. Note that it does not change the fact that lowering the contact resistance in this phase still fully depends on further Ge diffusion towards the 2DEG layer. Therefore, it only slightly modifies how R_{Ge} in Eq. 7.3 decreases towards low values.

7.6 Conclusions

Summarizing, we have measured the zero-bias resistance of annealed AuGe/Ni/Au contacts to a 2DEG as a function of annealing time and temperature. We have thus obtained optimal annealing parameters for three different heterostructures where the 2DEG lies at a different depth with respect to the surface of the wafer. TEM images of several annealed contacts provided further insight into the an-

nealing mechanism and the formation of a good ohmic contact. Combining this information we have developed a model that can predict the optimal annealing parameters for contacting a 2DEG at a certain depth in a GaAs/AlGaAs heterostructure. This model should have predictive value for many heterostructures, as long the temperature of the samples as a function of time during the annealing process is known. Our model may become invalid for systems with a very deep 2DEG, since R_{if} (Eq. 7.4) is expected to increase more rapidly at long annealing times, possibly resulting in non-ohmic behavior. Our model suggests that for solving this problem the focus should be at maintaining sufficient contact area between Ni grains and the Ge-doped AlGaAs layer at long annealing times. This can possibly be engineered by changing the layer thickness, order and composition of the initial AuGe/Ni/Au metallization.

We thank B. H. J. Wolfs, M. Sladkov and S. J. van der Molen for help and valuable discussions, and the Dutch Foundation for Fundamental Research on Matter (FOM) and the Netherlands Organization for Scientific Research (NWO) for funding.

References

[1] See for example C. W. J. Beenakker, H. van Houten, Solid State Physics **44**, 1 (1991).

[2] For a review see A. G. Bacas *et al.*, Thin Solid Films **308-309**, 599 (1997).

[3] N. Braslau, J. B. Gunn, J. L. Staples, Solid State Electronics **10**, 381 (1967).

[4] M. Ogawa, J. Appl. Phys. **51**, 406 (1980).

[5] T. S. Kuan *et al.*, J. Appl. Phys. **54**, 6952 (1983).

[6] A. K. Kulkarni, and C. Lai, J. Vac. Sci. Technology A **6**, 1531 (1987).

[7] A. K. Kulkarni, and C. Lai, Thin Solid Films **164**, 435 (1988).

[8] N. Braslau, J. Vac. Sci. Technology **19**, 803 (1981).

[9] N. Braslau, Thin Solid Films **104**, 391 (1983).

[10] R. P. Taylor *et al.*, J. Appl. Phys. **76**, 7966 (1994).

[11] R. P. Taylor *et al.*, Superlattices and Microstructures **24**, 337 (1998).

[12] G. Sai Saravanan *et al.*, Semicond. Sci. Technol. **23**, 025019 (2008).

[13] H. H. Berger, Solid State Electronics **15**, 145 (1972).

Appendix A

Wafer inventory

In this Appendix we present the various heterostructures used in this thesis. All values for density and mobility were measured at 4.2 K with samples cooled down in the dark. We present the layer structure from top down.

A.1 WSUMI301612

This wafer was purchased from Sumitomo Electric Industries, Ltd. Devices from this wafer were used for experiments on quantum fluctuations in the non-local resistance in Chapter 6 and for studies on ohmic contact formation to a 2DEG in Chapter 7. Quantum point contacts fabricated on this wafer never showed any sign of spin splitting in a large in-plane magnetic field.

- 2DEG depth: 75 nm
- Density: $\sim 3 \times 10^{15}$ m^{-2}
- Mobility: ~ 100 m^2/Vs
- Layer structure:
  - 5 nm GaAs
  - 40 nm $Al_{0.27}Ga_{0.73}As$ (n-doped with Si at 2×10^{18} cm^{-3})
  - 30 nm $Al_{0.27}Ga_{0.73}As$
  - 800 nm GaAs

A.2 WREUT1098

This wafer was grown in the group of D. Reuter and A. D. Wieck at the Ruhr-Universität in Bochum, Germany. Devices from this wafer were used for experiments on point contacts and quantum dots in Chapters 3 and 4, and for studies on ohmic contact formation to a 2DEG in Chapter 7.

- 2DEG Depth: 114 nm
- Density: 1.5×10^{15} m^{-2}
- Mobility: 159 m^2/Vs
- Layer structure:
  - 5.5 nm GaAs
  - 71.9 nm $Al_{0.32}Ga_{0.68}As$ (n-doped with Si at 1×10^{18} cm^{-3})
  - 36.8 nm $Al_{0.32}Ga_{0.68}As$
  - 933 nm GaAs

A.3 WREUT12570

This wafer was grown in the group of D. Reuter and A. D. Wieck at the Ruhr-Universität in Bochum, Germany. Devices from this wafer were used only for studies on ohmic contact formation to a 2DEG in Chapter 7.

- 2DEG Depth: 180 nm
- Density: $\sim 3 \times 10^{15}$ m^{-2}
- Mobility: ~ 100 m^2/Vs
- Layer structure:
  - 5 nm GaAs
  - 70 nm $Al_{0.35}Ga_{0.65}As$
  - 70 nm $Al_{0.35}Ga_{0.65}As$ (n-doped with Si at 1×10^{18} cm^{-3})
  - 35 nm $Al_{0.35}Ga_{0.65}As$
  - 650 nm GaAs

Appendix B

Device fabrication

In this Appendix we will describe the fabrication procedure for the devices that were used in this thesis.

B.1 Alignment markers

- Preparation:
  - Clean in boiling acetone (10')
  - Rinse in IPA (30")
  - Spin dry
- Resist:
  - Spin 250 nm 950K PMMA (4% in Chlorobenzene) - 4000 rpm (60")
  - Bake at 180 ^{o}C (15')
- Exposure:
  - Beam voltage: 10 keV
  - Aperture: 10 μm
  - Working area: 200 x 200 μm
  - E-beam dose: 200 μC/cm^2
- Developing:
  - Develop in 1:3 MIBK / IPA (60")
  - Rinse in IPA (30")

  - Spin dry

- Evaporation:
  - 5 nm Ti
  - 50 nm Au
- Lift-off:
  - Lift-off in acetone (several hours) / acetone spray
  - Rinse in IPA (30")
  - Spin dry

B.2 Mesa etching

- Preparation:
  - Clean in boiling acetone (10')
  - Rinse in IPA (30")
  - Spin dry
- Resist:
  - Spin 70 nm 950K PMMA (2% in Ethyl lactate) - 4000 rpm (60")
  - Bake at 180 °C (15')
- Exposure:
  - Beam voltage: 10 keV
  - Aperture: 120 μm
  - Working area: 2000 x 2000 μm
  - E-beam dose: 150 μC/cm^2
- Developing:
  - Develop in 1:3 MIBK / IPA (35")
  - Rinse in IPA (30")
  - Spin dry

- Etching:
  - Etch in a 1:1:50 solution of H_2SO_4 / H_2O_2 / H_2O (50"). The etching rate is approximately 2 nm/s
  - Rinse in H_2O (30")
  - Spin dry
- Cleaning:
  - Clean in boiling acetone (10')
  - Rinse in IPA (30")
  - Spin dry

B.3 Ohmic contacts

- Preparation:
  - Clean in boiling acetone (10')
  - Rinse in IPA (30")
  - Spin dry
- Resist:
  - Spin 400 nm 50K PMMA (9% in Chlorobenzene) - 4000 rpm (60")
  - Bake at 180 °C (15')
  - Spin 70 nm 950K PMMA (2% in Ethyl lactate) - 4000 rpm (60")
  - Bake at 180 °C (15')
- Exposure:
  - Beam voltage: 10 keV
  - Aperture: 120 μm
  - Working area: 2000 x 2000 μm
  - E-beam dose: 200 μC/cm^2
- Developing:
  - Develop in 1:3 MIBK / IPA (60")

  - Rinse in IPA (30")
  - Spin dry

- Evaporation:
  - 120nm AuGe
  - 30nm Ni
  - 20nm Au

- Lift-off:
  - Lift-off in acetone (several hours) / acetone spray
  - Rinse in IPA (30")
  - Spin dry

- Annealing:
  - Anneal in N_2 atmosphere (50 ml/s) in the oven at 450 °C for typically 5 minutes (see Chapter 7 for more details)

B.4 Fine gates

- Preparation:
  - Clean in boiling acetone (10')
  - Rinse in IPA (30")
  - Spin dry

- Resist:
  - Spin 70 nm 950K PMMA (2% in Ethyl lactate) - 4000 rpm (60")
  - Bake at 180 °C (15')

- Exposure:
  - Beam voltage: 30 keV
  - Aperture: 10 μm
  - Working area: 200 x 200 μm

  - E-beam dose: 450 μC/cm^2

- Developing:
  - Develop in 1:3 MIBK / IPA (35")
  - Rinse in IPA (30")
  - Spin dry

- Evaporation:
  - 5 nm Ti
  - 15 nm Au

- Lift-off:
  - Lift-off in acetone (overnight) / acetone spray
  - Rinse in IPA (30")
  - Spin dry

B.5 Large gates

- Preparation:
  - Clean in boiling acetone (10')
  - Rinse in IPA (30")
  - Spin dry

- Resist:
  - Spin 400 nm 50K PMMA (9% in Chlorobenzene) - 4000 rpm (60")
  - Bake at 180 °C (15')
  - Spin 70 nm 950K PMMA (2% in Ethyl lactate) - 4000 rpm (60")
  - Bake at 180 °C (15')

- Exposure:
  - Beam voltage: 10 keV
  - Aperture: 120 μm

  - Working area: 2000 x 2000 μm
  - E-beam dose: 200 μC/cm^2

- Developing:
  - Develop in 1:3 MIBK / IPA (60")
  - Rinse in IPA (30")
  - Spin dry
- Evaporation:
  - 5 nm Ti
  - 150 nm Au
- Lift-off:
  - Lift-off in acetone (several hours) / acetone spray
  - Rinse in IPA (30")
  - Spin dry

Summary

This thesis presents research that contributes to the understanding of fundamental properties of electrons and electron spin in quantum point contacts and quantum dots. These nanodevices are fabricated with ultra-clean non-magnetic semiconductors, using state-of-the-art nanofabrication techniques. Furthermore, the experiments are done at very low temperatures. This allows for a study of how fundamental interactions in materials influence electron and spin states. Although this work has a fundamental character, it is also motivated by open questions in the field of spintronics regarding the ability to generate, transport, and detect electron spin in a controlled manner. We report research on two types of devices, the quantum point contact and the quantum dot. Both type of devices are defined with electrostatic gating techniques in a two-dimensional electron gas (2DEG) on a GaAs/AlGaAs heterostructure.

The first part of this thesis presents experimental work on Quantum Point Contacts (QPCs). A QPC can be though of as a short one-dimensional transport channel in which the electron transport is ballistic. Due to the transverse confinement, the conductance of a QPC is quantized in steps of $2e^2/h$ in zero magnetic field, where e is the electron charge and h Planck's constant. Furthermore, the electron emission from QPCs can be spin-polarized when a strong in-plane magnetic field is applied. Besides this well understood conductance quantization there are also several features in the conductance of a QPC due to many-body effects that still cannot be fully explained. In particular, the 0.7 anomaly, a shoulder in the conductance around $0.7(2e^2/h)$ in zero magnetic field, has been a topic of debate for more than a decade now. Other many-body effects in QPCs include the enhancement of the electron g-factor, and the zero-bias anomaly, a feature in the QPC conductance that shows similarities with transport though a Kondo impurity.

Since a QPC is one of the most fundamental electronic systems, it makes an ideal model system for studying the consequences of many-body effects for transport of spin-polarized electrons and spin coherence in nanodevices. We per-

formed electron transport measurements to study how these many-body effects in QPCs depend on the QPC geometry. We studied the energy spacing between the one-dimensional subbands and spin-splittings within one-dimensional subbands, both in zero field and high magnetic fields, for a set of 12 QPCs with identical material parameters. We found a clear relation between the subband spacing and the enhancement of the effective electron g-factor. These parameters depend on geometry in a regular manner that we can understand from electrostatic modeling of the QPC potential. The appearance of the 0.7 anomaly does not show a regular dependence on QPC geometry. However, we do find that in high magnetic fields there is a field-independent exchange contribution to the spin-splitting for the lowest one-dimensional subband in addition to the regular Zeeman splitting, and this exchange contribution is clearly correlated with the apparent zero-field splitting of the 0.7 anomaly. This suggests that the splitting of the 0.7 anomaly is dominated by this exchange contribution. Also for the zero-bias anomaly we do not find a clear dependence on QPC geometry, but our data suggests that it is worthwhile to further study its correlation with the splitting of the 0.7 anomaly. At this time, our analysis of experimental data is very phenomenological, presenting parameters and correlations for which it is not possible to make quantitative comparison with theory, since no analytical models are available. However, the trends allow for conclusions about the qualitative behavior.

The second part of this thesis reports experimental and numerical work on electron spin relaxation in large open Quantum Dots (QDs). We studied spin accumulation and relaxation of an electron spin ensemble that is confined to a micronscale QD. Our system is thus best described as an electron ensemble that is ballistically scattering inside a chaotic cavity. Such systems allow for studying spin relaxation in a regime in between bulk samples and ultra small dots, and in this regime spin-orbit effects have a dominant role. Therefore the scattering rate at the edge of the dot has an important influence on the relaxation time.

We have developed a non-local measurement geometry, using QPCs to operate a four-terminal quantum dot system. We demonstrated that this can be exploited to determine for a single device the spin relaxation rate inside the dot ($\tau_{sf} \approx 300\ ps$), contributions to spin relaxation from coupling the dot to reservoirs, and the degree of polarization for spin-selective transport in the contacts ($P \approx 0.8$). We can reproduce the spin relaxation in large quantum dots qualitatively with Monte-Carlo simulations. The values of polarization that we find, are consistent with the short length of our QPCs.

In the Monte-Carlo simulations we used an approach where the relaxation

was simulated with semiclassical electron trajectories in 2D and confined systems using realistic device parameters. This approach allows for fully including three SO effects that occur in realistic 2DEG materials. We calculate values for spin relaxation in micronscale dots with frequent scattering on the edge of the dot, and these values are much lower than calculated values for large high-mobility 2DEG areas, contrary to the established result that strong confinement or frequent momentum scattering reduces relaxation. In this regime of confinement enhanced relaxation, the relaxation time can decrease by more than two orders of magnitude by applying a strong external magnetic field parallel to the initial spin direction. An analogue to confinement enhanced relaxation was also found for large 2D systems with extremely high mobilities.

We also investigated quantum fluctuations in the non-local resistance of the four-terminal quantum dot. In practice, transport in large open QDs always shows mesoscopic fluctuations of the conductance, a characteristic that results from the interference of multiple transport paths through the sample. The amplitude of these fluctuations is strongly reduced when the coupling between the voltage probes and the dot is enhanced. Along with experimental results, we present a theoretical analysis based on the Landauer-Büttiker formalism. Agreement with theory is very good if it is scaled with a factor that accounts for the influence of orbital dephasing inside the dot.

Finally, we report on the annealing mechanism of ohmic contacts to a two-dimensional electron gas (2DEG) in GaAs/AlGaAs heterostructures. These contacts are often realized by annealing of AuGe/Ni/Au that is deposited on its surface. We have obtained optimal annealing parameters for three different heterostructures where the 2DEG lies at a different depth with respect to the surface of the wafer. TEM images of several annealed contacts provided further insight into the annealing mechanism and the formation of a good ohmic contact. Combining this information we have developed a model that can predict the optimal annealing parameters for contacting a 2DEG at a certain depth in a GaAs/AlGaAs heterostructure. This model should have predictive value for many heterostructures, as long the temperature of the samples as a function of time during the annealing process is known.

Samenvatting

Dit proefschrift presenteert onderzoek dat bijdraagt aan het begrijpen van fundamentele eigenschappen van elektronen en elektronenspin in quantum puntcontacten en quantum dots. Deze nanodevices worden gemaakt met ultra-schone niet-magnetische halfgeleiders, met behulp van geavanceerde nanofabricage technieken. Bovendien worden de experimenten gedaan bij extreem lage temperaturen. Daardoor kunnen we bestuderen hoe fundamentele interacties in materialen de elektron- en spintoestanden beïnvloeden. Alhoewel het voornamelijk fundamenteel onderzoek betreft, wordt dit werk ook gemotiveerd door openstaande vragen in het vakgebied spintronica met betrekking tot het gecontroleerd genereren, transporteren en detecteren van elektronenspin. Wij presenteren onderzoek naar twee types devices, het quantum puntcontact (QPC) en de quantum dot (QD). Beide worden gedefinieerd in een tweedimensionaal elektronengas (2DEG) in een GaAs/AlGaAs heterostructuur, door negatieve spanningen aan te brengen op metalen elektroden bovenop de heterostructuur.

Het eerste gedeelte van dit proefschrift presenteert experimenten aan quantum puntcontacten (QPC's). Een QPC kan beschouwd worden als kort eendimensionaal kanaaltje waarin het elektron transport ballistisch is. Als gevolg van de opsluitingspotentiaal in de richting loodrecht op de richting van het transport, is de geleiding van een QPC in nul magneetveld gekwantiseerd in discrete stappen van $2e^2/h$, waarbij e de lading van het elektron en h de constante van Planck is. Bovendien kan de elektron emissie vanuit een QPC spin gepolariseerd zijn wanneer een sterk magneetveld wordt aangelegd in het vlak van het 2DEG. Behalve deze gekwantiseerde geleiding, die volledig wordt begrepen, zijn er nog enkele andere distinctieve kenmerken in de geleiding van een QPC als gevolg van *many-body* effecten, die nog steeds niet volledig verklaard kunnen worden. In het bijzonder is de 0.7 anomalie, een knik in de geleiding rond $0.7(2e^2/h)$ in nul magneetveld, al meer dan 10 jaar een onderwerp van discussie. Andere *many-body* effecten in QPC's zijn de versterking van de elektron g-factor en de nul-bias anomalie, een karakteristiek in de geleiding van een QPC dat sterke overeenkomsten vertoont

met het transport door een Kondo onzuiverheid.

Aangezien een QPC één van de meest fundamentele elektronische systemen is, is het een ideaal modelsysteem om de gevolgen te bestuderen van *many-body* effecten op het transport van spin gepolariseerde elektronen en op spin coherentie in nanodevices. We hebben elektrische transportmetingen gedaan om te bestuderen hoe deze effecten afhangen van de geometrie van de puntcontacten. We hebben de energiesplitsing tussen de eendimensionale subbanden bestudeerd, zowel in nul magneetveld als in een sterk magneetveld, voor een serie van 12 QPC's met identieke materiaaleigenschappen. Daarbij hebben we een duidelijke afhankelijkheid gevonden tussen de grootte van de subband splitsing en de versterking van de effectieve elektron g-factor. Deze parameters hangen op een reguliere manier af van de geometrie van de QPC's en deze afhankelijkheid kunnen we snappen als we een elektrostatisch model van de potentiaal van het puntcontact beschouwen. De kenmerken van de 0.7 anomalie laten geen reguliere afhankelijkheid van de QPC geometrie zien. Echter vinden we wel dat er in sterke magneetvelden een magneetveld-onafhankelijke *exchange* bijdrage is aan de spin-splitsing van de laagste eendimensionale subband, naast de reguliere Zeeman splitsing. Deze *exchange* bijdrage is duidelijk gecorreleerd met de ogenschijn-lijke subband splitsing van de 0.7 anomalie in nul magneetveld. Dat suggereert dat de splitsing van de 0.7 anomalie wordt bepaald door deze *exchange* bijdrage. Ook voor de nul-bias anomalie vinden we geen duidelijke afhankelijkheid van de QPC geometrie, maar onze data laat zien dat het waardevol kan zijn om de correlatie met de splitsing van de 0.7 anomalie verder te onderzoeken. Op dit moment is onze analyse van de experimentele data erg fenomenologisch, waarbij we parameters en correlaties presenteren waarvoor het niet mogelijk is om een kwantitatieve vergelijking met de theorie te maken, aangezien er geen analytische modellen beschikbaar zijn. Desondanks kunnen we op basis van trends in de data conclusies trekken over het kwalitatieve gedrag.

Het tweede gedeelte van dit proefschrift presenteert experimenteel en numeriek werk over elektron spin accumulatie in zogenaamde grote open quantum dots (QD's). We hebben spin accumulatie en relaxatie bestudeerd van een elektronenverzameling die was opgesloten in een micronschaal QD. Ons systeem kan het beste worden omschreven als een elektronenverzameling die ballistisch rondbotst in een kleine chaotische ruimte. Met behulp van dergelijke systemen kunnen we spin relaxatie bestuderen in een regime tussen 2D samples en extreem kleine QD's en in dit regime wordt de spin relaxatie gedomineerd door de spin-baan-koppeling. Daarom heeft de botsingsfrequentie met de rand van de dot een

belangrijke invloed op de relaxatietijd.

We hebben een niet-lokale meettechniek ontwikkeld, waarbij we QPC's gebruiken om een 4-punts meting aan een quantum dot te doen. We laten zien dat dit gebruikt kan worden om voor een enkel device de spin relaxatietijd binnen in de dot te bepalen ($\tau_{sf} \approx 300\ ps$), maar tegelijkertijd ook de bijdrage aan de spin relaxatie door koppeling van de dot aan grote elektron reservoirs en de mate van polarisatie van het spin-selectieve transport in de contacten ($P \approx 0.8$). We kunnen de spin relaxatie in grote quantum dots kwalitatief reproduceren met behulp van Monte-Carlo simulaties. De waarden voor polarisatie die we vinden zijn consistent met de korte lengte van onze QPC's.

In deze Monte-Carlo simulaties hebben we voor een aanpak gekozen waarbij de relaxatie wordt gesimuleerd met behulp van semi-klassieke elektronenbanen in 2D en opgesloten systemen waarbij we gebruik maken van realistische device parameters. Door deze aanpak kunnen we alle drie de spin-baan effecten meenemen die in realistische 2DEG materialen voorkomen. We berekenen waarden voor spin relaxatie in micronschaal dots met frequente botsingen met de rand van de dot, en deze waarden zijn veel lager dan de berekende waarden voor grote 2DEG gebieden met een hoge mobiliteit. Dit is tegenstrijdig met het gebruikelijke resultaat dat sterkere opsluiting of meer frequente botsingen de relaxatie verzwakken. In dit regime van *confinement enhanced relaxation*, kan de relaxatietijd tot wel 2 ordes van grootte afnemen wanneer een sterk extern magneetveld wordt aangelegd parallel met de initiele spin richting. Een analoog van *confinement enhanced relaxation* hebben we ook gevonden voor grote 2D systemen met extreem hoge mobiliteiten.

Met behulp van de 4-punts meting hebben we ook quantum fluctuaties in de niet-lokale weerstand van de quantum dot bestudeerd. In de praktijk zijn er altijd mesoscopische fluctuaties van de geleiding wanneer elektron transport in grote open QD's wordt gemeten. Deze fluctuaties zijn het gevolg van interferentie van verschillende transportpaden door de dot. De amplitude van deze fluctuaties neemt sterk af wanneer de koppeling tussen de spanningsprobes en de dot versterkt wordt. Naast de experimentele resultaten presenteren we ook een theoretische analyse gebaseerd op het Landauer-Büttiker formalisme. De overeenkomst met de theorie is erg goed wanneer het geschaald wordt met een factor die rekening houdt met de invloed van orbitale dephasing in de dot.

Tenslotte rapporteren we over het annealing mechanisme van ohmse contacten aan een tweedimensionaal elektronengas (2DEG) in GaAs/AlGaAs heterostructuren. Deze contacten worden vaak gerealiseerd door AuGe/Ni/Au, dat op het

oppervlak is opgedampt, te annealen. We hebben de optimale anneal parameters gevonden voor drie verschillende heterostructuren waarbij het 2DEG op een andere diepte ligt onder het oppervlak van de wafer. TEM plaatjes van verschillende geannealde contacten geven verder inzicht in het anneal mechanisme en het ontstaan van een goed ohms contact. Met al deze informatie hebben we een model ontwikkeld waarmee we de optimale anneal parameters kunnen voorspellen om een 2DEG op een willekeurige diepte in een GaAs/AlGaAs heterostructuur te contacteren. Dit model zal een voorspellende waarde hebben voor veel heterostructuren, zolang de temperatuur van de samples bekend is gedurende het anneal proces.

Epilogue

The work presented in this thesis was carried out in the Physics of Nanodevices group at the University of Groningen, between April 2004 and June 2008. Only about half a year before the start of this project, during my master's research and research internship, I realized that I really enjoyed doing experimental work, and decided I wanted to do a PhD. Looking back now, I have never regretted that choice, although things did not go quite as planned (as if they ever). From my interviews before the start of the project, it seemed that it was simply a matter of measuring spin accumulation and then the real work would start. How wrong were we... Clearly we had underestimated the amount of issues (mainly technical) that had to be solved, I seriously think the lock-in amplifier is the only item of the entire set-up that made it to the end unchanged. Nevertheless, it is really an undescribable feeling to finally succeed in what you have been working for, and when you are, at that moment, running your long-anticipated experiment and it works!

The results I presented in this thesis are the result of work that I did together with students, technicians and other colleagues. Therefore I want to use this opportunity to thank a number of people, some for directly contributing to this work, others simply for creating a pleasant environment to live and work.

First and foremost, I want to thank Caspar van der Wal for being the best supervisor I could have wished for. I really enjoyed working together and owe you lots of thanks for everything that you have taught me and for all your hard work that made you much more than just a supervisor. Your critical view and perseverance made all of my work and, in fact, my whole working style so much better, that I am sure I will profit from that my entire career. That you have not always made my life easier, could not have been illustrated better than in the cartoon entitled "Erik and Caspar in Dilbertland" in our coffee room, about the seemingly infinite loops of making changes to conference abstracts, papers, and (of course) this thesis.

Also, I want to thank Bart van Wees, not only for giving me the opportunity

to do this project, but also because it was your course on mesoscopic physics that inspired me to do a PhD your group. I am impressed by your physical insight and intuition, and your ability as a "devil's advocate" to always ask the questions I was hoping to avoid, or find weak points in any line of reasoning.

Further, I would like to thank Josh Folk, Yigal Meir and Dominik Zumbühl, I feel honored to have you in my reading committee since many of your papers have been an inspiration for me during my PhD. Here I also want to thank my two paranymphs Herman Nicolai and Pedro Rizo Diago for taking this responsible task so seriously (right?).

During my time as a PhD student I worked closely together with Alex Lerescu, Ji Liu and Javaid Iqbal (aka Goraya). Alex, thank you for teaching me the basics of device fabrication and doing measurements at a few milliKelvin, I really wish that you could have joined in the success that came with the new fridge. Ji, I wish you good luck in writing your thesis. Goraya, you are now the man in charge, I hope you will become a successful experimentalist!

I also owe a lot of thanks to the students that I worked with, Mikel Boute, Friederich Limbach, Joost Flipse and Sander Kamerbeek, your work ended up in this thesis one way or another. Thanks for all the help, I enjoyed being your supervisor.

Further, I want to thank the technical support in our group, Siemon Bakker, Johan Holstein, and Bernard Wolfs. Besides your technical knowledge, you guys bring lots of life to the group and you are of great importance for the good atmosphere. Here I especially want to thank Bernard for all the work he did in helping me build my set-up. I also want to thank Bart Kooi for his help with the TEM images of our ohmic contacts. Further I want to mention here Ubel Linstra for the steady supply of Helium during my experiments, Wigger Jonker for support on the home-built electronics, and Renate Hekkema-Nieborg and Sonja Heimink-Groot for taking care of the administrative work.

Further, I want to thank the members and former members of the Physics of Nanodevices group, I really enjoyed my time in the group, during coffee brakes, borrels, groepsuitjes and other events like the legendary visit to the 2006 World Cup in Germany with Alex, Pedro and Marius C.

Furthermore, I want to thank my friends and family, especially my parents, for their genuine interest in the progress of my project and the necessary distraction. Last, but certainly not least, I want to thank Ellen. Thank you for your endless support, for the joy we have already had together and the great future that lies ahead of us!

Curriculum vitae

Erik Johan Koop

27 May 1980	Born in Stadskanaal, the Netherlands.
1992-1998	Gymnasium at the S.G. Ubbo Emmius in Stadskanaal.
1998-2004	M.Sc. in Applied Physics at the University of Groningen. Graduate research in the group of prof. dr. ir. P. W. M. Blom. Subject: Electroluminescence in organic semiconductor devices.
2003	Student research internship at the Centro de Microanálisis de Materiales in Madrid, Spain with prof. dr. D. O. Boerma. Subject: Low-energy ion scattering on magnetic iron nitride patterns.
2004-2008	Ph.D. research at the University of Groningen in the group of prof. dr. ir. B. J. van Wees, under supervision of dr. ir. C. H. van der Wal. Subject: Electron spin transport in quantum dots and point contacts.

List of publications

1. *Two-impurity Kondo effect in a quantum point contact*
   E. J. Koop *et al.*
   In preparation.

2. *Spin-dephasing anisotropy and persistent spin orientation in a diffusive quasi-1D GaAs wire*
   J. Liu, T. Last, E. J. Koop, B. J. van Wees, and C. H. van der Wal,
   In preparation.

3. *The annealing mechanism of AuGe/Ni/Au ohmic contacts to a two-dimensional electron gas in GaAs/AlGaAs heterostructures*
   E. J. Koop, M. J. Iqbal, F. Limbach, M. Boute, B. J. van Wees, D. Reuter, A. D. Wieck, B. J. Kooi, and C. H. van der Wal,
   Submitted to J. Appl. Phys. (see also arXiv:0808.0928).

4. *Confinement-enhanced spin relaxation of electron ensembles in large quantum dots*
   E. J. Koop, B. J. van Wees, and C. H. van der Wal,
   Submitted to Phys. Rev. B (see also arXiv:0804.2968).

5. *Spin accumulation and spin relaxation in a large open quantum dot*
   E. J. Koop, B. J. van Wees, D. Reuter, A. D. Wieck,
   and C. H. van der Wal,
   Phys. Rev. Lett. **101**, 056602 (2008).

6. *The influence of device geometry on many-body effects in quantum point contacts: signatures of the 0.7 anomaly, exchange and Kondo*
   E. J. Koop, A. I. Lerescu, J. Liu, B. J. van Wees, D. Reuter, A. D. Wieck, and C. H. van der Wal,
   J. Supercond. Novel Magn. **20**, 433 (2007).

7. *Persistence of the 0.7 anomaly of quantum point contacts in high magnetic fields*
   E. J. Koop, A. I. Lerescu, J. Liu, B. J. van Wees, D. Reuter, A. D. Wieck, and C. H. van der Wal,
   In preparation (see also arXiv:0706.0792).

8. *Non-local detection of resistance fluctuations of an open quantum dot*
   A. I. Lerescu, E. J. Koop, C. H. van der Wal, B. J. van Wees, and J. H. Bardarson
   Submitted to Phys. Rev. B (see also arXiv:0705.3179).

9. *Hole transport in poly(phenylene vinylene)/methanofullerene bulk-heterojunction solar cells*
   C. Melzer, E. J. Koop, V. D. Mihailetchi, and P. W. M. Blom,
   Adv. Funct. Mater. **14**, 865 (2004).